SISSA **ISAS**

SCUOLA INTERNAZIONALE SUPERIORE DI STUDI AVANZATI
INTERNATIONAL SCHOOL FOR ADVANCED STUDIES

The role of turbulence in interstellar and intergalactic environments.

Thesis submitted for the degree of
Doctor Philosophiae

PhD Thesis of:
Carmelo Evoli

Supervisor:
Prof. Andrea Ferrara

October 2010

Contents

To j, p and b.
To make the essential visible.

Publications

The work contained within this thesis is largely already presented in the following published papers:

1. **C. Evoli** & A. Ferrara *The turbulent Intergalactic Medium*, 2010, accepted for publication in MNRAS;
2. **C. Evoli**, S. Salvadori & A. Ferrara *The puzzling origin of the ^{6}Li plateau*, 2008, MNRAS, **390**, L14.
3. **C. Evoli**, D. Gaggero, D. Grasso & L. Maccione *Cosmic ray nuclei, antiprotons and gamma rays in the galaxy: a new diffusion model*, 2008, JCAP, **10**, 18.

Some other interesting results that I achieved during my PhD work, only marginally touched in this thesis, are presented in the following published or submitted papers:

4. G. Di Bernardo et al. *Implications of the cosmic ray electron spectrum and anisotropy measured with Fermi-LAT*, 2010, accepted for publication in Astroparticle Physics.
5. **C. Evoli**, P. Salucci, A. Lapi & L. Danese, *The HI content of Local Late-type Galaxies*, 2010, submitted to MNRAS.
6. G. Di Bernardo, **C. Evoli**, D. Gaggero, D. Grasso & L. Maccione, *Unified interpretation of cosmic-ray nuclei and antiproton recent measurements*, 2010, accepted for publication in Astroparticle Physics.
7. M. Valdés, **C. Evoli** & A. Ferrara, *Particle energy cascade in the intergalactic medium*, 2010, MNRAS, **404**, 1569.
8. M. Cook, **C. Evoli**, E. Barausse, G.L. Granato & A. Lapi, *Two phase galaxy formation: the gas content of normal galaxies*, 2010, MNRAS, **402**, 941.

9. M. Cook, E. Barausse, **C. Evoli**, G.L. Granato & A. Lapi, *Two phase galaxy formation: the evolutionary properties of galaxies*, 2010, MNRAS, **402**, 2113.

10. **C. Evoli**, D. Grasso & L. Maccione, *Diffuse neutrino and gamma-ray emissions of the galaxy above the TeV*, 2007, JCAP, **06**, 3.

Introduction

When I meet God, I am going to ask him two questions:
Why relativity? And why turbulence?
I really believe he will have an answer for the first.
Werner Heisenberg, (1901-1976)

This thesis aim at studying the role of turbulence in different astrophysical environments. In fact, turbulence has been observed in a large variety of astrophysical sites, making turbulence one of the most important physical processes under investigation in astrophysics thanks to the contribution of either huge computer simulations and tough analytical treatments. Nevertheless a complete theoretical understanding of its origin and features represents a major challenge both for laboratory engineers and astrophysicists (although the regimes widely differ in the two area in terms of densities, velocities and Reynolds numbers). Since turbulent flows are characterized by chaotic, stochastic property changes resulting in the excitation of an extreme range of correlated spatial and temporal scales, sometimes it is necessary to devise alternative approaches with respect to brute force simulations based on statistical methods.

Observationally, direct evidences of turbulent behavior has been reported in the interplanetary and the interstellar medium by observing the flickering of radio sources. Super-thermal line broadening has been observed in stellar atmospheres and in the interstellar molecular clouds where turbulence is thought to play an important, perhaps dominant, role in star formation. In other cases, it is not possible to probe directly turbulent motions and progress is made by comparing simulations implementing at best the physics of turbulence to with available experimental data. This is the case, for example, of convective energy transport and mixing in stellar interiors or, on extragalactic scales, the turbulence generated by the formation of the largest self-gravitating objects known, clusters of galaxies.

In particular, turbulence appears central to our understanding of the interstellar medium. The distribution of pressures and densities are probably determined as much by turbulent ram pressure as by thermal phase transitions. Furthermore, compression by large-scale turbulent flows may form the molecular clouds where star formation mainly happen, and sustain turbulence within these clouds to support them against gravitational collapse. Being likely dependent on the gas structure, galactic magnetic field exhibits a chaotic structure as well. This can be directly inferred on large scales by Faraday rotation of galactic pulsars and extragalactic radio-galaxies, additionally tested through the diffusive propagation of high-energy charged particles, i.e. cosmic rays (CRs), which travel from sources to the top of the Earth's atmosphere. Cosmic rays are under investigation since $\sim$100 years; yet their origin and properties have not been fully elucidated.

Another place in which we might expect to observe turbulence is the medium between the galaxies, the intergalactic medium (IGM). To probe the prevailing conditions in the IGM most of the interest was focused on the redshifted Lyα resonance line of neutral hydrogen arising in the so-called Lyα forest, and only later the absorption lines associated with ionized heavy elements. However most of the baryonic mass in the Universe is in the form of ionized hydrogen and it suffers for strong shock events either during structure formation and by subsequent mechanical or radiative feedbacks. In this case, very little is known from observations, a part from a couple of indirect observations which will discussed at the end of the first Chapter; theoretical investigations on the subject are also in an infancy stage.

To this aim, the work I have pursued during my PhD was twofold. I have attempted to probe turbulence properties in the interstellar gas of our Galaxy by modeling the cosmic-rays propagation along the galactic magnetic field lines and by comparing the results of the model with multi-messenger, recent observations of secondary CR nuclei and diffuse *gamma* and neutrino emissions. I have actively contributed in the development of a new numerical propagation model for galactic cosmic rays, called DRAGON, which allowed me to investigate the spatial dependence of the diffusion coefficient and its relationship with the spatial distribution of the galactic magnetic field, and finally to produce maps of the diffuse emission at high enough resolution to be compared with the upcoming data of the FERMI observatory. One of the main results of my work it was that all the data available at the present (in particular secondary/primary ratios, anti-proton/proton and positron

fraction) can be consistently matched within a unique diffusion-reacceleration model and, for the first time, I was able to determine the allowed range of the diffusion coefficient spectral index. This spectral index can be correlated to the power-spectrum slope of the galactic magnetic field, hence concluding that Kraichnan type diffusion is significantly favored with respect to the Kolmogorov one (Chapter 3).

On a more cosmological scale, I have studied in detail the interplay between galaxies and the intergalactic medium. I proposed supernova-driven outflows as a mechanism to pump and sustain turbulence in the IGM surrounding high-redshift galaxies. In my model, the evolution of winds are investigated via a semi-analytic approach following both galaxy evolution along its hierarchical growth and the expansion of supernova driven superbubbles as they escape from the halo potential well. Finally, the turbulence evolution within the expanding shells is followed by using a novel approach based on the spectral transfer equation. Such technique allows to follow the turbulent energy density deposited by galactic winds in the IGM, its spectral features, dissipation, and to predict the corresponding thermal/kinetic properties of such component. My findings allowed to predict that the turbulent energy content in these absorbers could be of the same order of the thermal one and a correlation could exist between the turbulent pressure in the expanding shells and the stellar mass of the blowing galaxies. This result is extremely relevant since it demonstrates for the fist time that IGM turbulence could have a non-negligible impact (essentially disregarded until now) on IGM absorption line diagnostics (Chapter 2).

Using the results achieved in these works I was able to investigate another interesting aspect of galaxy evolution: the production of light-elements by CRs. In particular, I focused my work on the lithium-6 problem. The abundance of this element observed in the metal poorest stars of our Galaxy is incompatible with the prediction of the Big-bang nucleosynthesis theory by 3 order of magnitudes and different mechanisms has been invoked to explain its origin. One of the most favorite mechanisms to explain the Li6 production is spallation by CRs accelerated by the first supernovae. I investigated the lithium-6 abundance evolution within a hierarchical model of MW formation which correctly reproduces the [Fe/H] distribution of metal-poor halo stars. Contrary to previous belief, I find that neither the level nor the flatness of the lithium-6 distribution with respect to [Fe/H] can be reproduced under the most favorable conditions by any model in which lithium-6 production is

tied to a (data-constrained) Galactic star formation rate via CR spallation. This result shows in a clear way that the origin of the observed plateau might be due to some other physical mechanism unrelated to star formation occurring in the early Universe (Chapter 4).

Trieste, 15th of August 2010

1

Turbulence in Astrophysics

Turbulence is a ubiquitous phenomenon in astrophysics. Direct or indirect evidence for turbulent motion has been observed in many different astrophysical sites ranging from the smallest bodies and planets up to cosmological scales produced during Big-Bang. Nevertheless the study of turbulence has proved difficult, requiring a firm grasp of applied mathematics and considerable physical insight into the dynamics of fluid: a complete theoretical understanding of the behavior of turbulent fluids is far from being achieved. Only recently have numerical simulations reached sufficiently high resolution to allow realistic investigations of the phenomena observed both in the terrestrial laboratory scale and in the extreme astrophysical environments. However, these simulations are limited to scales in which dissipative effects cannot be fully simulated, and for this reason most of the deepest questions about turbulence are not fully answered yet. Due to this limitation, in order to investigate turbulence and its evolution in most of the models of interest in an astrophysical context it has been necessary to adopt a different approach: instead of brute force simulation it is much more convenient to follow the statistical properties of the model. In this chapter we want to briefly introduce the main aspects of this approach and to give some examples of turbulence in astrophysical studies.

Before going into details, it is worth to define the conditions when a fluid can be considered as turbulent. A fluid of viscosity ν becomes turbulent when the rate of viscous dissipation, which is $\sim \nu/l^2$ at a certain length-scale l, is much smaller than the energy transfer rate $\sim u_l/l$, where u_l is the velocity dispersion at the scale l. The ratio of the two rates is the so-called Reynolds number Re$= u_l l/\nu$. In general,

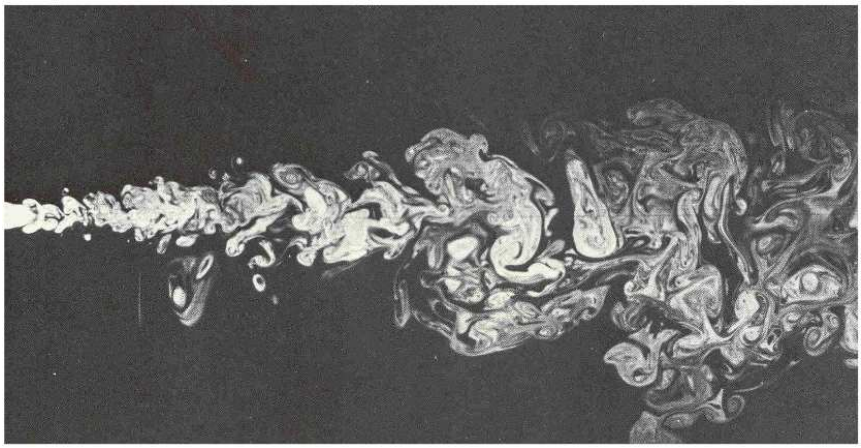

Figure 1.1 A jet initially axialsymmetric with Re = 2300.

when Re is much more larger than unity the system becomes turbulent (see Fig. 1.1). Turbulent structures develop gradually as Re increases, and those with Re $\sim 10^3$ are appreciably less chaotic than those with Re $\sim 10^8$.

The reason for adopting this definition can be further clarified by means of the Navier-Stokes equation which describes the evolution of a viscous fluid:

$$\frac{\partial \vec{v}}{\partial t} + (\vec{v} \cdot \nabla)\, \vec{v} = -\frac{1}{\rho}\nabla p + \nu \nabla^2 \vec{v} + \vec{F}, \tag{1.1}$$

where $\vec{v}$ is velocity, p is pressure, ρ is density and $\vec{F}$ is the force per unit of mass due to the external force acting on the fluid element. The nonlinear term $(\vec{v} \cdot \nabla)\, \vec{v}$ is responsible for sustaining the turbulence and the viscous term $\nu \nabla^2 \vec{v}$ acts as a dissipation term. The Reynolds number can be also defined as the ratio between these two terms if written in their dimensional forms. Viscosity is then important only on small scales, where it dissipates energy passed down from larger scale, while the turbulence injected in the system is dominant instead on large scales or at large velocity.

A different approach with respect to the one we are introducing in this chapter to describe the turbulent behavior of the fluids is adopted in the *chaos theory* which appeared promising of vast applications in the 70s. According to this model, when the non-linear term becomes important the solution of the Navier-Stokes equations become increasingly complex due to a sequence of *bifurcations*, that are sudden changes apparently random in the single element evolution, finally becoming practi-

cally unpredictable and, in other words, chaotic. The evolution of these bifurcations can be treated by means of an elegant *logistic equation* which is the master equation of any non-linear chaotic problem. The logistic equation share with the turbulence two important features: the strong sensitivity on the initial conditions of the system and the contrast between the simplicity of the statistical description of the system and the chaotic trajectories of the single elements.

Astrophysical turbulence has been discussed in many excellent text books [1, 2, 3, 4] and reviews [5, 6] to which we refer the reader for more details.

1.1 Statistical approach in turbulence problems

The transition from a laminar, calm, fluid towards a chaotic, turbulent, situation has an important consequence: the evolution of the fluid elements is not *deterministic* any more. In other words, the initial status of the fluid is always measured with finite precision and so when the turbulence arises, small differences in the initial condition can grow very rapidly, at which point two fluid elements initially close to each other can follow completely different trajectories. For this reason it is difficult to predict the fluid status after a given time: following the evolution of these elements using the deterministic equation of fluid dynamics would require a large number of variables to be considered. For this reason when we treat turbulent flows it is more convenient to adopt a statistical description of the fluid.

We can describe the fluctuating velocity field, at any given instant, as the superposition of periodic variations with all possible wavelengths, where the component of wavelength λ corresponds to the characteristic eddy size. The wavelength range evidently has an upper limit due to the fact that no eddies larger than the dimension of the medium can be present. Rather than the wavelength, it is often more convenient to use the wavenumber, simply defined as:

$$k \equiv \frac{2\pi}{\lambda}. \tag{1.2}$$

The energy per unit volume stored in eddies with wavenumbers between k and $k+\mathrm{d}k$ can be written as $\rho E(k)\mathrm{d}k$, where ρ is the mass density of the gas and $E(k)$ defines the *spectrum* of turbulence. It can be shown that most of the average properties of the turbulent motion can be described as a function of its spectrum. Moreover, the

spectrum is in principle a function of time. However, if turbulence is maintained by an external agent, providing continuous stirring, the turbulent spectrum could reach a stationary state in which all the energy dissipates at the smallest scales at the same rate at which energy is being supplied (see next section).

Some other diagnostic tools have been developed to identify the relevant physical processes. The structure function for an observable A assuming isotropy is defined as:

$$S_p(\delta r) = \langle |A(r) - A(r + \delta r)|^p \rangle, \tag{1.3}$$

for a position r and increment δr. The brackets denote a spatial average over the volume in which the fluid is defined. The structure function can be seen as a measure of correlation. For instance, if the observable A is the velocity, it gives measure of the correlation of the velocities of the fluid elements on scales within the volume. Another useful tool employing two-point statistics is the autocorrelation of A, defined as:

$$C(\delta r) = \langle A(r)A(r + \delta r) \rangle \tag{1.4}$$

Physically this function specifies how much an observable at a different position depends on the same observable at another position.

Finally, the last quantity we need to define here is the power spectrum:

$$P(k) = \langle \hat{A}(k)\hat{A}(k)^* \rangle \tag{1.5}$$

where $\hat{A}(k)$ is the Fourier transform of $A(r)$ and now the brackets denote an average over k-space. The power spectrum is related to the energy spectrum defined above by the relation:

$$E(k) = \int \hat{A}(k)\hat{A}(k)^* \mathrm{d}^3k \tag{1.6}$$

1.1.1 The Kolmogorov theory of turbulence

In a seminal work in 1941, Kolmogorov [7] proposed for the first time to describe the equilibrium state of a turbulent medium using a statistical approach and from this assumption he derived some important consequences for the spectral properties of the fluid. The equilibrium assumption requires that the system under investigation cannot be isolated. In fact, since the turbulence is intrinsically dissipative, any isolated system, i.e. without a source for the turbulent motions, tends naturally to

became less and less chaotic with time, even if the total energy of the fluid elements remains constant. This implies that in order to treat an equilibrium situation we must assume that an external stirring agent is acting on the fluid.

If this external source injects energy into the medium it activates more efficiently eddies of the same scale of the stirring motion. A simple experiment in a realistic fluid shows that these larger eddies soon form eddies of smaller size. The reason why the fragmentation of bigger eddies toward the smaller eddies happens is related to the Kelvin theorem. This theorem states that the vortex lines are frozen into the fluid (i.e. they move with the fluid). The turbulent motions in their randomness tend to push the fluid elements that occupy the same eddy to move far one from each other, and this motion stirs the eddy itself. Since the vorticity must be conserved in an incompressible fluid, this requires a contraction of the radius of the eddy, and therefore a reduction of its size. The mixing of lines of constant vorticity can destroy the eddy and they recombine to form an eddy of smaller size. This process continues on smaller scales via the so-called *energy cascade* (see Fig. 1.2).

Since we are treating an equilibrium process, we can make the assumption that every eddy receive a certain amount of energy per unit time and mass which is completely transmitted to smaller eddies in order to maintain this equilibrium. If the rate of energy input on the large scales is ϵ, the energy dissipated from the smallest scales will also be ϵ. Then the turbulent energy at last dissipates through heating due to viscosity on the smallest scales. If the large forcing scale is much greater than the dissipation scale, then there is an intermediate range where neither the forcing or dissipation are important to the dynamics. This is called the *inertial range*.

Over these ranges the energy rate ϵ can be expressed as a combination of the physical quantities that characterize the eddies. On dimensional grounds, the only possible combination is

$$\epsilon \sim \frac{u_l^3}{l}, \tag{1.7}$$

and therefore

$$u_l \sim (\epsilon l)^{1/3}, \tag{1.8}$$

which means the velocity associated with each eddy is proportional to the cubic root of its size. This result is know as the *Kolmogorov scale-law* and it is valid down to the region of dissipation. The scale where all the energy is dissipated in heating

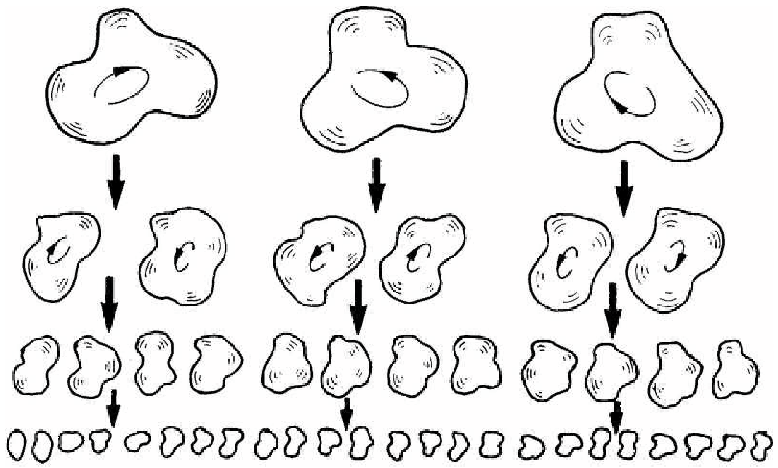

Figure 1.2 A pictorial view of the energy cascade between eddies of different sizes.

trough viscosity corresponds to a Reynolds number of the order of unity, giving

$$l_d u_d \sim \nu, \tag{1.9}$$

and so

$$u_d \sim (\nu\epsilon)^{1/4}. \tag{1.10}$$

Furthermore the spectrum in its inertial range is expected not to depend on the source or on the dissipation physics. Kolmogorov proposed to assume that the turbulence spectrum should appear to be *universal* and with analogous dimensional considerations should be of the form:

$$E(k) \sim \epsilon^{2/3} k^{-5/3}, \tag{1.11}$$

which is the well-known *Kolmogorov power-law*. Therefore, there is no need to keep track of the details of the fluid evolution at the intermediate scales, in the stationary limit: the flow preserves similarity due to the fact that each eddy dissipates its energy to the smaller scales, and the random fluctuations develop a simple power-law form.

A series of experiments have been performed in terrestrial laboratories to verify whether this simplified picture can be applied in real fluids. The results are in good agreement with the theory (see Fig. 1.3). Remarkably, even if this result has been obtained with a back of the envelope derivation, it has been convincingly observed in many astrophysical sites, as for example the interstellar medium (see § 1.2.2).

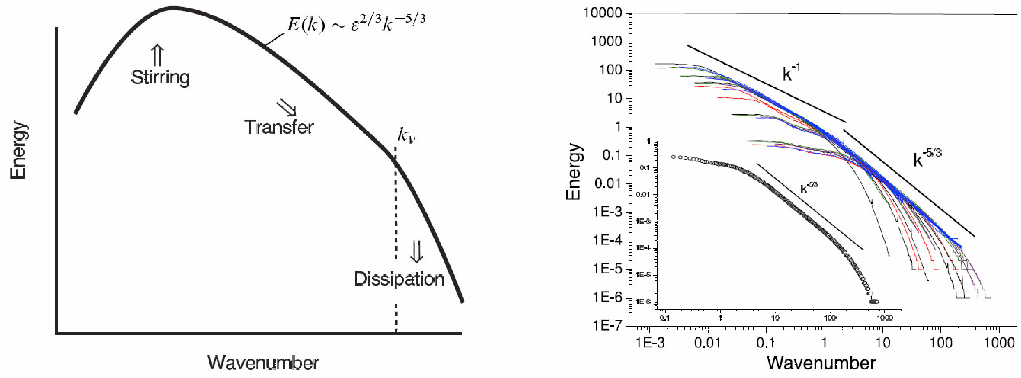

Figure 1.3 Comparison between the theoretical expectations from the Kolomogorov analysis and an experimental result obtained from the Princeton Superpipe facility (`http://gasdyn.princeton.edu`)

It is worth remembering that this result has been obtained under the assumption of an incompressible fluid, a condition which is not valid for most astrophysical fluids. The most important characteristic of a compressible fluid is the generation of acoustic waves, which are pressure and density fluctuations propagating at finite speed. In the context of turbulence theory this means that the shear, which in the incompressible case simply transfers the energy between eddies of different sizes, can now produce density variations which will propagate as sound waves in the medium.

If we define the Mach number as $M_l \equiv v_l/c_s$, it can be shown that the spectrum in the compressible (homogeneous) case is modified by a factor M_l^5 which takes into account that heat transport can happen also by means of sound waves propagation. For high Mach number these sound waves are actually shocks which dissipate energy very efficiently and contribute creating a turbulent pattern of the velocity field.

1.1.2 Dynamical equation

In some cases the assumption of a steady state cannot be strictly applied, and even if we are working in the inertial subrange, we need to treat the time evolution of the turbulence spectrum. The dynamical equation for $E(k,t)$ in isotropic turbulence can be derived in a straightforward way from the dynamical equation for the two-point velocity correlation [5, 8, 9, 2] and the resulting equation is written in the form:

$$\frac{\partial}{\partial t}\int_0^k \mathrm{d}k' E(k,t) = \int_0^k \mathrm{d}k' F(k,t) - 2\nu \int_0^k \mathrm{d}k' k^2 E(k,t) + \int_0^k \mathrm{d}k' S(k,t), \quad (1.12)$$

where $F(k,t)$ is the energy transfer function, ν is the kinematic viscosity and $S(k,t)$ is a source function. The left-hand side describes the change in the kinetic energy and the dissipation occurring in large eddies with wavenumber less than k. The flow of energy from large eddies is split in two contributions: part of it is transmitted in the form of kinetic energy to smaller eddies, and part is directly dissipated into heat trough viscosity.

A complete solution of this dynamical equation in its general form has not yet been found; the main difficulty is merely a restatement of the *closure* problem for the hydrodynamic equations since the transfer term is in principle a function of the third-order spectrum. In fact, instead of being forced to make an assumption about the next higher order velocity correlation function, it is necessary to postulate an explicit form of $F(k,t)$; this is usually done on the basis of some physical/dimensional arguments.

A general expression for $F(k,t)$ which automatically satisfies the condition of *local* interaction in *every* region of the spectrum has been proposed by [10]:

$$\int_0^k \mathrm{d}k' F(k',t) = -\alpha E^{3/2}(k,t) k^{5/2} \tag{1.13}$$

where α is a dimensionless constant of the order of unity whose correct value can be extrapolated from experiments [9].

Given the adopted form of the transfer spectrum, we can rewrite the Eq. 1.12 in its more convenient differential form:

$$\frac{\partial}{\partial t} E(k,t) = -\alpha \frac{\partial}{\partial k} \left[E(k,t)^{3/2} k^{5/2} \right] - 2\nu k^2 E(k,t) + S(k,t)\,. \tag{1.14}$$

Eq. 1.14 completely describes the evolution of the turbulent spectrum, provided the appropriate boundary and initial conditions are specified:

$$E(0,t) = E(\infty,t) = 0\,,\ 0 \leqslant t < \infty, \tag{1.15}$$

and

$$E(k,0) = E_0(k)\, 0 \leqslant k < \infty\,. \tag{1.16}$$

As an example of the application of this approach we refer the reader to [11] in which the reader can find a discussion of the steady state solutions of the Eq. 1.14

in the context of ISM turbulence.

We note here that the dissipation term contains a factor k^2, which means that the smaller scale contributes prevalently to the dissipation. Moreover, it is easy to demonstrate that:

$$\int_0^\infty F(k,t)dk = 0. \tag{1.17}$$

Intuitively, this result tells us that this term does not modify the total energy content, being a simple transfer function. Therefore, if we integrate the Eq. 1.14 over the entire spectrum we find that, at any time:

$$\epsilon = \int_0^\infty 2\nu k^2 E(k,t)\mathrm{d}k, \tag{1.18}$$

which means that these two rates can be easily compared.

1.1.3 The case of a magnetic field

A discussion of the evolution of a turbulent charged fluid in the presence of a magnetic field would deserve a long treatment, since it requires solving the time-dependent MHD equations. Since this is far beyond the goals of this chapter we will simplify the treatment, discussing only what is changed in the Kolmogorov picture in the presence of a magnetic field.

An essential feature of the Kolmogorov treatment is the *locality* of the interaction between the different elements of the cascade. However, if the fluid is embedded in a magnetic field, long range forces could break this assumption. In particular, Alfvén waves generated by the disturbances can transfer energy and momentum at any distance even in an incompressible fluid. By adding a long-range interaction, the correlation-lengths between the fluid elements are modified and a length-scale is added to the cascade spectrum.

Let us assume that the fluid is embedded in a magnetic field, B_0, which is coherent on large scales (comparable to the source scale), L. The Alfvén velocity, that is the velocity with which the field perturbations propagate, is $v_A = B/\sqrt{4\pi\rho}$ and this implies a characteristic time in which they transfer energy of the order of $t_A \sim L/v_A$. We compare this with the hydrodynamic timescale, the eddy turnover time for each scale k^{-1}, that is $1/(kv_k)$. When these two times are comparable, i.e.

$v_A/L = kv_k$ the spectrum becomes:

$$E(k) \sim \frac{v_A}{L} k^{-3/2}, \tag{1.19}$$

which is of the form derived by Kraichnan in 1965 [12]. The same result can also be obtained by considering that in the presence of a magnetic field the dissipation rate increases by a factor $\sim v_k/v_A$. Therefore, the transfer energy rate becomes $\epsilon \sim kv_k^4/v_A$ and hence the spectrum becomes $E(k) \sim \epsilon^{1/2} v_A^{1/2} k^{-3/2}$.

Further refinements of this simplified picture for compressible magnetic turbulence have been examined in recent years, in particular for the purposes of investigating the role of the anisotropy introduced by the large-scale field. In fact, due to the presence of a vector field, the medium is inherently anisotropic. This means that the motion of the fluid elements (as well as charged particles) along or perpendicular to the mean field could be different and the *parallel* and *perpendicular* spectra could have different slopes [13, 14].

1.2 Turbulence in astrophysical environments

The following discussion is concerned with the astrophysical sites where a turbulent behavior has been directly observed or has been inferred by comparing with observations simulations in which turbulence has a crucial role.

1.2.1 The Sun

The gas above the visible surface of the Sun is not in hydrostatic equilibrium. Instead, because of geometrical constraints and because of a gravitational potential inversely proportional to the radial distance, there is the possibility of a critical point, where the radial velocity equals the sound speed. The theory of such flows is explained in a number of text books on compressible flows or on astrophysical fluid dynamics [1]. In the case of the Sun the gas reaches speeds of around 400 km/s in the equatorial plane and 800 km/s at higher latitudes [15]. The solar wind is turbulent and fluctuates between 300 and 800 km/s on time scales ranging from seconds to hundreds of hours [16].

Direct evidence of turbulence in the solar corona is the observation of an approx-

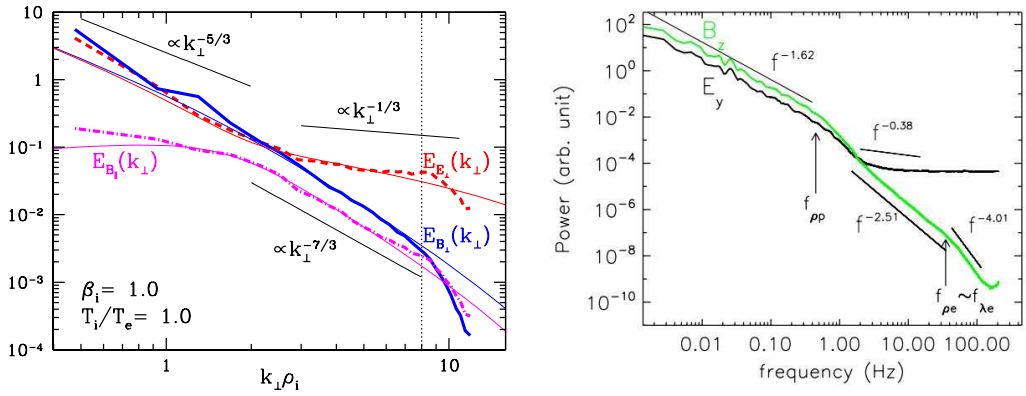

Figure 1.4 Spectra of electric and magnetic fields from a gyrokinetic simulation [18] (left) compared with those obtained from the Cluster spacecraft [19] (right). Note the approximate $k^{-5/3}$ spectrum below the proton gyrofrequency and an approximate $k^{-7/3}$ spectrum for the magnetic field (blue on the left and green on the right) between the proton and electron gyrofrequencies (in the right hand plot referred to as $f_{\rho \mathrm{p}}$ and $f_{\rho \mathrm{e}}$, respectively), followed by a steeper dissipation subrange [21].

imate $k^{-5/3}$ energy spectrum both for velocity and magnetic field [17], which above the typical electron gyrofrequency becomes a $k^{-7/3}$ spectrum for the magnetic field and a $k^{-1/3}$ spectrum for the electric field [18, 19] (see also Fig. 1.4). Moreover, the decay of turbulence with distance as an evidence for additional heating has been confirmed by a number of authors[16, 17, 20].

The photosphere is the visible surface of the Sun, from where photons can reach the Earth in a direct path. Deeper inside the Sun the gas is opaque and photons are continuously absorbed and re-emitted, following approximately a diffusion-like process. At the surface, the Sun exhibits a granular pattern that can already be seen with small amateur telescopes. The pattern is irregular and changes on a time scale of around 5 minutes. The visible granulation is just a thin layer on top of a deep convection zone. The convection zone covers the outer 30% of the Sun by radius. The inner 70% are convectively stable. This region is referred to as the radiative interior. Its overall dynamics can be understood through simulations and turbulence theory (i.e. mixing length theory) [22]. By calculating diagnostic spectra in the visible light and comparing with observations one can determine the

abundance of chemical elements [23, 24, 25]. The chemical element abundances are important for determining the opacity of the gas which, in turn, determines the radial structure of the Sun.

From the viewpoint of turbulence theory, this type of convection is special not so much because the Rayleigh number is extremely large ($\sim 10^{30}$), but mainly because the density and temperature stratification is extreme, covering six orders of magnitude of change in density and a factor of $\sim 3 \times 10^2$ in temperature. This huge dynamic range implies that the turbulence characteristics become strongly depth-dependent. The energy-carrying scale varies with depth in such a way that it is proportional to the local pressure scale height, H_p. The pressure scale height is proportional to the temperature and varies from about 200 km at the top of the convection zone to about 6×10^4 km at the bottom.

The typical correlation time of the turbulence is expected to be proportional to the local turnover time, $H_p/u_{\rm rms}$, where $u_{\rm rms}$ is the rms velocity associated with the turbulence. Estimating the convective energy flux as $F_{\rm conv} \sim \rho u_{\rm rms}^3$, we expect $u_{\rm rms}$ to vary by a factor of 100 from about 4 km/s at the top of the convection zone to about 40 m/s at the bottom. Thus, the turnover times vary by more than four orders of magnitude, from minutes at the top of the convection zone to about a month at the bottom.

1.2.2 The interstellar medium

The gas between the stars can be observed in absorption or emission both at infrared and radio wavelengths. The line of sight velocity component can be determined by Doppler shifts of spectral lines; see, e.g., [26]. There is a general power law scaling of velocity amplitudes and velocity differences with geometrical scale [26, 27, 28]. Velocity dispersions scale with size to a power of about 0.4 from sub-parsec scales to scales of the order of about 1 kpc; see Fig. 1 of [27]. The velocity scaling is practically the same in regions with varying intensity of star formation, indicating that the velocity scaling is inertial, and driven mostly by energy input at large scales, rather than a result of direct, local driving by ongoing star formation [29, 30, 31].

Direct evidence of turbulence on small length scales ($\sim 10^{12}$ cm) in the ISM comes from radio scintillation measurements [32, 33].

Galaxies such as our own Galaxy have typical radii of $R \sim 15$ kpc. The density

decreases rapidly away from the midplane with a typical density scale height of $H \sim 70\,\mathrm{pc}$. Near the midplane of a typical galaxy the turbulent velocities are around 15 km/s. This implies a typical turnover time, H/u_{turb}, of around 5 Myr.

An important aspect is the occurrence of supernovae, which mark the death of massive stars and provide a significant energy release into the interstellar medium through thermal energy and momentum injection. Traces of supernovae are seen as supernova remnants, which give a qualitative idea about the nature of interstellar turbulence.

Supernova explosions contribute about $E_{\mathrm{SN}} = 10^{51}$ erg per explosion. With about 20 supernovae per million years per kpc^2 estimated for the solar neighborhood this corresponds to an energy injection per unit area of

$$\int \epsilon_{\mathrm{SN}}\,\mathrm{d}z \sim 20 \times 10^{51}\,\mathrm{erg}/(3 \times 10^{13}\,\mathrm{s} \times 9 \times 10^{42}\,\mathrm{cm}^2) \sim 7 \times 10^{-6}\,\mathrm{erg\,cm^{-2}\,s^{-1}}. \tag{1.20}$$

This is almost two orders of magnitude more that what is required to sustain the turbulent energy dissipation per unit area and time, which may be estimated to be

$$\int \epsilon\,\mathrm{d}z \approx 0.5\,\rho u_{\mathrm{1D}}^3 \sim 10^{-24}\,\mathrm{g\,cm^{-3}}\,(10^6\,\mathrm{cm\,s^{-1}})^3 \sim 10^{-6}\,\mathrm{erg\,cm^{-2}\,s^{-1}}, \tag{1.21}$$

where the mean density of the interstellar medium is $\rho \sim 2 \times 10^{-24}\,\mathrm{g\,cm^{-3}}$ and the one-dimensional rms velocity is $u_{\mathrm{1D}} \approx 10\,\mathrm{km/s} = 10^6\,\mathrm{cm\,s^{-1}}$. This is also in good agreement with simulations [34].

The linear polarization properties of synchrotron radiation can be used to infer the magnetic field both along the line of sight via Faraday rotation and perpendicular to it through the polarization plane projected onto the sky [35, 36, 37]. The field strength is typically around $5\,\mu\mathrm{G}$ in the solar neighborhood of our Galaxy, but it can be several mG in the galactic center [38, 39]. For many spiral galaxies large-scale magnetic fields have been found. In many of them the magnetic field is approximately axisymmetric and symmetric about the midplane [40].

1.2.3 Molecular clouds

Understanding star formation is of central importance to understand the formation and evolution of galaxies. The traditional solution of the problem of star formation is gravitational fragmentation, that is cores of molecular clouds greater than a certain

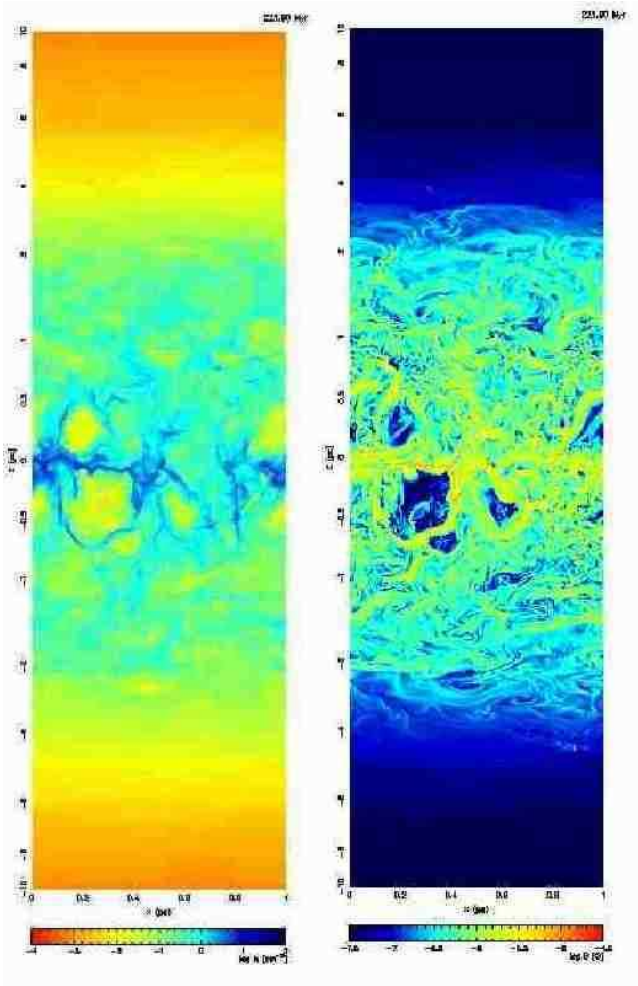

Figure 1.5 Two-dimensional slices through a three-dimensional simulation domain of supernova-driven turbulence in the interstellar medium showing the vertical distribution of the density (left) and magnetic field (right). Note the appearance of supernova remnants in density and magnetic fields as well as an overall concentration around the midplane at $z = 0$. Courtesy of [34].

critical density become gravitationally unstable, fragment and begin to collapse. By studying the growth of plane wave density perturbations in an infinite uniform medium with a finite pressure (and assuming that gravity plays a dominant role with respect to magnetic fields, turbulence, rotation and so on) it is possible to show that the perturbations whose wavelength exceed a critical value are gravity dominated and grow exponentially. The critical length of perturbations that are actually collapsing is called the *Jeans's length* and can be expressed as a function of

the medium density, ρ and the sound speed in the medium, c_s, in this way:

$$\lambda_J = c_s \sqrt{\frac{\pi}{G\rho}}\,. \tag{1.22}$$

The disk of the MW contains $\sim 10^9$ $M_\odot$ of molecular gas in the region where star formation is known to occur. From the gravitational fragmentation model, one can obtain a free fall time of the gas, in the absence of other sources of pressure support:

$$t_{\rm ff} = \frac{1}{\sqrt{G\rho}}\,, \tag{1.23}$$

which is about 3×10^6 years for the MW. This would give a star formation rate of around 250 $M_\odot$ yr^{-1} which is much greater than the observed rate of about 3 $M_\odot$ yr^{-1}. Clearly, this result implies the fragmentation model is incomplete, the complexity of the fragmentation process due to the effects of turbulence and magnetic fields should be taken properly into account.

Today it is agreed that supersonic turbulence occurs within molecular clouds [41]. This is inferred from different observations of molecular line broadening which indicate, firstly, a velocity dispersion comparable to or greater than the speed of sound and, secondly, a power-law dependence of the velocity dispersion, $\Delta\nu \propto l^\alpha$, in the range of length scale $0.1\,{\rm pc} \lesssim l \lesssim 10\,{\rm pc}$ of the associated structures [28, 42, 29]. This has been interpreted as a manifestation of the universality of interstellar turbulence (Heyer & Brunt 2004) which has important consequences for the theory of turbulence-regulated star formation: *Larson-type* relations for the velocity dispersion are explained as a direct consequence of the self-similarity of the turbulence cascade, with a possible modification of the scaling exponent due to magnetic fields, self-gravity or thermal processes [43, 44, 45, 46].

1.2.4 Accretion discs

Accretion discs are disc-like structures through which gas gradually spirals toward a central massive object while converting potential energy into kinetic and magnetic energies that are dissipated and radiated away. This conversion is believed to be turbulent in nature and may be driven by the magneto-rotational instability [47, 48]. An alternative mechanism for disk dissipation is that the disk functions as a self-regulating buffer. As long as the disk accretion towards the central object is smaller

than the rate of mass infall onto the disk from the surrounding nebula, the mass density of the disk increases. When the surface density reaches a level sufficient for gravitationally driven instabilities to develop, spiral waves starts to grow, develop into spiral shocks, and dissipation in the shocks then enhances the disk accretion enough to balance the rate of in-fall onto the disk [49, 50].

In order to allow material to spiral inward at a mass accretion rate $\dot{M}$, half of the orbital potential energy is converted viscously and resistively into heat and radiation. Therefore the total (bolometric) luminosity of an accretion disc is [51]

$$L = \frac{GM\dot{M}}{2R_{\rm in}}, \tag{1.24}$$

where M is the mass of the central object and $R_{\rm in}$ is the inner radius of the accretion disc. Obviously, the further the disc stretches toward the central object, i.e. the smaller the value of $R_{\rm in}$, the more efficient the energy conversion will be. Discs around black holes are most efficient in this respect, because here the innermost stable orbit is 1–3 Schwarzschild radii, i.e. (2–6)$\times GM/c^2$, where c is the speed of light. Thus, $L = 0.1 \times \dot{M}c^2$, which constitutes a much more efficient conversion than nuclear fusion, where the efficiency is only $0.007 \times \dot{M}c^2$ [1]. Here we have used for $\dot{M}$ the rate of hydrogen burning [51].

1.2.5 Galaxy clusters

Galaxies themselves tend to cluster on Mpc scales. There are typically around 10^4 galaxies in a cluster, but some clusters can be substantially smaller. All clusters are generally strong X-ray emitters, but some are also strong radio-emitters resulting from synchrotron emission in the presence of magnetic fields.

Typical temperatures are around 10^8 K corresponding to a sound speed of around $1000\,\mathrm{km\,s^{-1}}$. The implied velocity dispersion is is of the same order, as expected when the system is in approximate Virial equilibrium. With typical length scales on the order of the density scale height, $H_\rho = 100\,\mathrm{kpc}$, the turnover time is

$$100\,\mathrm{kpc}/(1000\,\mathrm{km/s}) = 0.1\,\mathrm{Gyr}\,. \tag{1.25}$$

This would also be the typical decay time of the turbulence in the absence of mech-

[1] Note that the factor 0.007 comes from the relative mass difference between a helium atom (4.0026) and four hydrogen atoms (1.0078).

anisms driving the turbulence.

Mechanisms for driving such turbulence include mutual encounters of clusters [52, 53]. Given that only a fraction of all galaxy clusters also have strong radio halos [54], one may speculate that these clusters have undergone a recent encounter or merger with another cluster within the last few Gigayears. Obviously, in this scenario one would just have decaying turbulence between encounters. In the context of galaxy clusters this subject has been studied by various groups [55, 56, 57]. Another mechanism that has been discussed in the literature is the driving by individual galaxies moving through the cluster and producing a turbulent wake behind them [58, 59, 60].

1.3 Cosmic ray propagation in the Galaxy

Many aspects of what we know about the cosmic ray (CR) nuclei, in particular those with energies from $\sim$1 to $\sim 10^5$ GeV/nucleon, can be understood in terms of shock acceleration at supernova blast waves and diffusive propagation in turbulent magnetic fields in the Galaxy. For example, as we will discuss in the next subsection, the simple observation that the composition of the CR observed at the top of the atmosphere is different from that one of the solar system nuclei is a direct hint of the importance of diffusion of these particles in the ISM.

In fact, being charged particles, the galactic CRs cannot stream freely throughout the Galaxy, they instead interact with the galactic magnetic field which exhibit a random pattern, likely due to a strong coupling with the chaotic structure of the interstellar gas. It is for this reason that the resonant interaction of CRs with the interstellar magnetic field irregularities has been successfully proposed to model the diffusive behavior of CR density.

Since all our knowledge of CR propagation comes via secondary CRs observed at the Earth (with an additional information from produced diffuse γ-rays and synchrotron radiation), the correct interpretation of all these observables in a propagation model in which diffusion has a dominant role is equivalent to probe the turbulent properties of the ISM.

1.3.1 Evidence for diffusive propagation

Before going into details about the theoretical modeling of CRs propagation (see also Ch. 3), it is useful to present the most stringent pieces of evidence of the diffusive behavior of galactic CRs.

If we assume that some nuclei, e.g. Boron, are only produced by spallation of CRs on the ISM nuclei (since they are not observed elsewhere in the Galaxy and they are almost absent as end products of stellar nucleosynthesis, see Fig. 1.6), we can determine the average amount of matter traversed by CRs nuclei necessary to produce the observed amount of secondary CRs. According to this calculation CRs must traverse typically a matter density of about $x = 5$ g cm^{-2} between injection and observation [4]. We can convert this into a typical age τ for the CRs residual time if we know the mean matter density through which they have travelled:

$$x = c\langle\rho\rangle\tau. \tag{1.26}$$

If the CRs spend most of their time in the disc, whose density is known and it is $N \sim 1$ cm^{-3}, then we can estimate $\tau \sim 3 \times 10^6$ years. However, it might be that they spend longer in regions of lower particle density, such as the halo, which means that this time could be easily longer. In any case, we soon realize that this timescale is much longer than the time spent by a relativistic particle moving straight along the typical dimension of the propagation region ($1 - 10$ kpc), which is about $3 \times 10^{3-4}$ years. We must conclude that the propagation is not ballistic and the diffusive effects are actually dominant.

Another piece of evidence comes from the isotropy of the arrival directions of CRs. If CRs streamed freely out of the Galaxy, then their distribution on the sky would be highly anisotropic, with most of the flux coming from the direction of the central regions of the Galaxy. The observations show instead a very high degree of isotropy of CRs in the energy range in which galactic CR contribution is dominant. The CRs do not follow straight lines in their propagation but instead they scatters many times losing the angular information.

If we justify these observations by assuming that the CRs are effectively scattered, either by irregularities in the magnetic field or by waves excited by CRs themselves (see the next subsection) then we could describe the dynamics of charged particles in the Galaxy by means of an isotropic diffusion model.

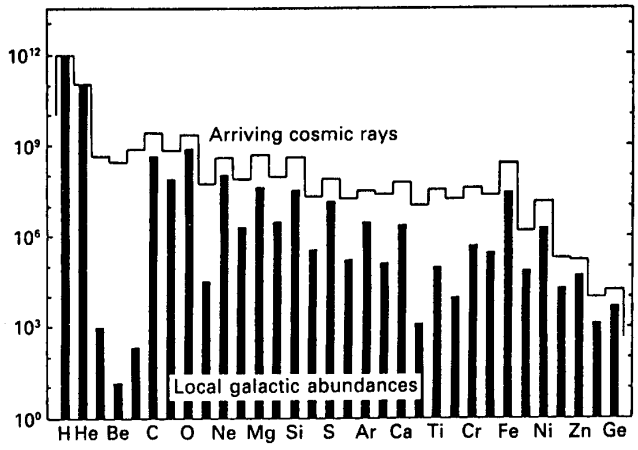

Figure 1.6 Relative abundance of nuclei in the ISM compared with the CR. Courtesy of [61].

The simplest version of the diffusion equation holds:

$$D\nabla^2 N - \frac{N}{\tau} = 0, \tag{1.27}$$

and if the particle must diffuse in about 10^6 years and, in this time, they reach the half-thickness of the disc, about 300 pc, then we can finally obtain an *order-of-magnitude* estimate of the diffusion coefficient from the above equation as

$$D \sim L^2/\tau = 3 \times 10^{28} cm^2 s^{-1}. \tag{1.28}$$

Rewriting this in terms of a mean free path λ, we find $D = 1/3\lambda v$ and hence $\lambda \sim 1$ pc. This value happens to be the typical scale of inhomogeneities in the interstellar medium, associated with supernova shells and regions of ionized hydrogen.

1.3.2 The diffusion coefficient

We have seen that CR diffusion has been suggested for explaining why the energetic charged particles observed at the top of the atmosphere have highly isotropic distributions and why they are well retained in the Galaxy.

On the microscopic level, the diffusion of CRs results from particle scattering on random MHD waves and discontinuities in the ISM. MHD waves arise in magnetized plasma in response to any perturbation. The effective collision integral for charged energetic particles moving in a magnetic field with small random fluctuations $\delta B \ll$

B can be taken from the quasi-linear theory of plasma turbulence [62]. The wave-particle interaction has a resonant character, so that an energetic particle is scattered predominantly by those irregularities of the magnetic field that have their projection of the wave vector on the average magnetic field direction equal to a multiple of $1/r_g\mu$, where $r_g = pc/ZeB$ is the Larmor radius and μ is the pitch angle. The resulting spatial diffusion is strongly anisotropic locally, predominantly following the magnetic field lines.

This result can be used to calculate the maximum energy of the particle that can be retained by the Galactic magnetic field. In fact, if we assume the largest scale on which the interstellar magnetic field fluctuates is $L \sim 100$ pc and that the more energetic particles can be effectively trapped in the Galaxy should be $r_g \sim L$ given that the Larmor radius is

$$r_g \sim 1\, kpc \frac{E[EeV]}{ZeB[G]}, \tag{1.29}$$

and the typical Galactic magnetic field strength is of order of few G, it follows that the Milky Way is able to confine particles up to the 10^{15} eV, which corresponds to that of a slope change in the CR spectrum.

Following several detailed reviews of the theory of CR diffusion [63, 61, 64] the spatial diffusion coefficient at $r_g < L$ can roughly be estimated as $D \sim (\delta B/B)^{-2} v r_g/3$ where δB is the amplitude of the random field at the resonant wave number $k_{res} = 1/r_g$. The spectral energy density of interstellar turbulence has a power-law form $\epsilon(k)\mathrm{d}k \sim k^{-2+\alpha}\mathrm{d}k$, and observations suggest $\alpha \sim 1/3$ over a wide range of wave numbers $1/(10^{20}\,\mathrm{cm}) < k < 1/(10^{8}\,\mathrm{cm})$ (§ 1.2.2) and the strength of the random field at the main scale is $\delta B \sim 5\mu$G. This gives an estimate of the diffusion coefficient $D \sim 2 \times 10^{27} \beta R_{GV}^{1/3} cm^2 s^{-1}$ for all CR particles with magnetic rigidities $R < 10^8$ GV, in reasonable agreement with the empirical diffusion model.

Remarkably, the scaling law $D \sim R^{1/3}$ is determined by the value of the exponent $\alpha = 1/3$, typical of a Kolmogorov spectrum. Theoretically, the Kolmogorov-type spectrum may refer only to some part of the MHD turbulence that includes the structures strongly elongated along the magnetic field direction and that cannot provide the significant scattering and required diffusion of CRs [65]. In parallel, the more isotropic part of the turbulence, with a smaller value of the random field at the main scale and with exponent $\alpha = 1/2$ typical for the Kraichnan-type turbulence spectrum, may exist in the ISM [66].

The Kraichnan spectrum gives a scaling $D \sim R^{1/2}$, which is close to the high-energy asymptotic form of the diffusion coefficient obtained in the plain diffusion version of the propagation model. Thus, the approach based on kinetic theory gives a proper estimate of the diffusion coefficient and predicts a power-law dependence of diffusion on magnetic rigidity.

However, the actual diffusion coefficient must be determined with the help of empirical models of CR propagation in the Galaxy.

1.4 Is it the IGM turbulent?

Unlike the case of the ISM, we do not have any direct observation that can demonstrate whether the gas far from the galaxy is actually in a turbulent phase. In fact, the observational techniques that have been used to probe the turbulence of the interstellar gas, like for example pulsar scintillation, are not easily applied to the IGM observations.

However, in the accepted scenario of structure formation, most of the baryons are in filamentary structures which are themselves permeated by shocks induced by gravitational collapse, and moreover observations of metal pollution in high-redshift absorption gas suggests that strong galactic feedback, probably associated with galactic outflows, has been acting to transport stellar products out of the galaxy environment. These theoretical arguments should be strong enough to convince the reader that the IGM could host some level of turbulence.

In the Ch. 3 we propose a realistic model for injecting turbulence in the IGM by galactic feedback and for following the dissipation time-scales, but it is worth now to discuss about two recent observational results that can be interpreted as the first direct measurement of IGM turbulence and which are among the motivations of this work.

1.4.1 High-redshift CIV absorbers

Gravitational lenses can be used to probe the high-redshift universe due to their capability for magnifying the angular extent of a background object at cosmological distances. In particular, measurements of absorption pattern differences produced by high-redshift intergalactic gas on multiple line of sight to gravitationally-lensed

QSOs has been used by [67] to investigate the nature of hydrodynamic disturbances in the IGM. By using this effect they were able to spatially resolve proper scale down to tens of parsec at redshift $z \sim 3$.

At this redshift most of the absorbers in the QSO line of sight arise in low density condensations of the IGM and may be subject of feedback from nearby galaxies. In fact, observations indicate that already at redshifts $3 - 4$ the high ionization phase is widely polluted with metals ($Z \sim 10^{-2.5} Z_{\odot}$, [68], see also Ch. 2). Since the metals are mainly produced in stars within galaxies this it is widely interpreted as an evidence of the interaction of this gas with a sort of galactic feedback.

The differences between the absorption pattern in two adjacent lines of sight can be characterized in a variety of ways. If one thinks of the gas clouds in terms of coherent objects it makes sense to measure the optical depth or column density differences between the lines of sight, to determine the scale over which the gas densities vary and to get an idea of the cloud sizes. Differences across the lines of sight of the velocities projected along the line of sight (i.e. the velocity shear) provide clues to turbulence and systematic motion (e.g., rotation, expansion) in the gas.

The data allowed to obtain a crude estimate of the turbulent energy in the gas.

While the Kolmogorov approach may not be applicable, the usual dimensional analysis connecting the energy transfer rate ϵ with all the other physical quantities can give us a grasp of the physical condition of the observed region of the IGM.

In particular, the structure function defined as a function of the beam separation s,

$$B(s) = \langle v(s') - v(s'') \rangle^2 \sim v_s^2 \sim (\epsilon s)^{2/3} \tag{1.30}$$

can be measured from the pairs of C IV column density weighted line of sight velocities, as a function of projected beam separation.

As shown in the Fig. 1.7, taking $s = 300pc$ as a reference point, $B(s) = 100$ (km/s)^2, and the energy rate is found to be

$$\epsilon \sim 10^{-3}\, cm^2 s^{-3}\,. \tag{1.31}$$

This is considerably less than values measured, e.g., for the Orion nebula, where $\epsilon \approx 0.1 - 1$ cm^2 s^{-3} [69] but it is comparable to the global rate of energy input into

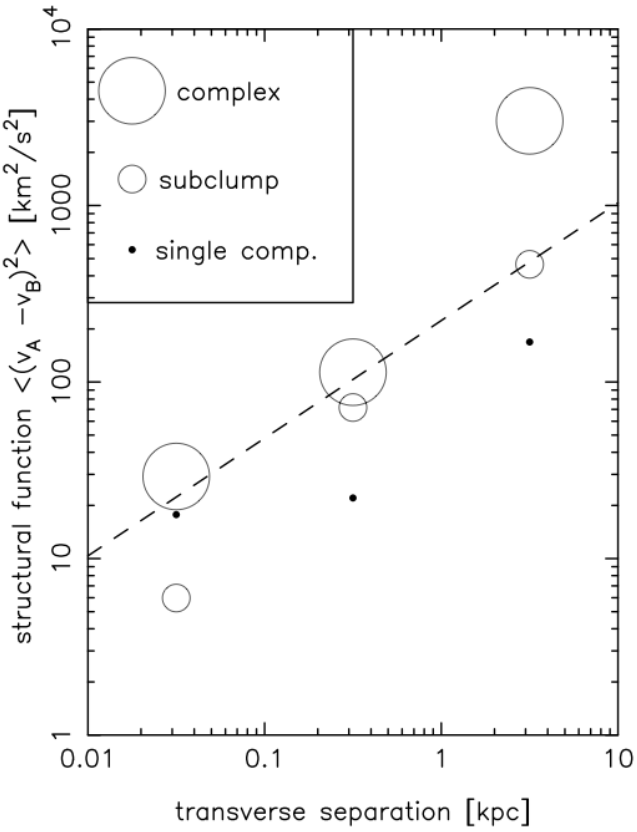

Figure 1.7 Structure function as a function of beam separation. The dashed line illustrates a Kolmogorov spectrum with a vertical normalization corresponding to an energy transfer rate $\epsilon = 10^{-3}$ cm^2 s^{-3}. Courtesy of [67].

the Galactic ISM.

Since the energy transfer rate ϵ can be equated to the dissipation rate (see § 1.1.2) it has been possible to estimate the approximate time scale for dissipation, i.e. the time it takes to transform the mean kinetic energy in the gas, at a rate ϵ into heat:

$$\tau_{\rm diss} \sim \frac{1}{2}\frac{< v^2 >}{\epsilon} \sim 9 \times 10^7 \,{\rm yr}, \tag{1.32}$$

which implies that CIV clouds are being stirred on a time scale significantly smaller than a Hubble time. Finally, it is possible to conclude that the turbulence [67] observed near the mean redshift $< z > \sim 2.7$ has been produced by recent events typical of galactic stellar lifetimes.

1.4.2 Radio Scintillation in the IGM

Radio-wave scattering is a generic process that occurs whenever radio waves pass through a medium containing density fluctuations. To date, observable effects have been seen from the Earth's ionosphere (e.g., ionospheric scintillations), the interplanetary medium (e.g., interplanetary scintillations and spectral broadening), and the interstellar medium.

Nevertheless, the IGM would appear to have the characteristic necessary for interstellar scattering to be obtained. For redshifts $z \lesssim 6$, the absence of a Gunn-Peterson trough in quasar spectra indicates that the IGM is largely ionized, and recent far-ultraviolet and soft X-ray observations of highly ionized species (e.g., O VI) along the line of sight to various low-redshift quasars may be a direct detection of the ionized IGM [70, 71, 72, 73]. In the prevailing scenario for large-scale structure formation, most of the baryons are in filamentary structures which are themselves permeated by shocks. Thus, it is expected that the IGM is both ionized and turbulent. Moreover the long path lengths through the IGM (> 100 Mpc) as compared to the ISM ($\sim 1 - 10$ kpc) may compensate for the lower density ($\sim 10^{-7}$ cm^{-3} and 0.025 cm^{-3} respectively).

Detection of intergalactic scattering would be a powerful probe of the IGM, as it would be caused by the majority of the baryons. In particular if compared with the observations of the Lyα forest which probe mostly the neutral component, which represents only about 10^{-5} of the mass.

[74] have considered intergalactic scattering from the general IGM, expanding on previous treatments of scattering from intra-cluster media [75, 76]. The expected dispersion measure (DM), a quantity which measure the amount of dispersion suffered by radio waves, through the IGM for sources with redshifts $z \gtrsim 4$ is

$$\mathrm{DM} \equiv \int_0^D ds\, n_e(s) \gtrsim 1000\,\mathrm{pc\,cm^{-3}} \tag{1.33}$$

where D is the source distance and $n_e(s)$ is the electron density along the line of sight. This value is comparable to path lengths of order of a few kpc through the ISM.

On the other side the expected scattering measure (SM) through the IGM depends upon location of the bulk of the scattering material. If the bulk of the scat-

tering arises in galaxies like the MW (rather than the diffuse IGM)

$$\mathrm{SM} \equiv \int_0^D ds\, C_n^2(s) \sim 10^{-4.5}\,\mathrm{kpc\,m^{-20/3}} \tag{1.34}$$

where C_n^2 are the coefficients of the wavenumber spectrum for electron-density fluctuations.

A better estimation of the SM in the diffuse IGM requires assumptions about the distribution and power spectrum of density fluctuations in the IGM. Assuming an IGM with a structure similar to the one we observe in the ISM, [74] estimates that scattering measures as large as SM$\sim 10^{-3}$ kpc m$^{-20/3}$ may be obtained. Moreover, for the intergalactic scattering an additional wavelength-dependent weighting should be taken into account, favoring scattering material close to the observer, due to the fact that at higher redshifts, the wavelength of the propagating radiation is shorter and scattering is generally less effective.

The main result is that a scatter broadening diameters of order 1 mas are implied, which could be within the planned capabilities of the next very long baseline interferometry on terrestrial baselines (e.g. SKA).

One of the first attempts to apply this scattering physics to a transient object detected by [77] has been reported in [78]. [78] consider the effects of multi-path smearing due to IGM turbulence, finally claiming that the duration of the event is likely dominated by scattering in the IGM and not in the local ISM. If this is the case, it implies that turbulence exists in the IGM down to scales less than $\sim 7 \times 10^7$ m, and a simple argument suggests that the magnetic field in the IGM scattering region is $\gtrsim 4(T_e/10^3\,K)^{1/2}$ nG.

2

The turbulence in the IGM

The IGM is a pervasive, diffuse cosmic baryonic component out of which galaxies form by accretion. In turn, the IGM is replenished with gas and heavy elements carried by galactic outflows. Such dynamical processes hence encode a record of the complex galaxy-IGM interplay.

Observations of metal absorption lines (e.g. C III , C IV, Si III, S IV and O VI) in quasar spectra are a direct probe of this evolution. They show that regions of enhanced IGM density far from large galaxies are polluted with non-negligible amounts of heavies [e.g. 79, 80, 81, 82, 83, 84, 85]. In addition, Lyα forest clouds with neutral hydrogen column density $\log N(HI) > 14$ are metal enriched to $Z \approx 10^{-3}-10^{-2}$ $Z_{\odot}$ [68, 79, 86]; finally, the carbon and silicon abundances of such systems remain roughly constant throughout the redshift range $1.5 < z < 5.5$ [87, 82], although the first signs of a slight decrease above $z = 6$ have been now tentatively reported [88].

Since metals are created in stars inside galaxies, their transport into these distant regions must rely on some yet unknown mechanisms. The most likely one is supernova-driven galactic outflows [89; 90 [FPS]; 91, 92, 93], although different alternatives have been proposed. This hypothesis is supported by a series of observations of galactic winds [e.g. 94, 95, 96, 97] from which one can conclude that (on some spatial scale) galactic wind velocities range from hundreds to thousands of km/s and the mass loss rates are comparable to star formation rates (SFRs).

A complementary piece of information comes from the well-established fact that the interstellar medium (ISM) in galactic disks is turbulent. In particuar, in the

MW pulsar scintillation experiments have convincingly demonstrated that electron density fluctuations in the ISM are characterized by a Kolmogorov spectrum on scales ranging from AUs to kpc (see § 1.2.2).

Turbulence is likely to be to most relevant pressure contribution; its driving may be due to different sources (star formation, stellar outflows, instabilities) acting on specific characteristic scales and injecting different amounts of kinetic energy into the medium; among these, supernova (SN) explosions are thought to be the dominant agent, at least in the star forming regions of galaxies [98, 11, 99]. If both turbulence and metal enrichment are predominantly driven by the same physical phenomenon, i.e. kinetic energy deposition by supernova shocks, then a natural expectation is that IGM gas in enriched regions should show signatures of a turbulent regime.

Some first attempts to measure turbulence in the IGM has been already described in the Introduction (see § 1.4). Another hint of a significant turbulent contribution to the IGM kinetic budget comes from the fact that the median Doppler parameters measured in the Lyα forest are significantly larger than those predicted by cosmological simulations. Again, this implies that some energy in non-thermal form must be injected in the gas to explain the observed line broadening [100, 101].

Quite surprisingly, the properties of intergalactic turbulence have received so far relatively little attention in spite of the insights that its detailed understanding might provide on the galaxy-IGM interplay (FPS; 102; 103). [102] trying to model low-z OVI absorbers concluded that their properties fit observables if and only if sub-resolution turbulence (in practice a density dependent turbulent b-parameter) is added at a level which increases with OVI absorber strength (and hence presumably closer to high density regions hosting galaxies). In addition, stronger absorbers arise from more recent outflows. It is important to note, that turbulence, if present, can also profoundly modify the enrichment patterns through diffusion processes, as pointed out already by FPS. Additional important information might come from investigations of structure formation, during which the released gravitational energy is transferred to the IGM in different forms (e.g. gas entropy, instabilities, cosmic ray acceleration); in particular, turbulence is induced by the vorticity cascade originating at cosmological shocks. This has been investigated throughout cosmological simulations by [104] and [105], who derived the average magnetic field strength and turbulent pressure in the over-density IGM regions outside clusters/groups.

We try to fill the aforementioned gap by investigating in detail the supernova-

driven outflow scenario as a mechanism to pump and sustain turbulence in the IGM surrounding high-redshift galaxies. We investigate the evolution of winds via a semi-analytic approach following both galaxy evolution along its hierarchical growth and the expansion of supernova driven superbubbles as they escape from the halo potential well. With such results in hand, we model turbulence evolution within wind shells using a novel approach based on the spectral transfer equation. This approach allows to derive the turbulent energy density deposited by galactic winds in the IGM, along with its spectral features and dissipation time scales, and to predict the corresponding thermal/kinetic evolution of the IGM.

2.1 The model

In this Section we describe how we determine the evolution of the turbulent energy of the deposited by galactic outflows into the IGM. First, we introduce the galaxy formation model, allowing a precise description of both the SF history and the SN feedback along the galaxy merger tree (MT). These results are then used as inputs to model the evolution of pressure-supported bubbles through the solution of dynamical equations and the turbulence energy spectrum evolution within them.

2.1.1 Cosmic star formation history

The semi-analytic model we introduce in this Section to describe the evolution of a galaxy along its MT is similar to the one by [106] with the improvements introduced by [107] (see also § 4.1 in which a brief description of the full model is presented). Since for this work we are not interested in following the chemical enrichment in detail, we use a simplified approach described in the following.

In hierarchical models of structure formation, such as ΛCDM, the formation of a DM halo trough accretion and repeated mergers can be described by a MT [108]. MTs, which list the progenitors of a given halo at different redshifts and describing how and when these merge together, contain essentially all the necessary information about the dark matter content of halos to build realistic model of galaxy formation as demonstrated by a long-standing practice in the field [109, 110].

The MTs can be extracted from N-body simulations [111] or generated by Monte-Carlo algorithms [112]. In this work we compute the mass growth histories of DM

halos using the second method using a public code[1] based on the EPS theory [113], as improved by [114], to which we defer the reader in numerical details. As an input, we use a WMAP5[2] cosmological parameters and power-spectrum. As an output, we obtain many realizations of the MT for a given halo mass M_0 at a certain final redshift $z_{\rm f}$; each realization lists all progenitors of M_0 at different redshifts, following the related merging histories down to a mass of $M_{\rm res}$.

In our model all the proto-galaxies virializes with a gas mass fraction of 1/6. The neutral gas in these mini-halos cannot cool via atomic hydrogen and relies on the presence of molecular hydrogen, H_2, to cool and collapse, ultimately forming stars. Since we assume that feedback effects rapidly suppress star formation in the first minihalos and that only Lyα cooling halos ($T_{\rm vir} > 10^4 K$) contribute to the SF history of the galaxy, we choose $M_{\rm res} = M_4(z = 20)$ where $M_4(z)$ is the mass corresponding to a halo with virial temperature of 10^4 K at redshift z, given

$$M_4(z) \approx 10^8 M_\odot \left(\frac{10}{1+z}\right)^{3/2} \tag{2.1}$$

(for an exact expression see [116]) and $z = 20$ is the starting redshift of our simulation. Note that the value of $M_{\rm res}$ sets the limit between *progenitors* and *mass accretion*, since the galaxies above $M_{\rm res}$ experience star formation and stellar feedback, ultimately changing their gas content, whereas objects below this threshold retain their original gas content fraction during their evolution, which is finally inherited by another halo in the next hierarchy level.

Star formation in gas clouds occurs on a free-fall timescale $t_{\rm ff} = (3\pi/32G\rho)^{1/2}$ where G is the gravitational constant and ρ is the total (dark+baryonic) mass density inside the halo. The star formation efficiency of a galaxy is then modeled as a fraction, ϵ_*, of the free-fall time:

$$\psi(z) = \epsilon_* \frac{M_{\rm g}(z)}{t_{\rm ff}(z)} \tag{2.2}$$

where ϵ_*, represents a free parameter of the model and $M_{\rm g}$ represents the gas mass in the halo which has not yet been converted into stars.

According to the standard scenario for galaxy formation the gas inside the galaxy

[1] `http://star-www.dur.ac.uk/~cole/merger_trees`

[2] We adopt a flat ΛCDM cosmological model with $h = 0.72$, $\Omega_b = 0.044$, $\Omega_m = 0.26$, $n_s = 0.96$ and $\sigma_8 = 0.8$ consistent with the five-year WMAP parameter analysis [115].

is depleted by various feedback processes, the most important being gas-loss driven by SN explosions. In fact, SN explosions may power a wind which, if sufficiently energetic, may overcome the gravitational pull of the host halo leading to expulsion of gas and metals into the surrounding IGM. To model this process, we compare the kinetic energy injected by SN-driven winds with the minimum kinetic energy of a mass $M_{\rm w}$ to *escape* the galactic potential well [117, 118, 119]. The mass of gas ejected from the galaxy is computed from the equation:

$$\frac{1}{2}M_{\rm w}v_e^2 = E_{SN} \tag{2.3}$$

where

$$E_{SN} = \epsilon_{\rm w}N_{SN}\langle E_{SN}\rangle \tag{2.4}$$

is the kinetic energy injected by SNe and $v_e^2 = GM/R_{vir} = 2E_b/M$ is the escape velocity of the gas from a halo with mass M and binding energy E_b given by [116]:

$$E_b = \frac{1}{2}\frac{GM^2}{R_{vir}} = 5.45\times10^{53}\left(\frac{M_8}{h^{-1}}\right)^{5/3}\left(\frac{1+z}{10}\right)h^{-1}\,{\rm erg} \tag{2.5}$$

In Eq. 2.4, $\epsilon_{\rm w}$ is a free parameter which controls the conversion efficiency of SN explosion energy in kinetic form, N_{SN} is the number of SN, and $\langle E_{SN}\rangle = 1.2\times10^{51}$ erg is the average SN explosion energy (not in neutrinos). Differentiating with respect to time Eq. 2.3 we find that the gas ejection rate is proportional to the SN explosion rate:

$$\dot{M}_{\rm w} = \frac{2\epsilon_{\rm w}\langle E_{SN}\rangle}{v_e^2}\dot{N}_{SN} \tag{2.6}$$

In our model we only consider Type II SNe (pair-instability supernovae are neglected as PopIII stars do not contribute significantly to the total SFR [120]); hence we calculate $N_{\rm SN}$ by integrating the adopted IMF (see below) in the canonical supernova range 8-100 $M_\odot$. For any star forming halo of the galaxy hierarchy, we therefore solve the following system of differential equations:

$$\dot{M}_*(z) = [1-R(z)]\;\psi(z) \tag{2.7}$$

$$\dot{M}_{\rm g}(z) = \dot{M}_a(z) - [1-R(z)]\;\psi(z) - \dot{M}_{\rm w}(z) \tag{2.8}$$

The first equation simply defines the SFR. In our model, we have assumed the

Instantaneous Recycling Approximation (IRA, [121]), according to which stars are divided in two classes: those which live forever, if their lifetime is longer than the time since their formation and those which die instantaneously, eventually leaving a remnant. The transition mass between the two possible evolutions, or turn-off mass ($m_{\rm to}$), has been computed at any considered redshift. Under IRA, the *returned fraction*, that is the stellar mass fraction returned to the gas through winds and SN explosions is:

$$R(z) = \frac{\int_{m_{\rm to}(z)}^{100 M_\odot} [m - w_m(m)]\phi(m) dm}{\int_{0.1 M_\odot}^{100 M_\odot} m\phi(m) dm} \tag{2.9}$$

where $\phi(m)$ is the IMF of the newborn PopII/I stars and it is assumed to have the form:

$$\phi(m) = \frac{{\rm d}N}{{\rm d}m} \propto m^{-1+x} \exp\left(-\frac{m_{\rm cut}}{m}\right) \tag{2.10}$$

with $x = -1.35$, $m_{\rm cut} = 0.35$ M$_\odot$ and m in the range $[0.1, 100]$ M$_\odot$ [122]. The quantity $w_m(m)$ represents the mass of the stellar remnant left by a star of mass m which explodes as SN. We have used the grid of models by [123] for intermediate mass stars ($0.9 < m < 8$ M$_\odot$) and [124] for massive stars ($8 < m < 40$ M$_\odot$).

The second equation describes the mass variation of cold gas: the latter increases due to *accretion* and it decreases both because of astration and mass loss due to SN winds. To model gas accretion we assume that if a new halo virializes out of the IGM gas it forms with a cosmological gas fraction $f_b = \Omega_b/\Omega_m = 1/6$, whereas if it results form the merging of two already existing halos its gas content is simply the sum of the gas mass of the progenitors. Similarly, during the merger, the stellar mass of the new galaxy is assumed to be the sum of the stellar masses of the progenitors. The model free parameters ($\epsilon_{\rm w}$ and ϵ_*) are fixed to match the global properties of the MW as we will discuss in more details in the next Section.

2.1.2 Bubble evolution

In our simulation galactic outflows are treated as pressure-driven bubbles of hot gas emerging from star-forming galaxies. They expand working against IGM pressure, and are driven by the energy injected by multi-SN explosions. Most of the swept-up mass, both in the early adiabatic and in the following radiative phases, is concentrated in a dense shell bounding the hot over-pressurized interior.

Galactic bubbles are canonically studied by using the thin-shell approximation [125, 126, 127], which has been checked against numerical simulations giving excellent agreement [128]. The shell expansion, whose radius is denoted by R_s, is driven by the internal energy E_b of the hot bubble gas. The pressure of such a gas (with adiabatic index 5/3) is therefore $P_b = E_b/2\pi R_s^3$. Hence, momentum and energy conservation yield the following relevant equations:

$$\frac{d}{dt}(V_s \rho \dot{R}_s) = 4\pi R_s^2 (P_b - P) - \frac{GM(R_s)}{R_s^2}\rho V_s \tag{2.11}$$

$$\frac{dE_b}{dt} = L(t) - 4\pi R_s^2 P_b \dot{R}_s - V_s \bar{n}_{H,b}^2 \Lambda(\bar{T}_b) \tag{2.12}$$

where the subscripts s and b indicate shell and bubble quantities, respectively. The volume enclosed by the shell is $V_s = (4\pi/3)R_s^3$, and ρ is the density of the ambient medium taken to be equal to the halo gas density distribution (assumed to have an isothermal profile) within R_{vir}, and to the IGM background density outside the virial radius. Finally, $\bar{n}_{H,b}^2 \Lambda(\bar{T})$ is the cooling rate per unit volume of the hot bubble gas, whose average hydrogen density and temperature are $\bar{n}_{H,b}$ and $\bar{T}$, respectively.

The right-hand side of Eq. 2.11 represents the momentum gained by the shell from the SN-shocked wind; the right-hand side of Eq. 2.12 describes the mechanical energy input, the work done against the shell, and the energy losses due to radiation. The mechanical luminosity is defined as $L(t) = \mathrm{d}E/\mathrm{d}t$ where E is the energy produced by the total contribution of N_{SN} SNe with efficiency ϵ_{w} and energy $\langle E_{SN} \rangle$. Note that, as the bubbles sizes are always much smaller that the horizon scale, the cosmological terms in the above equations can be safely neglected.

To determine the pressure of the ambient medium inside halos we make further assume that the gas is at the virial temperature [129]; outside R_{vir}, the IGM is taken to behave as an ideal gas photo-heated by the UV-background radiation to temperature calculated as in, e.g. [130]. Note that, even prior to reionization, the IGM into which the bubble expand will be locally ionized and heated to roughly the same temperature by the SN progenitor stars.

We notice here that the bubble reaches very rapidly the virial radius, so that these bubbles are practically expanding in the IGM for most of their time. To see this, we consider as in [127] a typical objects virializing at high-redshift ($z = 9$) with an halo mass $M = 10^8 h^{-1}$ $\mathrm{M}_\odot$. At these epochs, the dark matter halo of a subgalactic system will be characterized by a virial radius

$$R_{\rm vir} = 0.76 M_8^{1/3} h^{-1} \left(\frac{1+z}{10}\right)^{-1} \ {\rm kpc} \tag{2.13}$$

The Sedov solution (which is a good approximation of the equation systems when the ambient gas pressure, gravity and cooling can be neglected) predicts that the shell radius evolves according to: $R_s = (125/154\pi)^{1/5}(Lt^3/\rho)^{1/5}$; assuming a constant luminosity of 10^{38} erg^{-1}, we find that the time taken to reach $R_{\rm vir}$ is $\sim 10^7$ yr. This time happens to be smaller than the Hubble time at that redshift.

The cooling function (represented by $\Lambda(T)$ in Eq. 2.12) depends on the hot bubble density, temperature and metallicity (Z). In principle, one could compute an average metallicity of the bubble, but for simplicity we assume for this quantity a constant value $Z = 0.1 Z_\odot$, noting that the final results are very slightly dependent on this choice within a reasonable range. The cooling rates due to gas radiative processes are taken from [131]; the other relevant cooling agent is inverse Compton cooling off CMB photons [132], which is dominant at higher redshifts.

To determine the cooling rate of the bubble (which depends on the density and the temperature of the hot interior) we need an additional relation. As in [127], by equating the rate at which gas is injected from the shell into the cavity with the conductive evaporation rate we obtain an equation for the evolution of the temperature T_b:

$$\frac{{\rm d}T_b}{{\rm d}t} = 3\frac{T_b}{R_s}\dot{R}_s + \frac{T_b}{P_b}\dot{P}_b - \frac{23}{10}\frac{C_1}{C_2}\frac{kT_b^{9/2}}{R_s^2 P_b} \tag{2.14}$$

where $C_1 = 16\pi\mu m_p \eta/25k$ and $C_2 = (125/39)\pi\mu m_p$ and $\eta = 6\times10^{-7}$ (c.g.s. units) is the classical Spitzer thermal conduction coefficient (we have assumed a Coulomb logarithm equal to 30 and neglected possible conductive saturation effects). This relation closes the system of Eqs. 2.11 and 2.12.

Another important quantity to determine the fate of the wind, is the total mass in the shell, M_s, since the energy required to accelerate it increase with its mass. The shell grow rate $\dot{M}_s$ is wind mass deposition rate (Eq. 2.3) and the rate at which gas is swept-up from the galactic environment (for $R_s \leqslant r_{\rm vir}$) or from the IGM ($R_s > R_{vir}$):

$$\frac{{\rm d}M_s}{{\rm d}t} = \dot{M}_w + 4\pi\rho R_s^2 \frac{{\rm d}R_s}{{\rm d}t} \tag{2.15}$$

The velocity of the shock front decreases during the time because of adiabatic expansion and cooling of the bubble, it might happens the shock velocity equals the

intergalactic gas sound speed, in this case we assume the dynamics of the wind joins the Hubble flow and no more mass is accreted.

Since the Eqs. 2.11, 2.12 and 2.14 requires an initial condition which cannot be $R_s = 0$ (no bubble) to be consinstelly solved, we used the Sedov solution for a very short time with respect to $t_H(z = 20)$ to obtain the *primordial* bubble to follow the evolution. The evolutionary equations (Eqs. 2.11, 2.12 and 2.14) can be integrated numerically to follow the evolution of the shell along with the thermodynamic properties of the bubble for a given halo.

A final point concerns the treatment of bubbles when two halos merge along the hierarchical merger tree. In that case, we impose mass conservation, i.e. the mass the new shell is the sum of the masses M_s^1 and M_s^2 of the two progenitor bubbles, that is $M_s^f = M_s^1 + M_s^2$. Similarly, the final volume is taken to be the equal to sum of the volumes of the two single cavities $V_b^f = V_1^f + V_2^f$, and by the adopted spherical symmetry, we update the shock radius as $R_s^f = \left[(R_s^1)^3 + (R_s^2)^3\right]^{1/3}$. Finally, the shock velocity is given by the momentum conservation, which states that $v_s^f = \tilde{M}_s^1 v_s^1 + \tilde{M}_s^2 v_s^2$ where $\tilde{M}_s^i = M_s^i/(M_s^1 + M_s^2)$, and the new internal energy is the sum of the progenitor bubbles internal energies, that is $E_b^f = E_b^1 + E_b^2$. The gas temperature in the merged bubble is computed by assuming the final thermal pressure is the sum of the thermal pressures of the merging bubble: $T_b^f = \tilde{\rho}_b^1 T_b^1 + \tilde{\rho}_b^2 T_b^2$ where $\tilde{\rho}_b^i = \rho_b^i/(\rho_b^1 + \rho_b^2)$.

2.1.3 Turbulence evolution

In order to model the evolution of the turbulence developed in the expanding shells we adopt in the following an approach based on the spectral transfer equation derived by [11] (hereafter NF96) based on the hydrodynamic Kovasznay approximation that was already introduced in § 1.1.2. Our aim is to derive ensemble properties of the turbulent spectrum. A caveat must be made here. The assumption underlying the description presented in § 1.1.2 is one of incompressible, homogeneous, isotropic turbulence. This assumption clearly fails in the highly compressive IGM. However, the bulk of our knowledge on turbulence comes from terrestrial laboratory experiments, and most of them deal with liquids; in addition, simulations of compressible turbulence [133, 134, 135] have shown that nonlinear interactions rapidly transfer most of the energy to non-compressible modes, in final one can use those results at least as a reasonable guide when discussing compressible turbulence.

To model $\mathcal{S}(k,t)$ we assume that turbulent motions in the outflow are induced by interacting blast waves. That is, we maintain that observed turbulent motions in the shell are ultimately derived from the kinetic energy of SN induced shock waves which can act as source function for the turbulent cascade with an efficiency of order unity. If this is the case, there are some general constraints on the form of the source function. [136] have studied in detail the shock-induced turbulence phenomenon, and conclude that the turbulent spectrum has, for the [98] model for the SN shock-wave expansions, a k^{-2} dependence in the short-wavelength regime, while for long wavelengths it is proportional to k^2. Thus, the simplest source function retaining this behavior is

$$\mathcal{S}(k,t) = S_0(t) f(k/k_0) \tag{2.16}$$

where $f(x) = x^2/(1+x^4)$, k_0 is the wave-number corresponding to the characteristic length at which the turbulence is injected (and assumed to be $k_0 \sim 1/R_s$) and $S_0(t)$ is a normalization factor obtained by equating the k-integral of the source function to the kinetic energy rate ($\dot{E}_{\rm kin}$). Finally, as in [137] we use a constant kinematic viscosity of $\nu = 5 \times 10^{24}$ cm^2 s^{-1}; this is equivalent to scale the dynamic viscosity coefficient with density.

The spectrum evolution is followed for each halo of the MT; again, we need to specify how we treat merger events. To conserve turbulent energy associated to any MT node we assume

$$\rho\mathcal{E}(k) = \rho_1\mathcal{E}_1(k) + \rho_2\mathcal{E}_2(k), \tag{2.17}$$

which entails

$$\mathcal{E}(k) = \frac{M_1 R_s^3}{M R_{s1}^3}\mathcal{E}_1(k) + \frac{M_2 R_s^3}{M R_{s1}^3}\mathcal{E}_2(k). \tag{2.18}$$

The turbulent pressure is finally given by

$$p_t(t) = \rho \int_0^\infty {\rm d}k \mathcal{E}(k,t). \tag{2.19}$$

2.2 Results

In this Section we present the results of our model. After a description of the model calibration, useful to fix the model free parameters, we give our prediction for the bubble evolution along a MT extending down to $z = 0$ along with the IGM

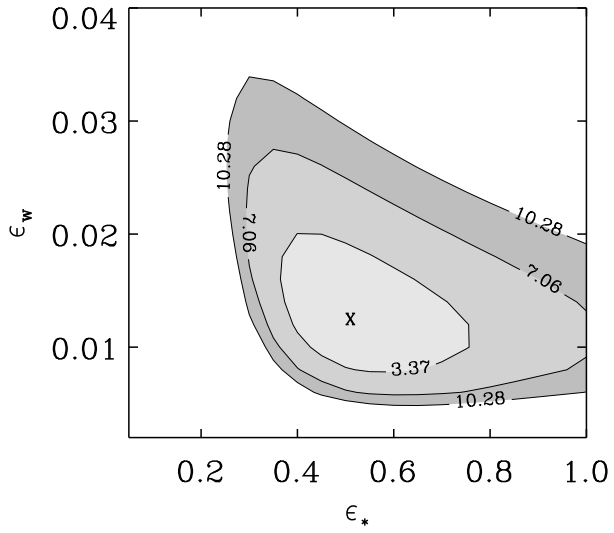

Figure 2.1 The 68%, 95%, 99% confidence level regions of our galaxy model are represented in the $(\epsilon_{\rm w} - \epsilon_*)$ plane.

turbulence properties.

2.2.1 Model calibration

Our galaxy evolution model includes several relatively poorly known (albeit important) physical processes that need to be empirically calibrated. To this aim we have used the observed properties of the MW as a benchmark to fix the best values for the two model free parameters: ϵ_*, the efficiency of star formation (Eq. 2.2) and $\epsilon_{\rm w}$, the SN feedback efficiency (Eq. 2.3). This has been accomplished by producing the MT of a dark matter halo with mass consistent with the MW one [10^{12} $M_\odot$, 139] at redshift $z = 0$. We have then compared the resulting properties of the synthetic galaxy with the following ones deduced from MW observations:

- Stellar mass. Contributions to the stellar mass come from the disk $M_*^{disk} \sim (4-6) \times 10^{10} M_\odot$, the bulge $M_*^{bulge} \sim (0.4-1) \times 10^{10} M_\odot$, and the halo $M_*^{halo} \sim (0.2-1) \times 10^{10} M_\odot$ components [140, 141], yielding a total stellar mass of $M_* \sim 6 \times 10^{10} M_\odot$.

- Gas-to-stellar mass ratio, $M_{gas}/M_* = 0.13$. The mass of gas has been derived using the observed mass of HI and HII regions of the Galaxy, $M_{gas} = M_{HI} + M_{HII} \sim (6+2) \times 10^9 M_\odot$ [142].

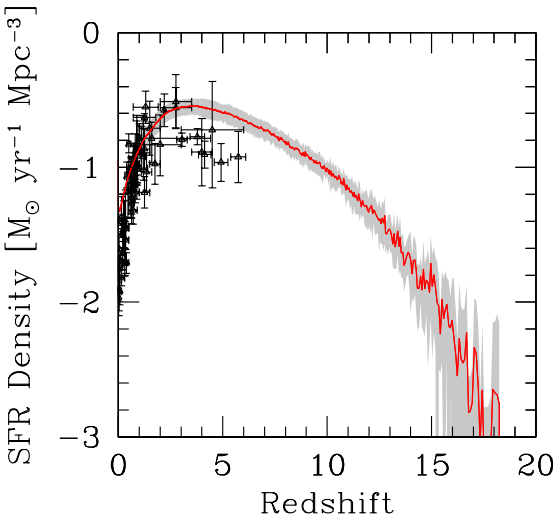

Figure 2.2 Redshift evolution of the SFR density along the MW merger tree for our best-fit model ($\epsilon_* = 0.5, \epsilon_w = 0.012$. The curves are obtained after averaging over 100 realizations of the MT; shaded areas denote $\pm 1\sigma$ dispersion regions around the mean. Points represent the low-redshift measurements of the cosmic SFR by [138].

- Current star formation rate. [143] use the total free-free emission in the WMAP foreground map as a probe of the massive star population and derive a global SFR of 1.3 $M_\odot$ yr^{-1}.

For all these observables we assume a relative uncertainty of 20%. Fig. 2.1 shows the χ^2 confidence levels of our model with respect to these observables as function of ϵ_* and ϵ_w. The distribution presents a clear minimum at $(\epsilon_*, \epsilon_w) = (0.5, 0.012)$; however, a degeneracy exists with a relatively wide range of choices that can reproduce with sufficient accuracy the global MW properties. Thus, the best-fit model implies a star formation timescale which is only a factor ≈ 2 longer than the free-fall time and a relatively inefficient feedback in order not to expel from very first proto-galaxies too much gas which will then be crucial to fuel the subsequent SF in larger objects.

From the same run we can obtain the redshift evolution of the SFR density along the MW merger tree for our best-fit model, after averaging over 100 different realization of the MT[3]. For comparison sake only, we overplot the cosmic SFR on top of the MW SFR history. Perhaps not coincidentally, the two evolutions match each other quite well indicating that the Galaxy is a not too biased tracer of average

[3]The effective comoving volume of the MW is taken equal to 30 Mpc^3, and corresponds the size of a 10^{12} $M_\odot$ linear fluctuation.

cosmic conditions.

In the remainder of the chapter we assume that these values for $(\epsilon_*, \epsilon_{\rm w})$ hold for any galaxy present in the MT. This might a poor approximation, but given the persisting ignorance on star formation and feedback processes a better performance of more complex choices is not guaranteed to produce a more solid result. In any case the model success in reproducing key Galactic properties provides at least a first and necessary step towards more refined treatments.

2.2.2 Galactic outflows

We illustrate the properties of galactic outflows by focusing on the case of the progenitors of a 10^{13} $M_\odot$ halo at redshift $z = 0$ (i.e. a small cluster/group). Since the total number of galaxies at any intermediate redshift is very large we will deal with *mean* quantities to describe the global properties of the winds. This precludes the inspection of one-to-one relationships between galaxy and its wind properties, but will make possible to appreciate the correlations among several global quantities, as we will see in the following.

Fig. 2.3 gives concise overview of the bubbles we have identified around galaxies at selected redshifts ($z = 10, 6, 3, 1$) and it can be used to elucidate many physical aspects. Bubbles tend to become older towards lower redshifts with a decreasing age spread; their ages tend to accumulate close to the Hubble time. This behavior reflects the fact that after an early evolutionary phase in which bubbles grow by number around relatively low-mass objects, the average growth of the halo population mass associated with deeper potential wells, prevents the formation of new bubbles after $z = 3$. Hence most of the bubbles seen around galaxies at intermediate redshifts ($z = 3 - 5$), where they are more easily observed, contain material expelled by galaxies at a much earlier time. At the same time old bubbles merge together to form a fewer large ones. The role of merging events is made clear by the solid curves in the top panels which show the distribution of merging events for halos that have witnesses at least 1 merging event. A fraction M/N, indicated by the labels inside the panels in Fig. 2.3, have evolved in isolation until the considered z, i.e. they never suffered a merger. Such ratio decreases steadily with time, going from 81% at $z = 10$ to 0 at $z = 1$. The merging activity increases the average ages of bubbles: as discussed above, at high z a large number of young, isolated bubbles exist that are later turn into aged, large ones.

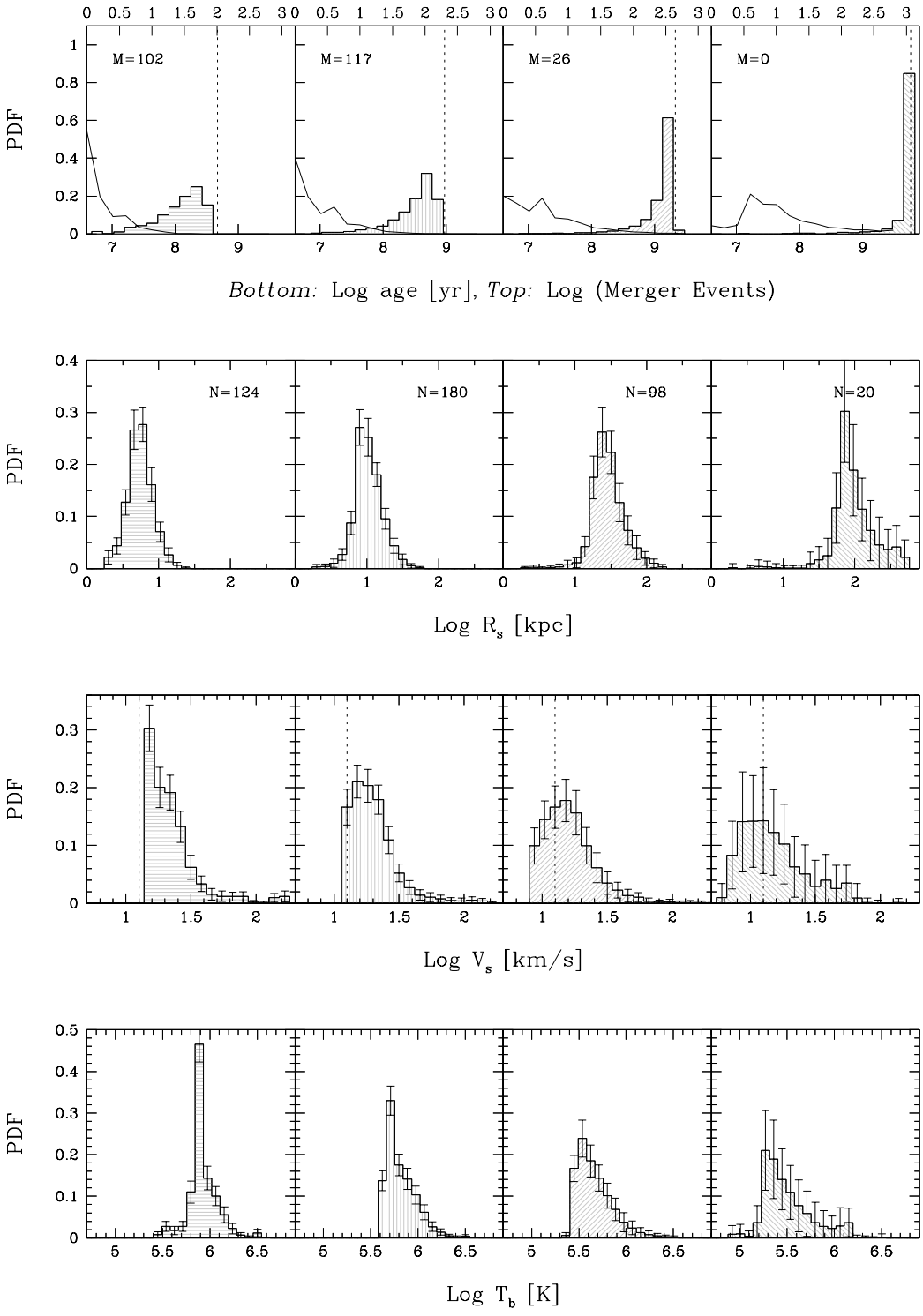

Figure 2.3 Probability Distribution Function (PDF) for different bubble properties at different redshifts (left to right) $z = 10, 6, 3, 1$; error bars show the 1σ dispersion. The solid curves in the top panels show the distribution of the number of mergings for the halos in the MT. The label M indicates the number of halos that evolved in isolation up to that redshift; N indicates the total number of halos at that z. The dashed lines in the top panels marks the age of the universe at that redshift. The dashed lines in the third row panels marks the IGM sound speed at that redshift.

The typical bubble size grows from 5 kpc (physical) at $z = 10$, to about 100 kpc at $z = 1$. Merging is definitely an important agency behind this evolution; however, it cannot be the only growth factor for bubbles. This can be realized by combining the information from the age and size distributions. At the lowest redshifts shown in Fig. 2.3, the bubble age distribution essentially collapses onto the cosmic age value; nevertheless, we a considerable size spread, ranging from 1 to a few hundred kpc, exists. Such spread is caused by the corresponding dispersion of galaxy star formation rates. Larger galaxies tend to have faster winds, which show up as a tail in the PDF of the shock velocity distributions ($V_s > 30$ km s^{-1}). Hence a minority of the bubbles found at $z < 3$ are constituted by old bubbles which are still powered by their current galaxy, which is undergoing vigorous star-formation. Instead of creating a new bubble, these massive cluster progenitors blow their winds into pre-existing, old bubble structures.

From the velocity PDF evolution, it is interesting to note that at early times bubbles (somewhat contrary to naive expectations) expand on average at larger velocities and they tend to decelerate at lower redshifts. This is an obvious implication of the aging trend described above. As larger galaxies dilute their energy on the larger volume of pre-existing cavities, they can sustain the growth of bubbles but cannot re-accelerate them to the high velocities at which they were traveling in the past.

The evolution of the bubble temperature T_b (Fig. 2.3) is governed by competing effects. Adiabatic expansion and radiative cooling (depending on bubble gas temperature and, to a much limited extent, gas metallicity) lead to a decrease of T_b, while thermalization of the wind energy provide a heat input. Almost all the bubbles have temperatures $> 10^{5.5}$ K at $z = 10$, whereas by $z = 3$ this fraction decreases to $< 20\%$. This is mainly due to the adiabatic expansion of the bubbles. The expanding outflow is powered by the continuous injection of SN energy both in kinetic (in practice stored in the shell, where most of the mass is located) and thermal (stored in the bubble interior) forms. More quantitatively, from Fig. 2.4 one can appreciate that the kinetic energy is always dominant (by a factor 2-3) with respect to the internal one. This kinetic energy will be rapidly converted in disordered motions by instabilities, finally resulting in a fully developed turbulent spectrum. The bubble volume filling factor also increases with time, as illustrated in the bottom panel of the same Figure, reaching about 10% at $z < 2$. One has to keep in mind that our

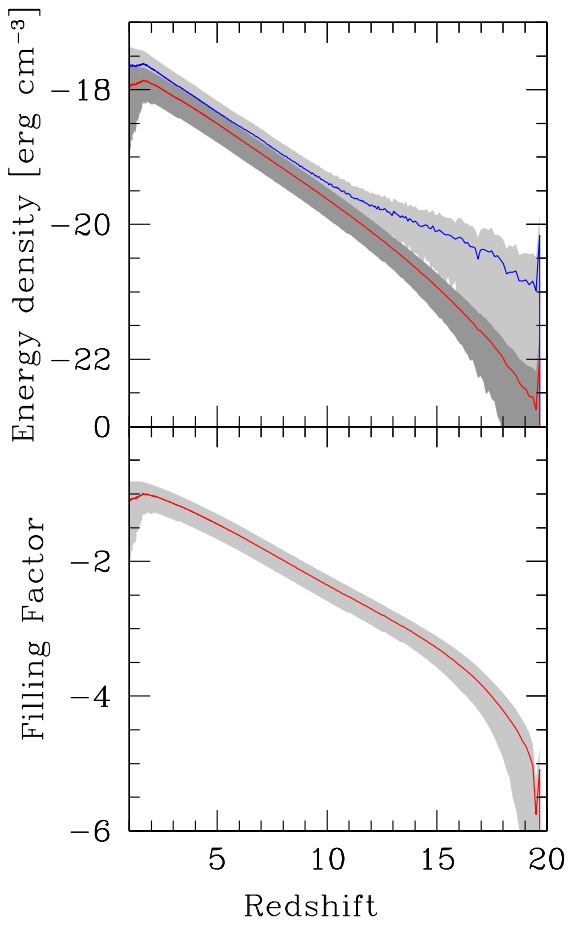

Figure 2.4 *Top:* Mean kinetic (blue) and thermal (red) energy of regions affected by outflows at different redshifts. *Bottom:* Volume filling factor of outflows. Shaded areas show 1σ dispersion around the mean (solid curve) of 100 merger tree realizations.

study is based on the MT of a cluster/small group and therefore it might reflect a somewhat biased cosmic regions, although we do not expect major differences as we extrapolate these results to general IGM. A similar treatment of the outflow evolution has been successfully used by [144] and [145] to investigate the role of galaxies in enriching the IGM. In particular [145] use the modified PS formalism to follow the evolution of halos and porosity-weighted averages to investigate the global influence of winds. For a reasonable choice of the model free-parameters, they find that outflows can generally escape from the low mass halos ($M_h < 10^9\,M_\odot$) which then dominate the observed enrichment; nevertheless, MW-type galaxies can create Mpc-size metal enriched bubbles in their surroundings. [144] apply the semi-analytical prescription for galactic winds to high-resolution N-body simulations of field galaxies. Their main conclusion is that galactic outflows do no perturb the structure of the Lyα forest, galaxies with $10^9 < M_* < 10^{10}$ are the main responsible for IGM chemical enrichment at $z = 3$.

The bubble volume filling factor is a useful tool when applying our models to quantify turbulent effects in the quasar absorption line spectra, as we will try to do later on. As a note of caution, the filling factor shown in Fig. 2.4 might be overestimated to some degree as we do not attempt to account for possible, although likely rare, overlaps between bubbles.

2.2.3 Turbulence evolution

The best way to observationally probe the turbulent content of gas affected by outflows is to measure the Doppler parameter, b, of absorption lines arising from kinetically perturbed gas. For this reason in the following we will use b to quantify turbulence evolution.

In general, one can write b as the quadratic sum of the thermal and turbulent components,

$$b = (b_{\rm th}^2 + b_{\rm t}^2)^{1/2}, \tag{2.20}$$

where

$$b_{\rm th} = \left(\frac{2k_B T}{m_a}\right)^{1/2} \tag{2.21}$$

is the thermal contribution and

$$b_{\rm t} = \sqrt{\frac{p_{\rm t}}{\rho}} \tag{2.22}$$

is the contribution due to the turbulent pressure defined in Eq. 2.19. Note that the turbulent contribution (contrary to the thermal one) does not depend on the mass m_a of the atomic mass of the absorbing element. This allows to generalize our results to all species associated with the cold HI shell gas (e.g. CIV). Moreover, since the observed Doppler parameter is the sum of the two contributions and the thermal broadening is smaller for heavier elements, the relative contribution of turbulent broadening should more important (and hence more easily detectable) for heavier elements. In Fig. 2.5 we show the distribution of Doppler parameters in simulated galaxies at different redshifts. The b_t distribution function at all redshifts shows a similar shape, with a low-energy cut-off, followed by a maximum and a steed declining tail towards larger values. However, the PDF shift towards lower b_t values with time: while at $z \geqslant 6$, the region affected by the winds can become very turbulent, reaching in a few spots $b_t > 50$ km s^{-1}, as a result of the violently expanding of fresh new bubbles carved by early galactic winds, at later times winds blowing in pre-existing bubbles limit become more gentle, producing in decrease of turbulent broadening effects. By $z \approx 1-2$ the distribution has stabilized on median values of the order of 1-2 km s^{-1}, and even the most turbulent spots do not exceed 25 km s^{-1}. The trend above is further enhanced by the dissipation of turbulent energy with time, which does not allow to store kinetic energy into eddies indefinitely. To see this quantitatively, it is useful to estimate the turbulent dissipation timescale. Under the hypothesis of a fully developed, steady-state spectrum the dissipation timescale is well approximated by the eddy turn-over timescale, namely $t_e \sim R_s/V_s$. If we further assume that to the early stages of bubble evolution the Sedov solution applies, it follows that $t_e \sim 2.5 t_b$, where t_b is the bubble age, in turn shorter than the Hubble time. This implies that, due to their high velocity and relatively small radii, dissipation acts very efficiently at earlier stage, thus decreasing the turbulent energy budget of these objects. We pause briefly to emphasize an important point. One has to keep in mind though (see Fig. 2.4) that the filling factor of the turbulent regions is quite small at high redshift, and therefore it must be made clear that the above is not the b_t parameter applicable to the global IGM, but only to tiny and specific (but well defined) portions of it. By plotting the volume-weighted evolution of $\langle b_t \rangle$, shown in Fig. 2.6, we can find support to the previous statement: at higher redshift the turbulent pressure contribution is less important because of the small size of outflow-affected regions, whereas in local objects the latter grow enough to

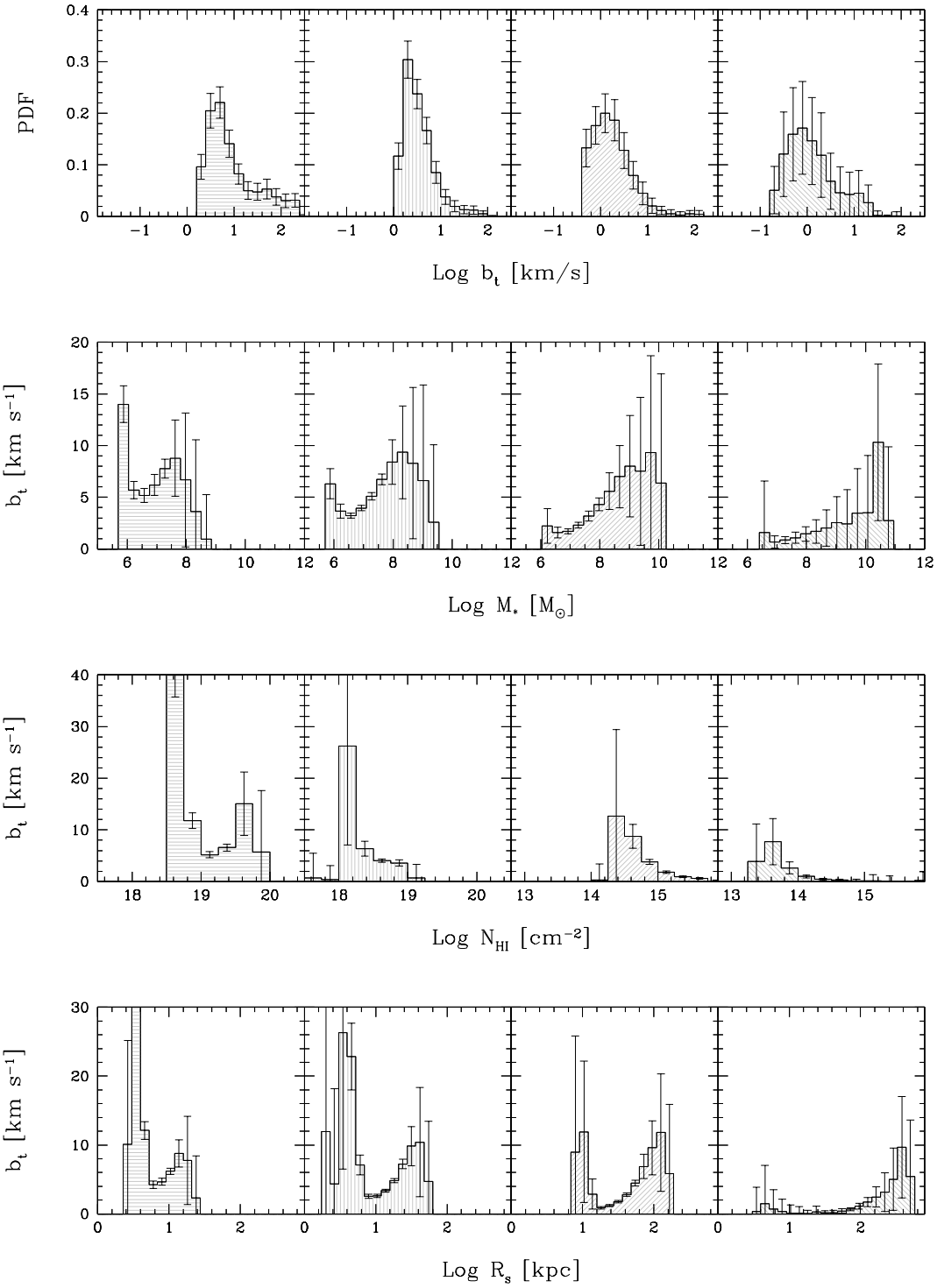

Figure 2.5 Turbulence properties in terms of the Doppler parameter b_t at four selected redshifts: $z = 10, 6, 3, 1$ (left to right columns). The first row contains the PDF of b_t, the others (top to bottom) show the relations between b_t and stellar mass, M_*, hydrogen column density, N_{HI}, shock radius, R_s, respectively. Error bars denote 1σ dispersion in each bin.

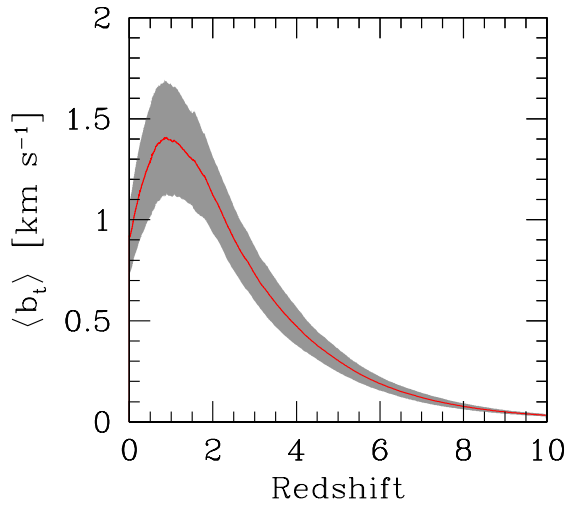

Figure 2.6 Redshift evolution of the volume-weighted Doppler parameter. The solid curve shows the mean; the shaded area corresponds to 1σ dispersion.

occupy a significant fraction of the volume; however, this occurs too late, when dissipation has already started to quench eddies on the smallest scales. The trade-off between injection and dissipation, conspire to produce a maximum in $\langle b_t \rangle$ at $z \approx 1$. Let us turn back to the analysis of the other panels in Fig. 2.5. It is interesting to determine the level of turbulence in bubbles produced by galaxies of different stellar masses. In general, b_t is positively correlated with the stellar mass of a galaxy. This is a consequence of the fact that the SFR (which is ultimately proportional to the energy input rate due to supernovae) is more sustained in larger galaxies. However, we see that the onset of a turbulent regime is almost unavoidable in regions that are stirred by galactic winds. Again, the peak at very low M_* is interpreted as the imprint of young bubbles in which turbulence has not yet suffered from dissipation: we double-checked this hypothesis by studying the correlation in different bubble age bins. This analysis is reported in Fig. 2.7 (for a single MT realization) whose examination clarifies that the youngest bubbles have the largest b_t values. Thus, the bursting star formation activity going on in small galaxies momentarily reverses the trend of increasing b_t as a function of stellar mass, clearly indicating that the level of turbulence depends both on age *and* mass of the object. The spread of the distribution is very limited, suggesting that different mass accretion histories do not influence substantially final Doppler parameter distribution.

A relatively easily accessible observational quantity when studying the IGM is the

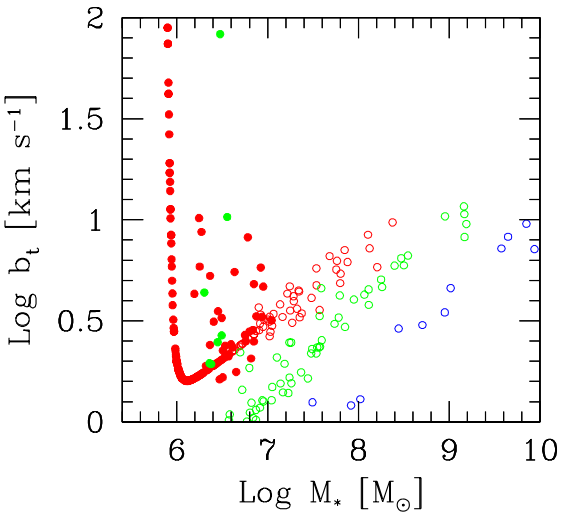

Figure 2.7 The Doppler parameter b_t as a function of the galaxy stellar mass for a single realization of the MT, shown at $z = 6$ (red circles), $z = 3$ (green circles), $z = 1$ (blue circles). The filled points indicate bubble whose age is less than half of the Hubble time.

neutral hydrogen column density, N_{HI}, of the absorbing shell/system. A reasonable estimate for such quantity can be obtained from the following formula:

$$N_H = \int_{R_s - \Delta R_s}^{R_s} n_H(r) dr \approx n_H \Delta R_s = \frac{M_s}{4\pi \mu R_s^2} \tag{2.23}$$

In the latter n_H is the mean density in the thin shell, given by the ratio between its mass (M_s) and its volume V_s:

$$V_s = 4\pi R_s^2 \Delta R_s \tag{2.24}$$

The neutral hydrogen ionization correction can be obtained by solving the appropriate photoionization equilibrium balance equations given, e.g. by [146] and assuming the UV background history of the Universe computed by [147]. The third row of panels in Fig. 2.5 shows the distribution of b_t with N_{HI}. One can note that at redshift $z \sim 3$ the turbulent broadening starts making an impact in HI lines with $N(HI) \geqslant 10^{14}$ cm^{-2}.

Finally, the lowermost panel in Fig. 2.5 shows the correlation between b_t and the distance reached by the outflow. This might have important observational implications. [96] by studying the correlation between galaxies and CIV systems with large velocity spreads, showed that most of these systems are associated with star-

forming galaxies. It is conceivable to interpret such result as a direct evidence of large-scale outflows around $2 \lesssim z \lesssim 3$ galaxies. A similar investigation, as discussed in the next Section, could directly probe the level of turbulence in these objects and test our predictions.

2.2.4 Sanity checks

A direct comparison of our results with the actual level of turbulence in the IGM is not possible since this observable has not been convincingly derived yet. In the meantime, it is possible to perform at least a sanity check for our model as follows.

In order to study the properties of the IGM, a number of high-quality QSO absorption line experiments has been carried on during the last decade allowing the build-up of a large sample of observed systems for which both $N_{\rm HI}$ and the Doppler parameter b have been fitted (see an almost complete list of references in 101). The observed HI column densities cover the range 10^{12-22} cm^{-2} and follow an almost perfect power-law distribution $\mathrm{d}N/\mathrm{d}N_{\rm HI} \propto N_{\rm HI}^{-\beta}$ with $\beta = 1.5 - 1.7$. The Doppler parameters of these systems range over about $10 < b < 100$ km s^{-1}, with the vast majority being concentrated between $15 - 60$ km/s. The observed broadening could be either real, i.e. caused by physical mechanisms (e.g. thermal broadening, turbulence and peculiar motions), or artificial, due to the blending of close systems.

Many authors have suggested the use of the lower-cutoff in the Doppler parameter distribution vs. $N_{\rm HI}$ as a reliable proxy for the gas temperature at a given redshift. Similar approaches has been used by [148] to report evolution in the inferred IGM gas temperature over the range $2.0 < z < 4.5$ and by [149] to extract the *equation of state* of the IGM from the Doppler parameter distribution of the low-density Lyα forest. To make progress we follow this procedure.

In Fig. 2.8 we show the absorber properties derived in a sample of Lyα forests from 22 high-resolution VLT/UVES Large Program QSO spectra [150, 151], selected at redshift $z \sim 3$. To avoid the contamination of absorbers affected by the UV background flux from the QSO, we exclude from our sample absorbers closer than 3000 km/s to the QSO and we also do not consider in our analysis Doppler parameters > 100 km s^{-1} since they are very likely due to errors in the fitting procedure. In the same graph we report our estimated thermal Doppler parameter ($b_{\rm th}$) as a function of $N_{\rm HI}$, obtained from a linear fit of the *minimum* b-values, defined by

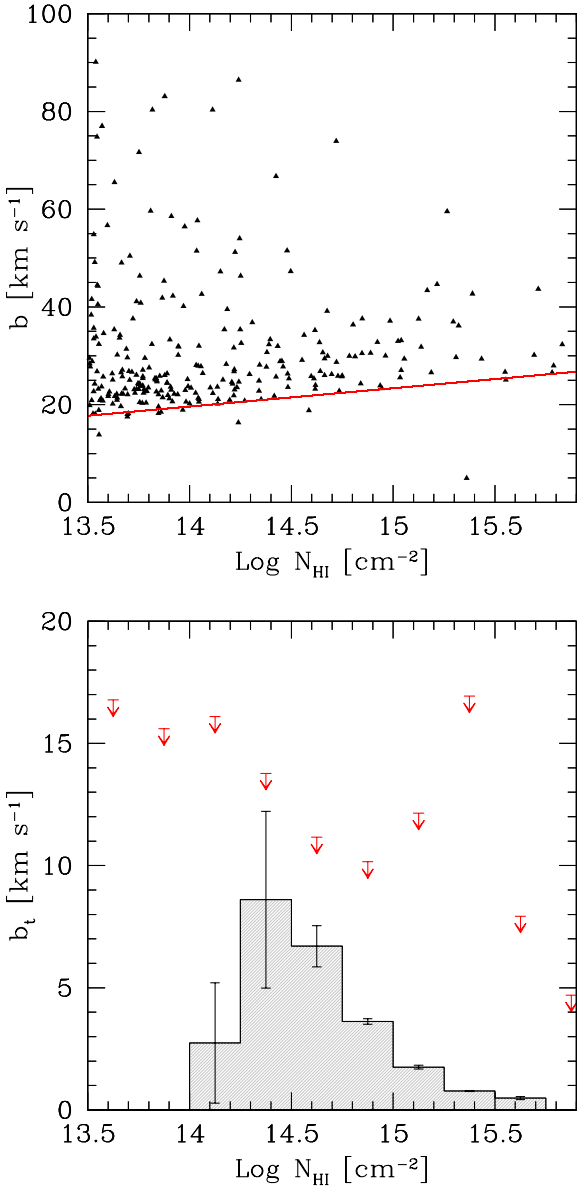

Figure 2.8 *Left panel:* Doppler parameter – HI column density relation observed in the IGM at $z = 3$ (data points from VLT/UVES LP). The red curve represents a fit to the lower cutoff used to derive the thermal contribution. *Right:* Turbulent Doppler parameter distribution at $z = 3$ as predicted by our model (histogram), also reporting 1-σ dispersion. The red arrows show the observational upper limits.

dividing the $N_{\rm HI}$ range in 50 bins and selecting the smaller b-value in each bin.

The sanity check then consists in the comparison of our predicted mean b_t distribution with the analogous average residual Doppler parameters from the data after the thermal contribution has been subtracted. Given the reasons for contamination listed above what we show in Fig. 2.8 cannot be intended as a direct theory-data comparison as the observed broadening still contains a contribution from IGM peculiar motions, which are not directly related to turbulent motions. Hence, the data point must be consider as strict upper limits which our theoretical Doppler parameters should not exceed. Quite encouragingly, this is indeed the case: our model is consistent with the experimental upper limits in the entire HI column density range. The uncertainties in the exact observational determination of b_t does not allow a more meaningful comparison at this stage. This will become possible if in the future Rauch-type experiments using (lensed) quasar pairs will be carried out thanks to the possible increased availability of such systems enabled by the SDSS. As an example of the strong potential of this strategy, [152] have discovered 130 close pairs of QSOs in the SDSS DR5.

As an alternative, the presence of the metal lines in the absorbers could also be used as a possible way to obtain an independent measurement of the IGM turbulent level. The measurements of the Doppler parameters from absorption features corresponding to two or more elements (typically, CIV and SIV) assumed to be co-spatial, allows the separation between thermal and kinematic broadening contributions. As already mentioned in the previous Section, this technique could disentangle the broadening due to the kinematic from the thermal one which is instead mass dependent. To achieve this result high resolution spectroscopy is required in order to properly fit the profile of the absorbers along the QSO los and to determine the redshift of the lines with sufficient precision to make sure that the ions share the same absorber environment. We plan to combine these type of observations with our model in a forthcoming work.

2.3 Conclusions

Turbulence is an important physical process in essentially all astrophysical environments but, it received a relatively meager attention on the scale relevant to

cosmological phenomena. This is partly understood from the difficulty to collect reliable data as observations aimed at the study of these aspects are very challenging. Even more surprisingly though, the well ascertained fact that the IGM is polluted on large scales by heavy elements, carried by powerful winds powered by galaxies, should raise strong suspects that turbulence must pervade the IGM, albeit at levels yet difficult to understand.

To clarify the amount of turbulent energy deposited in the IGM by galactic winds we have developed a simple but physically accurate model based on standard ΛCDM hierarchical structure formation model to identify halos hosting galaxies progenitor of a small cluster/group of total mass $M = 10^{13} M_{\odot}$ at $z = 0$. In addition, the required star formation history in all their progenitors via a merger-tree technique (carefully calibrated to reproduce the Milky Way) is also followed. As these galaxies progress along their history, their collective supernova explosion vent gas, heavy elements and, most importantly for the present study, energy in the surrounding IGM. The evolution of these hot intergalactic bubbles is followed by including all the relevant physics, enabling us to determine their thermodynamic properties at best. We couple then this general galaxy-IGM interplay scenario (which can be used and adapted to a number of ancillary applications as e.g. metal enrichment and SZ effect) to a treatment of turbulence evolution using a powerful approach based on the spectral transfer function developed by [11]. In brief, the major advantage of this method is a relatively straightforward derivation of the turbulent IGM turbulent pressure evolution (see Eq. 2.19).

The main results can be summarized as follows. At $z \approx 3$ the majority of the bubbles around galaxies are old (ages > 1 Gyr), i.e. they contain metals expelled by their progenitors at earlier times, and have a size distribution at that redshift in the range 10-100 (physical) kpc. The velocities reach up to 100 km s^{-1} for larger galaxies but a considerable fraction of the bubbles have already become subsonic and the shock decayed into a sound wave; temperatures in the rarefied bubble cavities are in the range $5.4 < \log(T/K) < 6.5$, i.e. a around a million degrees. The bubble volume filling factor increases with time reaching about 10% at $z < 2$. The energy deposited by these expanding shocks in the IGM is predominantly in kinetic form (mean energy density of 1 μeV cm^{-3}, about 2-3$\times$ the thermal one), which is rapidly converted in disordered motions by instabilities, finally resulting in a fully developed turbulent spectrum. The corresponding *mean* turbulent Doppler

parameter, b_t, peaks at $z \approx 1$ at about 1.5 km s^{-1} with maximum $b_t = 25$ km s^{-1}. More informative though is the b_t distribution associated with individual bubbles and the relations with the galaxy stellar mass and bubble shell column density and radius. The shape of the b_t distribution does not significantly evolve with redshift but undergoes a continuous shift towards lower b_t values with time, as a result of bubble aging. We find also a clear trend of decreasing b_t with $N_{\rm HI}$ and a more complex dependence on R_s resulting from the age spread of the bubbles. We have finally tried to compare our results with available data on the Doppler parameter deduced from QSO absorption line studies of the Lyα forest, but we are facing the difficulty of accurately removing the contamination due to the thermal component and the more troublesome peculiar contribution. Alternatively one can extend our study to make predictions for quasar pairs systems and/or using observations involving different metal species. We are already working along these directions, which in general require additional information of the position of galaxies and therefore the implementation of our turbulent model into a full-scale hydrodynamic simulations.

3

Understanding CRs propagation

The problems of origin and propagation of Cosmic Rays (CRs) in the Galaxy are long standing questions and the combination of several different observations in a wide energy range is required to understand them at least partly.

Much of the difficulty in attempting at answering comes ultimately from the fact that CRs are charged particles. Being charged, they do not propagate on straight lines, but their trajectories are bent by galactic magnetic fields (GMF), hence their arrival directions on Earth do not point back to their sources. Since the ISM in which CRs propagate is a turbulent medium (see § 1.2.2), CRs interacting with randomly oriented Alfvén waves experience diffusion and are possibly convected and reaccelerated during their travel. Therefore, the description of their propagation from source to Earth through the ISM is a hard task, whose degree of accuracy has necessarily grown in the years to account for the large amount of available astrophysical data (see [153] for a comprehensive review).

The most realistic description of CR propagation is given by diffusion models (see § 3.1) which involve a large number of parameters which need to be fixed using several types of experimental data. Their knowledge is crucial not only for CR physics but also for constraining or determining the properties of an exotic galactic component from indirect measurements.

However, in spite of the strong efforts made on both observational and theoretical sides, most of these parameters are still poorly known. One of the reasons lies in the fact that best quality data on CR spectra (e.g. the ratios of secondary to primary nuclear species) were available mainly at low energy ($E \lesssim 10$ GeV/n), where several

competing physical processes (e.g. solar modulation, convection, reacceleration) are expected to affect significantly the CR spectra by an *a priori* undetermined relative amount. Furthermore, the uncertainties on the spallation cross sections and their effects on the propagated CR composition are still sizable at such low energies.

On the other hand, the interpretation of high energy ($E > 10$ GeV/n) CR data is, in principle, easier since in this range only spatial diffusion and spallation losses (the latter becoming less and less relevant with increasing energy) are expected to shape the CR spectra. Furthermore, other uncertainties related to the physics of solar modulation and to poorly known nuclear cross sections are reduced by considering only data at energies larger than several GeV/n. Hence, the study of high energy CR spectra allows in principle to constrain the plain diffusion properties of CR in the Galaxy, in particular the strength D_0 of the diffusion coefficient at a reference rigidity and its energy slope δ, and offers a lever arm to better understand low energy effects (see [154] for an interesting discussion about this issue). This possibility has been precluded for long time by the scarcity of observational data.

The experimental situation however improved recently when the CREAM balloon experiment measured the spectrum of light CR nuclei and especially the boron to carbon ratio (B/C) up to ~ 1 TeV/n [155]. Besides CR nuclear measurements, valuable complementary data were recently provided by the PAMELA satellite experiment which measured the antiproton to proton ($\bar{p}/p$) ratio up to ~ 100 GeV with unprecedented accuracy [156]. Other valuable experimental data are expected to come from AMS-02 [157] which will soon be installed on board of the International Space Station. As for other secondary nuclear species, antiprotons are produced by the spallation of primary CRs (mainly protons and Helium nuclei) in the standard scenario. Therefore, their spectrum may provide an independent and complementary check of the validity of CR propagation models and a valuable probe of an extra component which may arise, for example, from secondary production in the CR astrophysical sources [158, 159] and/or from dark matter annihilation or decay (see e.g. [160, 161, 162, 163]).

Whether the measured secondary/primary nuclear ratios and antiproton spectra are fully compatible within the framework of a standard CR transport model is still under debate. Indeed, while a discrepancy between the parameters allowing to reproduce the B/C and the $\bar{p}/p$ was claimed in [164] (see also [153]), a good concordance was found in other analyses [160, 165]. Furthermore, even the interpre-

tation of nuclear data alone is still confused: analyses based on the leaky-box and semi-analytical diffusion models (see § 3.1) favor values of δ significantly larger than the ones found with the numerical GALPROP package[1]. The comparison of such results is not straightforward due to a number of different assumptions. Hence, an independent analysis accounting for most recent available data it was timely.

Within this work, we contribute to develop a new code called DRAGON (Diffusion of cosmic RAys in Galaxy modelizatiON) [166] to constrain the main diffusion parameters against updated experimental data in the energy range $1 \lesssim E \lesssim 10^3$ GeV/n. This code reproduces the results of the well known GALPROP code under the same conditions. Furthermore, it allows to test the effects of a spatially varying diffusion coefficient. The last version of our code accounts for ionization and Coulomb energy losses, diffusive reacceleration and convection, and exploits the performances of modern computer clusters to scan a rather large range of parameters under realistic physical conditions. Here below, after a brief introduction to propagation models, we present our method to constrain the diffusion coefficient normalization and spectral index, as well as the Alfvèn velocity v_A, with unprecedented accuracy by means of a statistical analysis of the agreement between model predictions and CR data including recent nuclear and antiproton data.

3.1 A brief introduction to propagation models

As we already argued in § 1.3, the high isotropy of low energy CRs and the large number of secondary nuclei, together with data from radioactive isotopes, suggest that high-energy particles travel long time in the Galaxy effectively interacting with the ISM. An important role here must be played by the galactic magnetic field, but due to lack of information about the physical conditions of the ISM, the details of the specific mechanism regulating the propagation of CRs in the Galaxy are still unknown. Therefore, approximate semi-empirical models have been developed, that allow to classify and correlate numerous experimental facts and to interpret some properties of composition, spectra and anisotropy of different components of CRs. Being the galactic magnetic field chaotic at some level, charged particles are generally expected to diffuse into it. It is well known, since the pioneering work of [167], that in

[1] `http://galprop.standford.edu`

the absence of continuos energy losses, re-acceleration and convection, the diffusive transport of stable nuclei in the ISM is described by the following equation:

$$\frac{\partial N_i}{\partial t} + \nabla(\mathbf{D} \cdot \nabla N_i) = Q_i(E_k, r, z) - c\beta n_{\rm gas}(r, z)\sigma_{\rm in}(E_k)N_i + \sum_{j>i} c\beta n_{\rm gas}(r, z)\sigma_{\rm ij}N_j \tag{3.1}$$

where N_i is the density of the species i, $E_k \equiv (E - m_A)/A$ (E is the total energy of a nucleus with mass $m_A \sim Am_{\rm nucleon}$) is the kinetic energy per nucleon, which is constant during propagation, D is the diffusion tensor, $Q_i(E_k, r, z)$ the distribution of CR sources. In the 2nd term of the r.h.s. of Eq. 3.1, which describes fragmentation losses, σ_i is the total inelastic cross section onto the ISM gas with density $n_{\rm gas}(r, z)$. In the 3rd term σ_{ij} is the cross-section for the production of the nuclear species j by the fragmentation of the i-th one. To solve Eq. 3.1 in general is a hard task. For this reason, many simplified models have been adopted. Before describing the most recent numerical models, it is worth referring to one of the most widely known and used analytical models, the so called *leaky-box* model [4]. The leaky-box model assumes that diffusion occurs very fast in the Galaxy, so that the CR density over the whole Galaxy is constant and the CR transport can be described by replacing the diffusion term in Eq. 3.1 with a leakage one, of the form $N_i/\tau_{\rm esc}$, accounting for the escape of CRs out of the Galaxy and all other quantities, like gas density or source distribution, with averaged ones. The resulting transport equation is

$$\frac{\partial N_i}{\partial t} + \frac{N_i}{\tau_{\rm esc}} = \bar{Q}_i(E_k) - c\beta\bar{n}_{\rm gas}\sigma_{\rm in}(E_k)N_i + \sum_{j>i} c\beta\bar{n}_{\rm gas}\sigma_{ij}N_j\,. \tag{3.2}$$

Within this framework, the most important properties of low-energy CRs depend essentially on the average thickness of material crossed by CRs during propagation $x_l = \bar{n}_{\rm gas}v_{\rm esc}$. For example, if we want to calculate the stationary state density of a secondary species (which we label with the subscript 2) assuming it is produced only by spallation of the primary species 1, we have

$$N_2\,(1/\tau_{\rm esc} + c\beta\bar{n}_{\rm gas}\sigma_2(E_k)) = c\beta\bar{n}_{\rm gas}\sigma_{12}N_1\,, \tag{3.3}$$

whose solution for the secondary/primary ratio is

$$\frac{N_2}{N_1} = \frac{\sigma_{12}}{\sigma_2 + 1/x_l}\,. \tag{3.4}$$

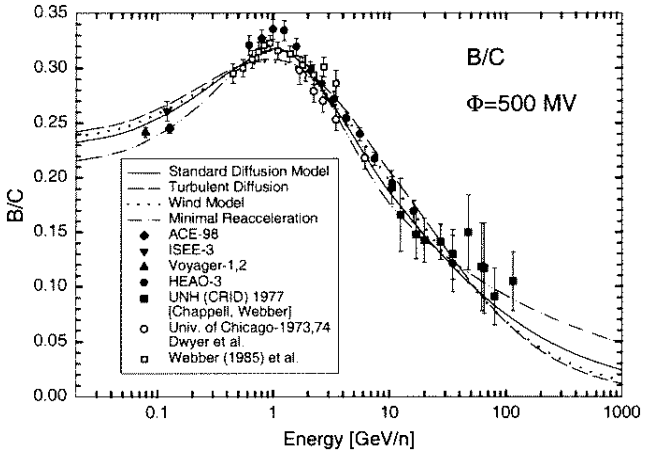

Figure 3.1 Compilation of data of B/C energy spectrum. Courtesy of [153].

By using this kind of relationships and our knowledge of nuclear cross-sections it is possible to infer the properties of x_l as a function of the kinetic energy per nucleon E_k. In Fig. 3.1 the observed B/C ratio is shown. From the energy dependence of B/C ratio it is possible to infer a scaling of the form $x_l \propto E^{-\delta}$ with $\delta \sim 0.6$, even if slightly depending on the details of the model used to fit the data.

Furthermore, it is possible, introducing some simplification in the geometry of the diffusion region, to relate the matter thickness x_l to the mean CR diffusion coefficient D [61]. If the gas is confined in a layer in the galactic disc whose height h_g is much smaller than the galactic halo one h_h, it can be shown that

$$x_l = \frac{n_g v h_g h_h}{D} \,. \tag{3.5}$$

Therefore, secondary/primary ratio measurements also give relevant information on the diffusion properties of galactic CRs, implying $D \propto E^{\delta}$, with $\delta \approx 0.6$, in this simple model.

3.2 The need for a more refined model

More realistic diffusion models are required to provide a comprehensive description of multi-channel observations (including heavy nuclei, electrons, γ-rays and antimatter particles), accounting for the growing amount of available astrophysical data.

The *two-zone* model [168] introduces further details in the diffusion model still

trying to obtain analytical results, while on the numerical side the GALPROP code [169, 170] has been developed extensively. In the case of GALPROP, the adoption of a realistic gas and radiation field distributions allows to model also the spectrum and angular distribution of the γ-ray secondary emission.

Although these models allow a significant step forward with respect to previous analysis, they still perform a number of simplifications with respect to a more realistic physical scenario. In particular, they assume diffusion to be statistically isotropic and homogenous, i.e. they adopt the same single value (or at most two values in the two-zone model) diffusion coefficient all over the propagation volume.

However, such assumptions may not always be justified, as diffusion coefficients generally depend on the regular magnetic field orientation and on the ratio between the regular and the chaotic magnetic field energy densities. Although these quantities are poorly known, several observations and theoretical arguments suggest that they are far from being spatially homogeneous in the Galaxy. This may have relevant consequences for the CR spatial distributions in the Galaxy, for the angular distribution of the secondary γ-ray and neutrino emissions [171] and to interpret the CR anisotropy.

Furthermore, the presence of a regular component of the magnetic field, which is the case in the Milky Way, is expected to break isotropy so that spatial diffusion has to be described in terms of a diffusion tensor $D_{ij}(\mathbf{x})$. According to [172] this can be conveniently decomposed as:

$$D_{ij}(\mathbf{x}) = (D_{\perp}(x) - D_{\parallel}(x))\hat{B}_i\hat{B}_j + D_{\parallel}(x)\delta_{ij} + D_A(x)\epsilon_{ijk}\hat{B}_k\,, \tag{3.6}$$

where $\hat{B}_i$ are the components of the regular magnetic field versor. The symmetric components $D_{\parallel}$ and $D_{\perp}$ are the diffusion coefficients along and perpendicularly to the regular field B_0, while D_A is the antisymmetric (Hall) diffusion coefficient which accounts for the drift due to the interplay of B_0 and CR density gradient. Since D_A is relevant only at very high energies ($E \gg 1$ PeV, see e.g. [171, 173]) we will disregard it in the following. Since diffusion is related to magnetic processes, diffusion coefficients depend on the particle rigidity $\rho = p(E)/Ze$. Moreover, in general $D_{\parallel}$ and $D_{\perp}$ depend differently on ρ and on the strength of hydromagnetic

fluctuations. In the quasi-linear theory (QLT):

$$D_{\parallel}(x,\rho) \sim \frac{1}{3} v r_L(\rho) \mathcal{P}^{-1}(k)\,, \tag{3.7}$$

where $r_L(\rho) = \rho/B_0$ is the Larmor radius and $\mathcal{P}(k) \sim \delta B(k)^2/B_0^2$ is the normalized power spectrum of the turbulent hydromagnetic modes with wavenumber $k \geqslant 2\pi r_L^{-1}(\rho)$. A power-law behavior $\mathcal{P}(k) \propto k^{-\gamma}$ is generally assumed, with $\gamma = 5/3(3/2)$ for Kolmogorov (Kraichnan) turbulence spectrum. In QLT the perpendicular diffusion coefficient is

$$D_{\perp}(x,\rho) \sim D_{\parallel}(x,\rho)\mathrm{P}(k) \ll 1\,, \tag{3.8}$$

meaning that diffusion takes place mainly along the regular magnetic field lines.

Although QLT may not be applicable to the conditions presents in the ISM, more realistic computations [61] confirmed that expectation, finding $D_{\perp} \approx 0.1 D_{\parallel}$. MonteCarlo simulations of particle propagation in turbulent fields [173, 174, 175] also found a similar result (although computation time limits allowed to test it only at energies above 100 TeV). What is most relevant here, however, is the different behavior of $D_{\parallel}$ and $D_{\perp}$ as a function of the turbulent power. Simulations of propagation in strongly turbulent fields agree with QLT predicting $D_{\parallel}$ ($D_{\perp}$) decreasing (increasing) when $\mathcal{P}(k)$ increases. It should be noted that if, as it is generally assumed, the CR source distribution can be approximated to be cylindrically symmetric, and the regular field to be purely azimuthal $B = (0, B_{\phi}, 0)$, parallel diffusion plays no physical role.

Clearly, under this approximation and in absence of an a priori criterion to fix the normalization and energy dependence of the diffusion coefficients, the substitution of an isotropic diffusion coefficient with $D_{\perp}$ would produce no physical effects. This conclusion is no more true, however, if the homogeneous diffusion approximation is relaxed and one tries to correlate spatial variations of the relevant diffusion coefficients to those of the hydro-magnetic fluctuation energy density, as $D_{\parallel}$ and $D_{\perp}$ have an opposite behavior as functions of $\mathcal{P}(k)$.

3.2.1 Spatial behavior of $D_\perp$ in the Milky Way

Very little is known about the spatial distribution of hydro-magnetic fluctuations in the Galaxy. From a theoretical point of view, this quantity is quite unlikely to be uniform, as fluctuations are expected to be correlated, via particle-wave resonant scattering, to CRs, which in turn are correlated to the non-uniform source distribution. Observationally, very little is known. There are, however, evidences both for a longitude [176] and latitude [177, 178] dependence of the fluctuation power.

A radial variation of the diffusion coefficient may have relevant consequences on the CR spatial distribution in the galactic disk. In [171] it was already pointed out that in-homogeneous diffusion may help reconciling the discrepancy between the rather smooth diffuse γ-ray longitude profile observed by EGRET [179] with the quite steep SNR (the most likely CR sources) radial distribution (CR gradient problem). That can be understood as a back-reaction effect: a larger CR density nearby sources induces a larger $\mathcal{P}(k)$, hence a larger $D_\perp$, which in turn implies a faster CR diffusion out of those regions (note that the effect would be opposite for $D_\parallel$). In § 3.7 we will show the possible consequences of this effect on the γ-ray angular distribution.

Concerning the vertical profile of the diffusion coefficient we assume here

$$D(\rho, r, z) = D(\rho) f(r) \exp\left(|z|/z_t\right) , \tag{3.9}$$

with z_t as a characteristic height scale for the diffusion coefficient.

This is motivated by the requirement to get a physically more reasonable behavior of the CR density at large $|z|$. In fact, a vertically growing $D_\perp$ may be justified if the regular component of the galactic magnetic field B_0 decreases more rapidly than the turbulent one, so that $\mathcal{P}(k)$ grows with $|z|$ in spite of the decreasing CR density. Indeed, this seems to correspond to the actual physical situation, as RMs of polarized radio sources point to a vertical height scale for the regular magnetic field as large as ~ 1.5 kpc [180], while dating of unstable CR species (mainly the ^{10}Be) constraints the halo vertical hedge to be in the interval $4 - 6$ kpc [169]. An exponentially growing profile of the diffusion coefficient has been also considered in [181].

We verified that, as far as stable secondary nuclei are concerned, replacing an

exponentially vertically growing $D_\perp$ with a uniform one has almost no effects, as expected because spallation takes place mainly in the thin Galactic disk where the CR density is only marginally affected by the choice between these two options. Observable effects may however be expected in the latitude profile of the γ-ray emission.

3.3 The CR propagation framework in DRAGON

Galactic CRs propagate diffusively in the irregular component of the Galactic magnetic field undergoing nuclear interactions with the gas present in the ISM. Similarly to previous treatments, we assume here that CR Galactic source, magnetic field and gas distributions can be approximated to be cylindrically symmetric. Under these conditions, and in the energy range we are interested in, CR propagation of stable nuclei obeys the well known transport equation [61]:

$$\begin{aligned} \frac{\partial N^i}{\partial t} &- \boldsymbol{\nabla} \cdot (D\,\boldsymbol{\nabla} - \boldsymbol{v}_c)\,N^i + \frac{\partial}{\partial p}\left(\dot{p} - \frac{p}{3}\boldsymbol{\nabla}\cdot\boldsymbol{v}_c\right)N^i - \frac{\partial}{\partial p}p^2 D_{pp}\frac{\partial}{\partial p}\frac{N^i}{p^2} = \\ &= Q^i(p,r,z) + \sum_{j>i} c\beta n_{\rm gas}(r,z)\sigma_{ji}N^j - c\beta n_{\rm gas}\sigma_{\rm in}(E_k)N^i\,. \end{aligned} \tag{3.10}$$

Here the symbols have the same meanings a in Eq. 3.1. In addition, $\boldsymbol{v}_c$ is the convection velocity and the last term on the l.h.s. describes diffusive reacceleration of CR in the turbulent galactic magnetic field. In agreement to the quasi-linear theory we assume the diffusion coefficient in momentum space D_{pp} to be related to the spatial diffusion coefficient by the relationship $D_{pp} = \dfrac{4}{3\delta(4-\delta^2)(4-\delta)} v_A^2\; p^2/D$ where v_A is the Alfvèn velocity. Here we assume that diffusive reacceleration takes place in the entire diffusive halo.

Although DRAGON allows to account also for CR convection, we neglect this effect in the present analysis showing *a posteriori* that it is not necessary to consistently describe all the available data above 1 GeV/n. Hence in the following we will set $v_c = 0$. By this we do not mean that CR data implies that the physical value of v_c is actually vanishing but only that an effective description of their propagation is possible even if convection is disregarded (see the discussion at the end of § 3.6).

DRAGON solves Eq. (3.10) numerically in the stationary limit $\partial N_i/\partial t = 0$ by imposing the following boundary conditions: $N(p, R_{\rm max}, z) = N(p, r, z_{\rm min}) =$

$N(p, r, z_{\rm max}) = 0$, corresponding to free escape of CRs at the outer limit of the Galaxy; a symmetry condition on the axis $r = 0$, $N(p, 0 + \epsilon, z) = N(p, 0 - \epsilon, z)$ ($\epsilon \ll 1$), due to the assumed cylindrically symmetric setup; a null flux condition $\partial N/\partial p = 0$ on the momentum boundaries. The spatial limits of our simulation box are defined by $R_{\rm max} = 20$ kpc and $z_{\rm max} = -z_{\rm min}$. We start the spallation routine from $Z = 16$, having verified that the effect of heavier nuclei on the results of the present analysis is negligible when compared to other uncertainties, being below the 1% level.

We briefly recall below the main assumptions we make for the terms appearing in Eq. (3.10).

3.3.1 Spatial diffusion coefficient

The dependence of D on the particle rigidity ρ and on the distance from the Galactic plane z is taken to be

$$D(\rho, r, z) = D_0 \, \beta^\eta \left(\frac{\rho}{\rho_0} \right)^\delta \quad \exp\left\{ |z|/z_t \right\} \ . \tag{3.11}$$

As discussed in § 3.2.1, a vertically growing D is physically more realistic than a uniform one and allows to get a more regular behavior of the CR density at the vertical boundaries of the propagation halo with respect to the case of uniform diffusion. As far as the statistical analysis discussed below is concerned, however, the substitution of such a profile with a vertically uniform D only requires a change of the normalization factor D_0. Generally, the value $\eta = 1$ is adopted in the related literature. This parameter, however, is not directly constrained by independent observations and other values have been recently considered (see e.g. [182]). We neglect here a possible dependence on the radial coordinate r, which we will consider later in § 3.7. We always set $z_{\rm max} = 2 \times z_t$ in Eq. (3.11) to avoid border effects, and $\rho_0 = 3$ GV in the following. Finally, we assume no break in the power-law dependence of D on rigidity, and we checked that our results do not depend on the choice of $z_{\rm max}$, but only on z_t, which then acts as the effective vertical size of the diffusive halo.

3.3.2 Cosmic ray sources

For the source term we assume the general form

$$Q_i(E_k, r, z) = f_S(r, z)\ q_0^i\ \left(\frac{\rho(E_k)}{\rho_0}\right)^{-\alpha_i}\ , \tag{3.12}$$

and impose the normalization condition $f_S(r_\odot, z_\odot) = 1$. We assume $f_S(r, z)$ to trace the SNR distribution as modeled in [183] on the basis of pulsar and progenitor star surveys [166]. This is slightly different from the radial distributions adopted in [170] and in [168, 184] which are based on pulsar surveys only. Two-zone models assume a step like dependence of $f_S(r, z)$ as function of z, being 1 in the Galactic disk ($|z| < z_d$) and 0 outside. For each value of δ in Eq. (3.11) we fix α_i by requiring that at very high energy ($E_k \gtrsim 100$ GeV/n) the equality $\alpha_i + \delta = \gamma_i$ holds, as expected in a plain diffusion regime. Indeed, at such high energies reacceleration and spallation processes are irrelevant. Here we adopt the same spectral index ($\gamma_i = \gamma$, hence $\alpha_i = \alpha$) for all nuclei as indicated by recent experimental results [185, 186].

The low energy behavior of Q is quite uncertain and several different dependencies of Q on the velocity β have been considered (see e.g. [168]). In the energy range explored in this work, however, different choices of such behavior have negligible effects. This strengthens further the importance of relying on high energy data to reduce systematic uncertainties.

The injection abundances q_0^i are tuned so that the propagated, and modulated, spectra of primary species fit the observed ones. Here we choose to normalize the source spectra of Oxygen and heavier nuclides to reproduce the observed spectra in CRs at $E \sim 100$ GeV/n. On the other hand, Carbon and Nitrogen (which, together with Oxygen mostly affect the B/C) injection abundances (with respect to Oxygen) are free parameters, over which we marginalize our statistical variables in our analysis, in a way which we will describe in § 3.4. Our data basis for Oxygen and heavier nuclei is constituted by ACE/CRIS data [187]. For B, C and N, besides CREAM's, we use experimental data provided by the HEAO-3 [188] and CRN [189] satellite-based experiments. HEAO-3 B/C data are nicely confirmed by a recent preliminary analysis of AMS-01 data [190] which, however, we do not use in this work.

We verified *a posteriori* that the observed Oxygen spectrum (see below), as well

as the subFe/Fe ratios[2], are reasonably reproduced by our best-fit model.

For the primary proton local interstellar spectrum (LIS) we adopt $J_p = 1.6 \times 10^4 \ (E_k/1 \text{ GeV})^{-2.73} \, (\text{m}^2 \text{ s sr GeV})^{-1}$ as measured by BESS during the 1998 flight [191]. This spectrum also provides an excellent fit to AMS-01 [190] data and, as we will show below, also to preliminary PAMELA proton spectrum data.

What is most important here, however, is that we assume no spectral breaks in the source spectrum of all nuclear species. As we will discuss in § 3.6 this point is crucial to understand the difference between our results and those of some previous works.

3.3.3 Nuclear cross sections

The spallation cross sections and the spallation network are based on a compilation of experimental data (when present) and semi-empirical energy dependent interpolation formulas as provided e.g. in [192, 193] (see also GALPROP code website, from which data and some related routines have been obtained and included in DRAGON as an external library).

For antiprotons, the main processes responsible for their production are $p - p_{\text{gas}}$, $p - \text{He}_{\text{gas}}$, $\text{He} - p_{\text{gas}}$ and $\text{He} - \text{He}_{\text{gas}}$ reactions, plus a negligible contribution from other nuclei. Similarly to [164, 165] we adopt the $\bar{p}$ production cross-section calculated using the parametrization given in [194]. Inelastic scattering, annihilation and tertiary $\bar{p}$ (antiprotons which have been inelastically scattered) are treated as in [164].

In order to test the possible dependence of our results on systematical uncertainties on those cross sections, we performed several DRAGON runs using also a different set of nuclear cross sections as determined in [195] (see § 3.6).

3.3.4 Target gas

The ISM gas is composed mainly by molecular, atomic and ionized hydrogen (respectively, H_2, HI and HII). Here we adopt the same distributions as in [169, 166]. We checked that other possible choices do not affect significantly our final results. Following [196] we take the He/H numerical fraction in the ISM to be 0.11. We neglect heavier nuclear species.

[2]To compute these ratios, of course we extended our numerical simulations up to $Z = 28$.

3.3.5 Solar modulation

We describe the effect of solar modulation on CR spectra by exploiting the widely used force-free approximation [197], prescribing that the modulated spectrum $J(E_k, Z, A)$ of a CR species is given, with respect to the Local Interstellar Spectrum (LIS) $J_{\rm LIS}(E_k, Z, A)$, by

$$J(E_k, Z, A) = \frac{(E_k + m)^2 - m^2}{\left(E_k + m + \frac{Z|e|}{A}\Phi\right)^2 - m^2} \; J_{\rm LIS}(E_k + \frac{Z|e|}{A}\Phi, Z, A) \; , \qquad (3.13)$$

where m is the nucleon mass and Φ is the so called modulation potential. This potential is known to change with the solar activity with a period of 11 years. It must be stressed that the potential Φ is not a model independent quantity. Rather, for each propagation model it should be obtained by fitting the CR spectra at low energy. The possibility of restricting our analysis to $E_k > 1$ GeV/n will reduce the systematic uncertainties associated to this unknown. Above 1 GeV/n the effects of modulation on the secondary/primary CR ratios used in our analysis are tiny and can safely be accounted for by means of the simple force free approximation.

For protons and antiprotons we use a potential which allows to match BESS98 [191], AMS-01[190] and PAMELA proton data even well below 1 GeV/n (see Fig. 3.7). Indeed all these experiments took their data in a period with almost the same, almost minimal, solar activity. Although a more complicated and realistic treatment of solar modulation, accounting for charge dependent effects, and the 22 year cycle change of polarity associated to solar effects, might be needed when dealing with $\bar{p}/p$ ratios (see e.g. [198]), we decide to work in the framework of the force-free field approximation, because the effects of solar modulation are less relevant above 1 GeV, hence we do not make a large error in estimating our confidence regions of propagation parameters in the framework of the force-field approximation.

3.4 Analysis and results

Our goal is to constrain the main propagation parameters δ, D_0, z_t and v_A entering in Eq. (3.11). To this aim, we compare to experimental data our prediction for the following physical quantities: the B/C, N/O, C/O ratios for $1 < E_k < 10^3$ GeV/n and the $\bar{p}/p$ ratio for $1 < E_k < 10^2$ GeV/n. We will check *a posteriori* that also

the Oxygen, proton and antiproton absolute spectra are correctly reproduced by our preferred models. In order to test the relevance of low energy physics on our constraints of the diffusion-reacceleration parameters, we perform our analysis for three different values of the minimal energy $E_{\rm min}$. We will then motivate the choice of the most suitable value of $E_{\rm min}$.

As long as the propagation halo scale height is allowed to vary within the range $2 \lesssim z_t \lesssim 6$ kpc (which is what we assume here), D_0 and z_t are practically degenerate so that our results depend only on the ratio D_0/z_t. Throughout this chapter we will always express this quantity in units of 10^{28} cm^2 s^{-1} kpc^{-1}. We verified *a posteriori* that for this range of z_t values, the predicted ^{10}Be/^{9}Be ratio, which constrains the CR propagation time hence the vertical scale height of the propagation region [61] when combined with secondary/primary stable nuclei data, is consistent with experimental data.

3.4.1 Light nuclei ratios

Method

It is a known result [166] that in order to constrain correctly the propagation parameters on the basis of B/C measurements it is essential to take into proper account that the main primary parent species of Boron[3] are also affected by propagation. This holds not only for the Nitrogen (N = ^{14}N + ^{15}N), which gets a significant secondary contribution, but also for Carbon and Oxygen, since for $E_k < 100$ GeV/n their spectra are shaped by spallation losses in a propagation dependent way. Therefore, we perform our likelihood analysis in three steps:

1. for fixed values of the propagation parameters v_A, δ, and D_0/z_t we vary the C/O and N/O source ratios to compute the χ^2([4]) (which we call $\chi^2_{\rm C,N,O}$) of the propagated, and modulated, C/O and N/O ratios against experimental data in the energy range $1 < E_k < 10^3$ GeV/n;

2. for the same fixed value of v_A, we finely sample the parameter space (δ, D_0/z_t) by using, for each couple of these parameters, the C/O and N/O source ratios

[3] A non negligible contribution to the ^{10}B comes from the beta decay of ^{10}Be, which is properly accounted for in our analysis.

[4] Every time we refer to a χ^2, we mean the χ^2 divided by the number of degrees of freedom, i.e. the so called reduced χ^2.

which minimize $\chi^2_{\rm C,N,O}$; for each of these realizations we compute the χ^2 (which we call $\chi^2_{\rm B/C}$) for the B/C modulated ratio against data with $E > E_{\rm min}$;

3. we repeat the same analysis for several values of v_A to probe the effect of diffusive reacceleration. For each value of v_A we then determine the allowed ranges of δ and D_0/z_t for several Confidence Levels (CL).

The wide energy range covered by these recent data allows us to perform our analysis using three different energy intervals defined by $E_{\rm min} = 1$, 5 and 10 GeV/n respectively and by the same $E_{\rm max} = 1$ TeV/n.

As we already stated in the above, we do not account in our analysis for light nuclei and antiproton data with energy below 1 GeV/n as they are affected by poorly known low energy physics and are not necessary to constrain the high energy behavior of the diffusion coefficient, which is the main goal of this work. In § 3.5 we will show, however, that specific models which fit all data even below that energy can be built, adopting diffusion coefficients allowed from our analysis.

Results of the analysis

In Tab. 3.1 we report the best-fit model parameters, and the relative minimal $\chi^2_{\rm B/C}$'s, as determined for several values of v_A and $E_{\rm min}$.

First of all we notice that in the highest energy range ($E_{\rm min} = 10$ GeV/n) the best-fit model values of δ and D_0/z_t are weakly dependent on the Alfvèn velocity. In particular, the best fit values of δ stays in the very narrow range $0.40 \div 0.46$ varying v_A from 0 to 30 km/ s. This agrees with the common wisdom that reacceleration is almost ineffective at such high energies (see also Fig. 3.4.3).

The most useful results, however, are those obtained for $E_{\rm min} = 5$ GeV/n since that threshold provides the best compromise between the two opposite requirements: 1) to include in the analysis more experimental data and 2) to work in an energy range where propagation is as less as possible affected by poorly known low energy physics. For example, possible charge dependent drift effects in the solar modulation (see e.g. [198, 164]) can be safely neglected in that energy range. Best fit parameters and confidence level contours obtained for that value of $E_{\rm min}$ are showed in Tab. 3.1 and in Fig. 3.2 respectively.

From both we notice that all considered values of v_A are almost equally permit-

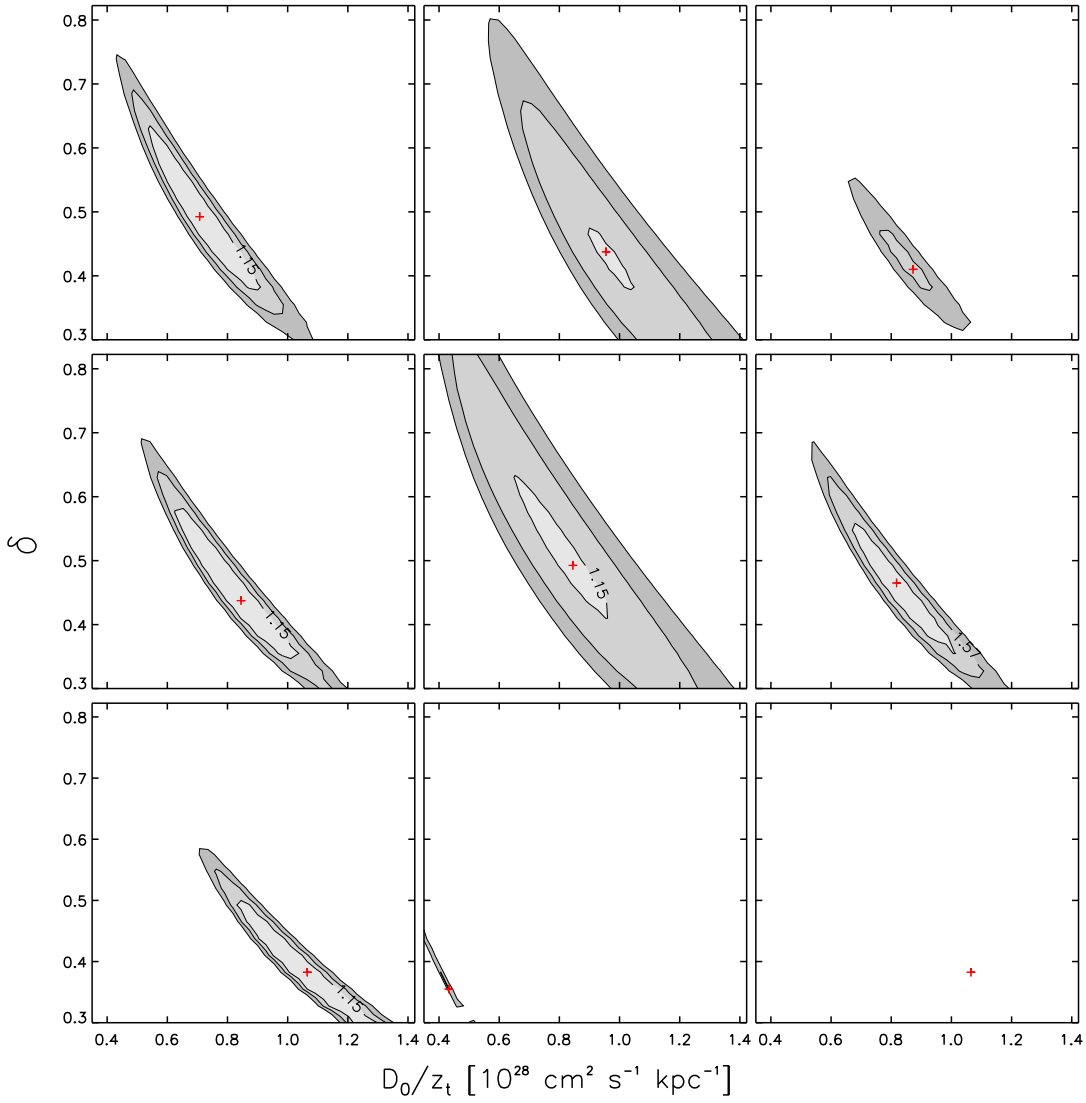

Figure 3.2 The 68%, 95% and 99% confidence level regions of DRAGON models, computed for $E_{\rm min} = 5$ GeV/n are represented in the plane $(D_0/z_t, \delta)$. For the 68% confidence level the corresponding value of the χ^2 is also shown. The red crosses show the best-fit position. Each row corresponds to different values of the Alfvèn velocity: $v_A = 10, 20, 30$ km/ s from top to bottom. Each column corresponds to different analyses: B/C (left panels), $\bar{p}/p$ (center panels) and combined (right panels).

Table 3.1 Best fit parameters, and the corresponding χ^2 values resulting from comparing our model predictions with nuclear experimental data alone (B/C analysis) and with nuclear and $\bar{p}/p$ combined data (combined statistical analysis), as described in text. The values corresponding to $E_{\rm min} = 5$ GeV/n for the combined analysis, which are used to constraint our models, are reported in bold.

		B/C analysis			joint analysis		
v_A [km/s]	$E_{\rm min}$ [GeV/n]	δ	D_0/z_t	χ^2	δ	D_0/z_t	χ^2
0	1	0.57	0.60	0.38	0.47	0.74	3.25
	5	0.52	0.65	0.33	**0.41**	**0.85**	**2.04**
	10	0.46	0.76	0.19	0.44	0.82	1.57
10	1	0.52	0.68	0.32	0.49	0.71	1.47
	5	0.49	0.71	0.28	**0.41**	**0.85**	**1.69**
	10	0.44	0.82	0.20	0.44	0.82	0.12
15	1	0.46	0.76	0.33	0.47	0.76	0.94
	5	0.49	0.73	0.26	**0.44**	**0.82**	**0.12**
	10	0.44	0.84	0.18	0.41	0.98	0.16
20	1	0.41	0.90	0.47	0.47	0.79	2.28
	5	0.44	0.84	0.22	**0.44**	**0.84**	**0.85**
	10	0.44	0.87	0.20	0.44	0.85	0.98
30	1	0.33	1.20	0.40	0.33	1.20	5.84
	5	0.38	1.06	0.20	**0.36**	**1.09**	**2.47**
	10	0.41	0.98	0.16	0.38	1.04	1.61

ted by the B/C χ^2 analysis, and that the $\delta - D_0/z_t$ allowed region slightly moves towards low δ's and large D_0/z_t's as v_A is increased from 0 to 30 km/s. While Kraichnan diffusion is clearly favored in the case of low values of v_A, Kolmogorov becomes favored, for $v_A \gtrsim 30$ km/s. The choice among those model, however, is difficult in the absence of an independent estimate of v_A. We will show that the antiproton/proton data break such degeneracy.

In Fig. 3.4.3 we show the effect on the B/C ratio of varying v_A keeping δ and D_0/z_t fixed to the value $(0.45, 0.8)$ which will be motivated below.

3.4.2 Antiprotons

The statistical analysis for the $\bar{p}/p$ ratio is rather simpler than the one for B/C. Indeed, the secondary $\bar{p}$ production depends, besides on D_0/z_t, δ and v_A, only on the source abundance ratio He/p. This last unknown quantity can be easily fixed by looking at the measured spectrum of He at Earth, which is relatively well known. Therefore, we do not need to fit the source abundance ratio here and can directly proceed to map the $\chi^2_{\bar{p}/p}$ in the $(D_0/z_t,\ \delta)$ space, for several v_A, similarly to what described in items (ii) and (iii) of the previous subsection.

In the second column of Fig. 3.2 we show the statistically allowed regions in the plane $(D_0/z_t, \delta)$ for several values of v_A and compare them with the corresponding regions determined from the light nuclei analysis (first column in the same figure). The allowed CL region is significantly larger than that determined from the light nuclei analysis (due to the larger experimental errors) and they overlap only for some values of the Alfvèn velocity. In fact, it is remarkable that the v_A varying behavior of those regions is almost opposite so that not all values of v_A are allowed by a combined analysis (see § 3.4.3).

3.4.3 Combined analysis

A combined analysis of light secondary/primary nuclei and antiproton/proton data can be performed under the working hypothesis that CR antiprotons are only of secondary origin.

We define the combined reduced χ^2 as $\chi^2_{\rm comb} = \frac{1}{2}\left(\chi^2_{\rm BC} + \chi^2_{\rm ap/p}\right)$. The CL regions for several values of v_A are reported in the third column of Fig. 3.2 and the corresponding best-fit parameters in Tab. 3.1. Again, here we use only data with $E > E_{\rm min} = 5$ GeV/n.

As we anticipated in the previous subsection, in general the CL region allowed by the combined analysis is smaller than the B/C one.

Indeed, while the parameter regions constrained by the B/C and $\bar{p}/p$ data nicely overlap for $10 \lesssim v_A \lesssim 20$ km s^{-1}, models outside this range do not allow a combined fit of both data sets at the required level of statistical significance (higher than 95%). The fact that only a limited range of the Alfvèn velocity values are allowed is consequence of the different behavior of the B/C and $\bar{p}/p$ ratios with v_A due to the different spectral shapes of these ratios. This is a new and quite interesting results.

It is reassuring to notice that the results of the analysis performed for $E_{\rm min} = 5$ and 10 GeV/n are practically coincident, which makes us confident that the combined analysis performed for $E_{\rm min} = 5$ GeV/n probes already the purely diffusive CR regime. It is also remarkable that the best fit values of δ and D_0/z_t stay almost unchanged when varying v_A. In particular $(\delta, D_0/z_t) \simeq (0.4 - 0.45, 0.8)$ for all allowed values of $v_A = 10 - 20$ km s^{-1} of the Alfvèn velocity. This makes us confident that the combined analysis performed for $E_{\rm min} = 5$ GeV/n best probes the diffusion-reacceleration parameters .

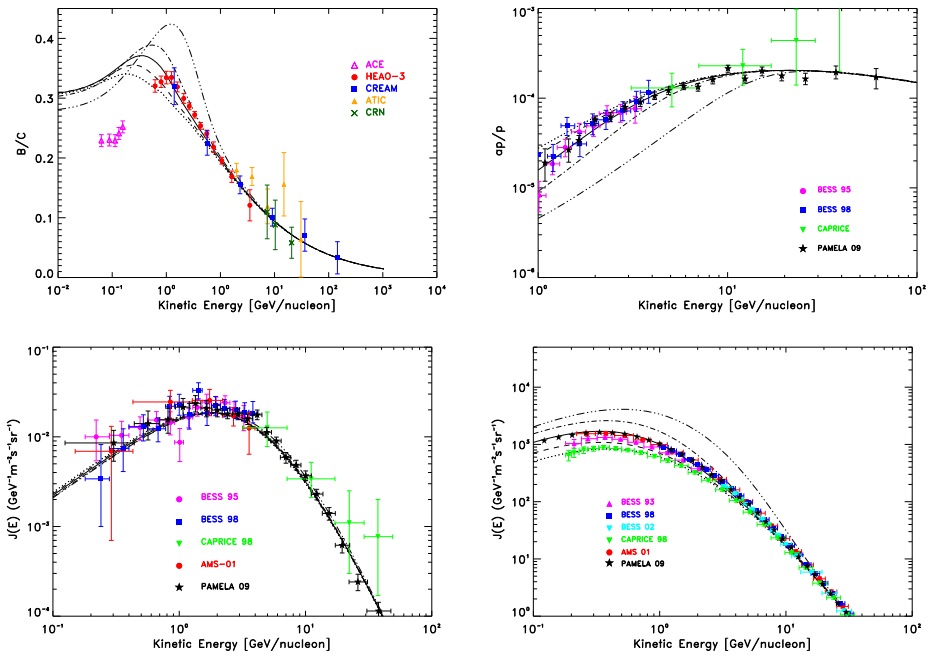

Figure 3.3 The B/C (panel a), and the $\bar{p}/p$ (panel b) ratios, as well the antiproton (panel c) and proton (panel d) absolute spectra computed with DRAGON for $\delta = 0.45$ and $D_0/z_t = 0.8$ are plotted for several values of v_A and compared with the respective experimental data. Dotted, short-dashed, solid, dot-dashed, long-dashed correspond to $v_A = 0, 10, 15, 20, 30$ km/ s respectively. Here $\eta = 1$ which clearly does allow to match nuclear data below 1 GeV/n. For this reason the modulation potentials $\Phi = 500$ MV adopted here for the B/C plot (as required to reproduce low energy Oxygen data) and $\Phi = 700$ MV for the $\bar{p}/p$ (to fit proton data) are not representative.

Among those considered $v_A = 15$ km s^{-1} is the Alfvèn velocity value which minimizes the χ^2 of the combined analysis, hence it gives rise to the best overlap between the light nuclei and the $\bar{p}/p$ confidence regions. This is also visible from Fig.s 3.4.3 and 3.4.3 where the B/C and the $\bar{p}/p$ ratios computed with $(\delta, D_0/z_t) \simeq (0.45, 0.7)$ are plotted for several v_A's. It is also interesting to notice that the dependence of the $\bar{p}/p$ ratio on v_A is driven by that of the proton spectrum since the absolute $\bar{p}$ spectrum is practically unaffected by re-acceleration (see Fig. 3.4.3). We stress that Fig.s 3.4.3, 3.4.3 are given here mainly for illustrative reasons since, below few GeV/n some other physics needs clearly to be introduced to reproduce the B/C data (see § 3.5).

Since the $v_A = 15$ km s^{-1} combined analysis CL region is the largest, it also provides the most conservative constraints on δ and D_0/z_t. They are $0.3 \lesssim \delta \lesssim 0.6$ and $0.6 \lesssim D_0/z_t \lesssim 1$ at 95% CL.

It should be kept in mind that our analysis accounts only for statistical experi-

mental errors. Several systematic uncertainties, however, may affect our constraints too. Among them, systematic errors in the experimental data, uncertainties in the Galactic gas density and hydrogen fraction distributions and nuclear fragmentation cross sections play a major role. A detailed discussion of the possible impact of these uncertainties on the determination of the CR propagation parameters is beyond the aims of this work. A thorough analysis was recently performed in [182] showing that, if low energy data are accounted for (which requires to introduce several unknown parameters with respect to those considered in this work) the systematic uncertainties on the D_0, δ and v_A can be comparable, or even larger, than the statistical ones. However, the former uncertainties are significantly smaller if one considers only a subclass of models without convection and keeping fixed other parameters which only matters a low energies, as we do in this work. For example, it was shown in [182] that for models with $v_c = 0$ the effect of considering different cross-section sets amounts to a $\sim 40\,\%$ uncertainty variation of δ which reduces to $\sim 10\,\%$ if one considers only the most updated cross section sets.

We verified with DRAGON that changing the GALPROP nuclear fragmentation cross sections with those given in [195] produces only a marginal effect on the B/C ratio. The relative effect of cross section uncertainties on the antipron/proton ratio is negligible here due to the high statistical errors on those data.

3.4.4 Maximal and minimal antiproton spectra

The previous results clearly favor a standard interpretation of the measured antiproton spectrum in terms of purely secondary production from CR nuclei. It is still possible, however, that a subdominant antiproton component arises from unconventional processes. In order to constrain such *exotic* component(s) with experimental data, one has to compare antiproton data with the predictions of the theoretical models validated against CR nuclei data alone.

For this purpose we define, for each value of v_A considered in the above, a pair of MAX and MIN models which maximize and minimize respectively the antiproton absolute flux integrated in the range $1 - 100$ GeV under the condition to be compatible with secondary/primary light nuclei data down to 1 GeV/n within 95% CL.

In Fig. 3.4 we show the allowed ranges of the antiproton absolute spectrum for

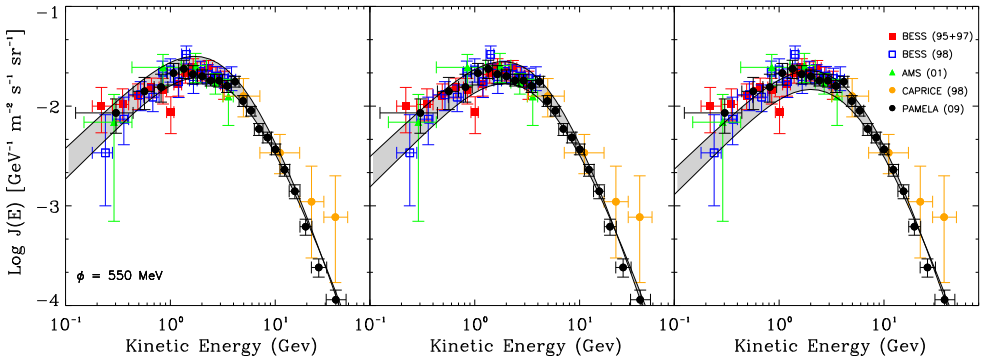

Figure 3.4 The $\bar{p}$ absolute spectrum is shown for $v_A = 10, 20, 30$ (from the left to the right panels respectively). The upper and lower curves correspond to the MAX and MIN models defined as in Sec. 3.4.4 respectively.

several values of v_A. Among the models considered here the absolute MAX and MIN models are those defined by the parameters $(\delta, D_0/z_t, v_A) = (0.68, 0.46, 0)$ and $(0.30, 1.2, 30)$ respectively. Therefore, we conclude that, under the hypotheses adopted in this work, $\bar{p}$ constraints on an exotic component should not use, as propagation models, any model whose $\bar{p}$ background prediction is lower than our MIN (or larger than our MAX) model, as it would be in contrast with B/C data at 95% CL. Hence, the most conservative constraint, under our hypotheses, arises from the request that the sum of the background $\bar{p}$ predicted by the MIN model plus the exotic $\bar{p}$ component do not exceed the experimental data, within some CL.

3.5 A comprehensive model describing all data

The aim of this section is to test the consistency of our previous results with CR data below few GeV/n and to identify an effective model allowing to fit all available data.

It is evident from Fig. 3.4.3 that while the best fit model obtained for $\eta = 1$ provides an excellent fit of experimental data above few GeV/n, below that energy it overshoots the B/C observations. As we discussed, such a discrepancy may be attributable to a number of effects which, at low energies, introduce degeneracies among the relevant parameters. For this reason, a statistical analysis aimed to fit those low energy parameters against presently available data would be hardly interpretable (see e.g. [182]) and it is beyond the aims of this work.

Here we follow a more phenomenological approach tuning only the parameter η (see Eq. 3.11) which sets the dependence of the diffusion coefficient on the particle velocity (a similar approach was followed in [182]). Interestingly we find that the choice $\eta \simeq -0.4$ allows to match light nuclei as well as antiproton data well below 1 GeV/n for almost the same range of δ and D_0/z_t values found for $\eta = 1$. Indeed, we checked that the $\eta = -0.4$ and $\eta = 1$ CL regions computed for $E_{\rm min} = 5$ GeV/n almost coincide (which is not the case for $E_{\rm min} = 1$ GeV/n. In Fig.s 3.6 and 3.6 we show as our best fit model obtained for $\eta = -0.4$, $\delta = 0.5$, $D_0/z_t = 0.7$, and $v_A = 15$ km/s^{-1} nicely reproduces all relevant data sets. They include also the N/O and C/O ratios (with ~ 6 % and ~ 75 % injection ratios respectively) as well as the absolute oxygen spectrum.

We notice that such a behavior of the diffusion coefficient is expected to arise as a consequence of the dissipation of magneto-hydrodynamics (MHD) waves by their resonant interaction with CRs [199]. Since this is the same interaction responsible for CR diffusion in the ISM, such an effect is unavoidable at some level. Interestingly, the value of δ used in [199] to fit the B/C in the presence of MHD wave dissipation is 0.5, which is consistent with what we found here (differently from what we do here, however, a break in the injection index was invoked in that work).

3.6 Comparison with previous results

As we mentioned above, our numerical diffusion code DRAGON reproduces the same results of GALPROP under the same physical conditions. Our analysis and main conclusions, however, differ significantly from those reported in several papers based on that code.

In order to clarify the reasons of such a discrepancy, in Fig. 3.6 and 3.6 we compare the predictions of our reference diffusion-reacceleration model $(\delta, D_0/z_t, v_A, \eta) = (0.5, 0.7, 15, -0.4)$, which for brevity we call *Kraichnan model*, with those obtained using the propagation parameters (and source distribution) of the *Kolmogorov model* discussed in [170], namely $(\delta, D_0(4\ {\rm GV})/z_t, v_A, \eta) = (0.33, 1.45, 30, 1)$ [5]. For the latter combination of parameters we consider two variants, represented by the solid/dashed

[5] In [170] a spatially uniform diffusion coefficient ($z_t = z_{\rm max} = 4$ kpc) was assumed. As we already noticed, for the purposes of the present analysis adopting a vertically uniform rather than varying diffusion coefficient only amounts to a rescaling of D_0/z_t. We verified that this does not affect any other result of our analysis.

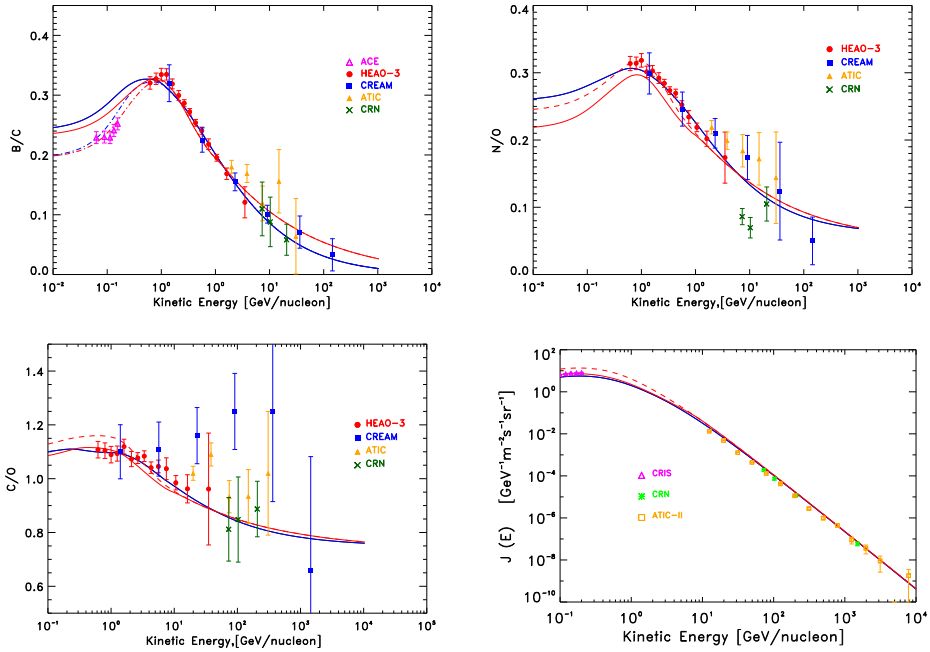

Figure 3.5 The B/C (panel a), N/O (panel b), C/O (panel c) and the oxygen absolute (panel d) spectra computed with our preferred *Kraichnan* model (blue solid line), the *Kolmogorov* reference model (red solid line) and the same model with no break in the CR source spectrum (red dashed line), are compared with available experimental data. In both cases we use DRAGON to model CR propagation and interactions (though almost identical results can be found with GALPROP). Here we use $\Phi = 450$ MV to modulate both the *Kolmogorov model* and our *Kraichnan* reference models. $\Phi = 300$ MV was used only to match B/C ACE data which were taken in a very low activity solar phase.

red lines, which differ for the presence/absence of a break at $\rho_{\rm break} = 9$ GV in the CR nuclei source spectra. The *Kolmogorov model* considered in [170] adopts such a break. It is evident from Fig. 3.7 as this is needed in order to reproduce the low energy tail of the observed proton spectrum which otherwise could not be fit for any choice of the modulation potential. It is important to notice, that this problem arises in all models with strong reacceleration $v_A > 20$ km s^{-1}. On the other hand our Kraichnan reference model requires a *modified* behavior of the diffusion coefficient at low energy ($\eta = -0.4$ rather than $\eta = 1$) which, however, may be motivated by independent physical arguments as discussed in § 3.5.

From Fig.s 3.6 the reader can see that while both the Kraichnan and Kolmogorov models reproduce the B/C equally well, the former model provides a significantly better description of the N/O ratio measured by HEAO-3 [188] and CREAM [155] (see Fig. 3.6). Furthermore, what mostly favors our Kraichnan reference model are BESS [191], CAPRICE [200] and especially the PAMELA measurements of the

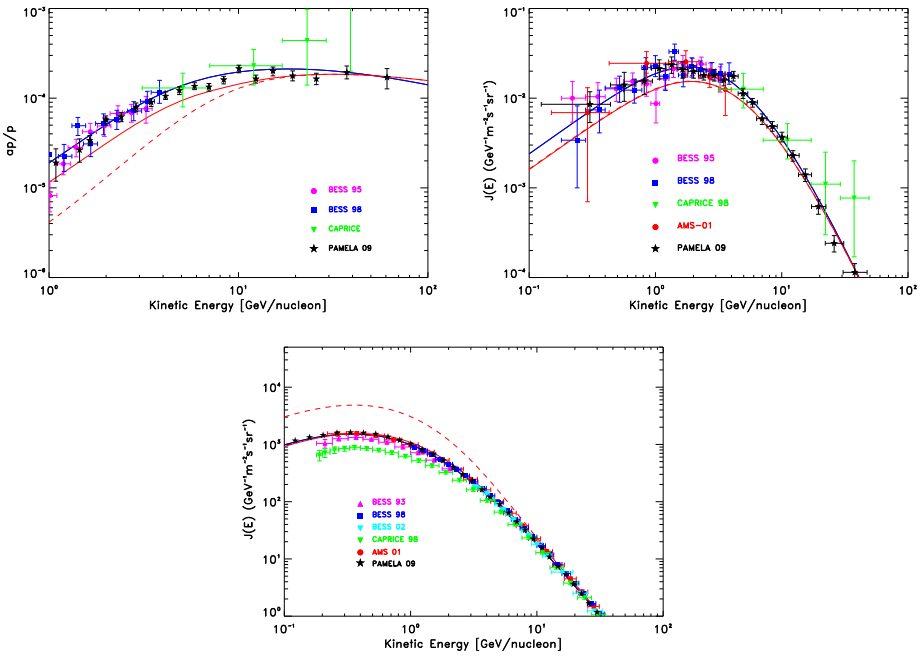

Figure 3.6 The $\bar{p}/p$ (panel a), $\bar{p}$ (panel b) and proton (panel c) computed with DRAGON are reported here use the same models and line notation used in Fig.s 3.6. The solar modulation potential used here is $\Phi = 550$ MV.

$\bar{p}/p$ [156] and antiproton absolute spectrum[6]. Indeed, the discrepancy between low energy antiproton data and the prediction of the *conventional* GALPROP model, which was already noted in [170], becomes more compelling due to the new PAMELA data, as shown in Fig. 3.6.

The comparison of our results with those of semi-analytical models is more difficult for obvious reasons. One of the difficulties lies in the simplified gas and source distribution adopted in those models (see Sec. 3.3). We verified, however, that such differences only affect the constraints to D_0/z_t with almost no effect on the determination of δ. We also need to take into account that semi-analytical models (see e.g. [168, 184]) assume diffusive reacceleration to take place only in the thin Galactic disk (whose height is z_d), while in the numerical models, as the one presented here, it takes place in the entire diffusion halo. Therefore, in order to compare the values of the Alfvèn velocity in those papers with those reported in the above it is necessary to perform a proper rescaling. This is approximatively given by (see e.g. Eq. (18) in [201]) $v_A = v_A^{\rm SA} \sqrt{z_d/z_t}$, with $v_A^{\rm SA}$ being the Alfvèn velocity in the semi-analytical

[6]We extracted this data from the slides of the talk of P. Picozza at the TeVPA 2009 conference, under permission of the author, `http://www-conf.slac.stanford.edu/tevpa09/Talks.asp`

models and z_t the half scale height of the Galactic disk.

In spite of these differences, and that CREAM and PAMELA data were not included in those analyses for chronological reasons, it is comforting that for low values of the convective velocity $v_c \simeq 0$ the preferred value of δ estimated in [168, 184] is in remarkably good agreement with that found in this work: $\delta \simeq 0.45$. Interestingly, the rescaled value of v_A determined in [168] is $v_A \simeq 10$, for $v_c \simeq 0$, which is also in good agreement with our results. It is important to notice that, similarly to what we did in our analysis, no break in the source spectral index was assumed in [168, 184].

We remind the reader that in the above we always assumed $v_c = 0$ as higher values of that parameter are not required to interpret CR nuclei and antiproton data. Models with a finite v_c, which may also allow to fit low energy data though with a different combination of low energy physics parameters (v_A, η, the modulation potential Φ, or any other), will be considered elsewhere. We already tested, however, that taking v_c in a reasonable range of values do not affect significantly our constraints on the diffusion coefficient parameters.

3.7 The γ-ray longitude distribution

In this section we want to use our preferred model for CRs propagation to test the effects of a possible radial dependence of the diffusion coefficient. As we already mentioned, this modification slightly changes local observables (e.g. B/C), so to this aim we model the secondary γ-ray emission originated, via π_0 decay, by the interaction of the hadronic component of CRs with the IS gas. Along the galactic plane (GP), where the gas column density is higher, this process is expected to give the dominant contribution to the total diffuse emission above the GeV. At the energies of our interest a simple scaling model for the differential production cross section can still reliably be used. In this regime the energy spectrum of secondary γ's is a power law with the same slope as the primary nuclei (only protons and He nuclei give a significant contribution). The main gas (target) components are the molecular (H_2) and atomic (HI) hydrogen, and He atoms. The contribution of ionized hydrogen is almost irrelevant in the GP. For $r > 2$ kpc, we adopt the same

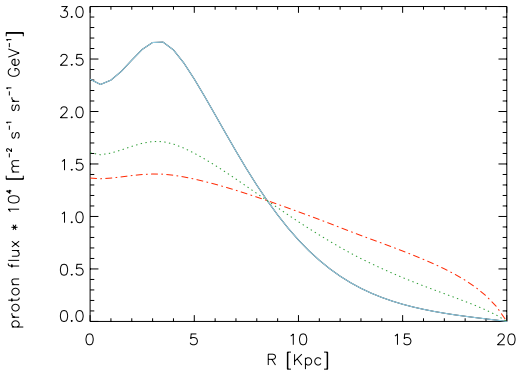

Figure 3.7 Proton differential flux at $E = 1$ GeV for three different choices of the parameter τ setting the radial dependence of the diffusion coefficient on the SNR distribution. $\tau = 0$ (radially uniform D): blue, continuous curve; $\tau = 0.5$: green, dotted; $\tau = 0.75$: red, dot-dashed. In all cases $z_t = 4$ kpc and the D normalization giving the best fit to B/C data is chosen.

HI spatial distribution as [170]. For the H_2 we assume

$$n_{H_2}(r, z) = \epsilon_0(r) X_{\rm CO}(r) \exp\{-\ln 2(z - z_0)^2 / z_h(r)\} \tag{3.14}$$

where $\epsilon(r)$ is the CO (a widely used H_2 tracer) volume emissivity, $z_0(r)$ and $z_h(r)$ are the midplane displacement and scale heights respectively, and $X_{\rm CO}(r)$ is the CO-H_2 conversion factor. All these quantities, with the exception of $X_{\rm CO}(r)$, are the same as in [202, 170] for $r > 2$ kpc, while for smaller radii we adopt the model in [203]. The adoption of Ferriere's model for the molecular and atomic hydrogen for $r < 2$ kpc allows us to avoid the interpolation of the γ-ray flux profile in the GC region and to reproduce naturally the peaked emission observed by EGRET toward the GC as already pointed out in [204]. For the 11% He fraction we adopt the same spatial distribution as for the HI.

3.7.1 The CR gradient problem

The main issue we want to address here is the so called CR *g*radient problem. This originates from the well known discrepancy between the theoretical flux profile obtained by assuming SNRs to be the sources of galactic CRs and that inferred from EGRET γ-ray diffuse observations [179]. Under mild assumptions on the distribution of the galactic gas, it was found [169] that the inferred CR radial profile should be much flatter than the theoretically expected one.

A possible way out was suggested in [170] in terms of a radially variable $X_{\rm CO}$.

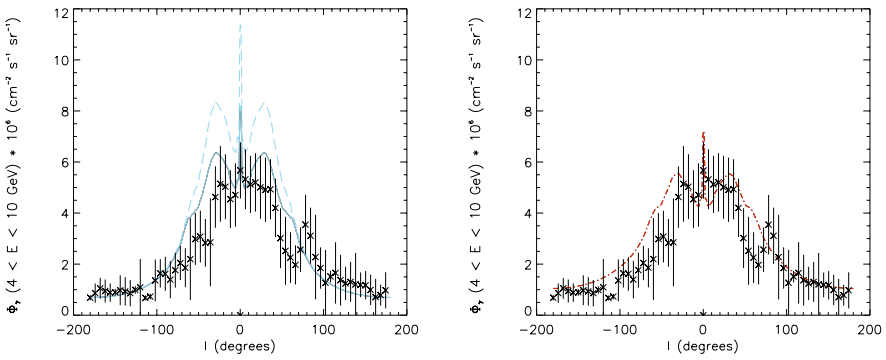

(a) (b)

Figure 3.8 Our predictions for the longitudinal profiles of the γ-ray hadronic emission integrated for $|b| < 1^\circ$ are compared with EGRET measurements. Left panel: radially uniform D with $X_{CO} = 1.8 \times 10^{20}$ cm$^{?2}$/(K km/s) for $r > 2$ kpc (long dashed curve), and X_{CO} as in [170] for $r > 2$ kpc (continuous curve). Right panel: $D(r)$ tracing the SNR distribution with $\tau = 0.75$. In both cases $z_t = 4$ kpc and D normalization is chosen to best-fit the B/C data.

While in [169, 170] this quantity was assumed to be uniform ($X_{CO} = 1.8 \times 10^{20}$ cm$^{?2}$/(K km/s)), in [170] it was taken to increase gradually by more than one order of magnitude from 4×10^{19} at $r = 2$ kpc to 1×10^{21} at $r > 10$ kpc. However, while the growth of this parameter with r is suggested by both theoretical arguments and observations of external galaxies, its actual behavior is rather uncertain so that in [170] it had to be tuned into 5 steps to match EGRET observations.

To test our code against possible failures in reproducing the γ-ray longitude profile, we try to reproduce the results of [170]. We adopt the same $X_{CO}(r)$ which was used in [170] and a CR model giving the best-fit of the B/C in the case of a radially uniform diffusion coefficient. We use $\delta = 0.57$ (see § 3.4.1) but our results do not change appreciably by using any value in the interval $0.45 \div 0.65$. In Fig. 3.8 we compare our results with EGRET measurements along the GP for $4 < E_\gamma < 10$ GeV [179]. We reasonably reproduce both the normalization and the main features of the observed longitude profile. For comparison, in the same figure we also show the emission profile which we would obtain using a constant $X_{CO}(r) = 1.8 \times 10^{20}$ for $r > 2$ kpc.

As an alternative possibility we explore the case in which the diffusion coefficient traces the radial dependence of the SNR distribution as we motivated in § 3.2.1. According to the arguments explained in the same section we expect the CR radial profile to be smoothed with respect to the one obtained in the case of constant

diffusion coefficient. Hence, we expect to be able to fit EGRET longitude profile without fine tuning the parameter X_{CO}. Indeed, this is what we find. We assume a constant $X_{CO} = 1.8 \times 10^{20}$ for $r > 2$ kpc, while in the bulge ($r < 2$ kpc), where physical conditions are much different from the outer disk, we take $X_{CO} = 0.5 \times 10^{20}$ [200]. For the diffusion coefficient, we assume that the function $f(r)$, as defined in Eq. 3.9, is

$$f(r) = f_S(r, 0)^\tau \, . \tag{3.15}$$

The function $f_S(r, 0)$ describing the radial distribution of the Galactic SNRs is taken by [183] and is the same as in [171]. The exponent τ is practically unknown, hence it will be fixed by the requirement to reproduce observations. We verified that, as long as $\tau < 1$, we are still able to obtain a good fit of the B/C and antiproton data with nearly the same parameter values as in section § 3.4.1. In particular, we find that for $\tau = 0.75$ the best-fit value for D_0/z_t is 0.52 while δ, the C/O and N/O injection abundances are unchanged with respect to the radially uniform diffusion case discussed in the previous sections. It is worth noticing, however, that the CR spatial distributions corresponding to these models are considerably different. In Fig. 3.7 we show the radial profile of the proton differential flux at 1 GeV for three different values of the parameter τ: 0.75, 0.5 and 0 (the latter corresponds to a radially uniform D). It is remarkable that the smoothing effect of relating D to the SNR distribution can be quite significant without spoiling the successful predictions for the charged secondary CR at Earth. Interesting observable effects, however, are expected for what concerns the diffuse γ-ray emission. In Fig. 3.8(b) we show the simulated γ-ray longitude profiles as obtained using $\tau = 0.75$ (smaller values of τ produce a less pronounced flattening). It is clear that our model is able to reproduce EGRET observation without invoking a fine tuning of the X_{CO}[7]

It is worth noticing that there is a potential degeneracy between the radial dependence of X_{CO} and that of the diffusion coefficient, as evident comparing Fig.s 3.8(a) and 3.8(b). This should be taken into account when interpreting observations of γ-ray diffusion emission of the Galaxy.

[7] Although we achieved this result by phenomenologically introducing the free parameter τ, it should be noticed that, differently from the $X_{CO}(r)$, τ is the only single value parameter which does need to be tuned in this model.

3.8 Conclusions

We used recent data on CR light nuclei and antiprotons to determine the conditions of propagation of high energy CRs in the Galaxy, exploiting our numerical code, DRAGON. In the framework of a diffusion-reacceleration model, we performed a thorough analysis of the agreement of our predictions with experimental information, aimed at constraining, in a statistical sense, the most important model parameters: D_0/z_t, δ and v_A. The amount and quality of data is enough to allow us to perform our analysis in a wide energy range, from 1 to 10^3 GeV/n, and also to check the evolution of our results varying the minimal energy at which data are considered. This is essential to reduce the uncertainties related to possibly unknown low energy physics, including solar modulation, and to disentangle the effects of reacceleration from those of diffusion.

One of the most important results of this analysis is that light nuclei (especially B/C) data and antiproton data can fit into a unique, coherent diffusion-reacceleration model of propagation, as it can be read off Fig. 3.2. Indeed, the confidence regions obtained for $E > 5$ GeV/n (where only the effects of diffusion and re-acceleration matters), light nuclei and antiproton CL regions nicely overlap to produce combined constraints on D_0/z_t, δ. While this was also shown in previous works (which however did not exploit the new CREAM data), a combined statistical analysis of nuclear and antiproton data has been performed here for the first time. We showed that such an analysis allows to narrow significantly the allowed values of δ and D_0/z_t: our constraints $0.3 < \delta < 0.6$ and $0.6 < D_0/z_t < 1$, as obtained at 95% C.L., are significantly more stringent that those previously determined in the related literature. Furthermore we found, for the first time, that only a relatively narrow range ($10 - 20$ km/ s) of the Alfvèn velocity values are allowed. Even well below 5 GeV/n, we showed that it is possible to find effective models which, still fulfilling those constraints, allow to nicely reproduce all relevant data. We also found that the preferred values of the N/O and C/O ratios at injection are ~ 6 % and ~ 75 % respectively. These results, and in particular the analysis of data with $E_{\rm min} = 5$ GeV/n, clearly favor a Kraichnan like CR diffusion ($\delta = 0.5$) respect to Kolmogorov ($\delta = 0.33$). It is worth noticing that a relatively large value of δ, as that preferred by our analysis, would give rise to a too large CR anisotropy if our results

are extrapolated to $E_k \gg 10^5$ GeV/n (see e.g. [158] and ref.s therein). Our results, therefore, may call for some changes in the standard CR propagation scenario.

Finally, we focused also on the effects on the expected secondary γ-ray diffuse emission. We showed that the longitude distribution of that emission can be significantly affected by in-homogeneous diffusion. In [171] it has been noticed that the effect goes in the right direction to provide a viable solution of the CR gradient problem. Here we confirm this claim and succeed reproducing EGRET observations for $4 < E < 10$ GeV and $|b| < 1^\circ$ for a reasonable choice of the relevant parameters. The extension of our predictions to larger latitudes would require to implement in DRAGON electron propagation (and losses) and more detailed gas and radiation distributions. We conclude by noticing that our predicted neutrino flux above 1 TeV along the GP is almost coincident with that derived in [171].

4

Light elements production by CRs

The relative abundance of light elements synthesized during the big bang nucleosynthesis (BBN) is a function of a single parameter, η, namely the baryon-to-photon ratio. Given the WMAP constraint $\eta = (6.8 \pm 0.21) \times 10^{-10}$, the light nuclei abundances can be precisely predicted by BBN [205, 206]. Despite a general agreement with the observed abundances of light elements, discrepancies arise concerning Li abundance. Observationally, the primordial abundance of lithium isotopes (^{7}Li and ^{6}Li), is measured in the atmospheres of Galactic metal-poor halo stars (MPHS).

Since the first detection by [207], later confirmed by subsequent works [208, 209, 210, 211] a ^{7}Li/H $= (1-2) \times 10^{-10}$ abundance was deduced, independent of stellar [Fe/H]. The presence of such a ^{7}Li plateau supports the idea that ^{7}Li is a primary element, synthesized by BBN. The measured value, however, results of a factor $2-4$ lower than the expected from the BBN ^{7}Li/H $= 4.27^{+1.02}_{-0.83} \times 10^{-10}$ [212], ^{7}Li/H $= 4.9^{+1.4}_{-1.2} \times 10^{-10}$ [213], or ^{7}Li/H $= 4.15^{+0.49}_{-0.45} \times 10^{-10}$ [214]. Recently, [215] and [216] found that mixing and diffusion processes during stellar evolution could reduce the ^{7}Li abundance in stellar atmospheres by about 0.2 dex, thus partially releasing the tension.

A more serious problem arose with ^{6}Li, for which the BBN predicts a value of $(^6\text{Li/H})_{\text{BBN}} \sim 10^{-14}$. Owing to the small difference in mass between ^{6}Li and ^{7}Li, lines from these two isotopes blend easily. The detection of ^{6}Li then results quite difficult since the predominance of ^{7}Li. Recently, high-resolution spectroscopic observations measured the ^{6}Li abundance in 24 MPHS [210], revealing the presence of a plateau ^{6}Li/H$= 6 \times 10^{-12}$ for $-3 \lesssim$ [Fe/H] $\lesssim -1$. A primordial origin of ^{6}Li

seems favoured by the presence of the plateau; however, the high ^{6}Li value observed cannot be reconciled with this hypothesis.

The solutions invoked to overcome the problem were: (i) a modification of BBN models [217, 218, 219, 220, 221], (ii) the fusion of ^{3}He accelerated by stellar flares with the atmospheric helium [222], (iii) a mechanism allowing for later production of ^{6}Li during Galaxy formation. The latter scenario involves the generation of cosmic rays (CRs). ^{6}Li, in fact, can be synthesized by fusion reactions ($\alpha + \alpha \rightarrow {}^6$Li) when high-energy CR particles collide with the ambient gas. Energetic CRs can either be accelerated by shock waves produced during cosmological structure formation processes [223, 224, 225] or, by strong supernova (SN) shocks along the build-up of the Galaxy. In their recent work [226] used the supernova rate (SNR) by [227] to compute the production of ^{6}Li in the intergalactic medium (IGM). Assuming that all MPHS form at $z \sim 3$, and from a gas with the same IGM composition, they obtained the observed ^{6}Li value. Despite the apparent success of the model, these assumptions are very idealized and require a closer inspection. We revisit the problem using a more realistic and data-constrained approach, based on the recent model by [106] (SSF07), which follows the hierarchical build-up of the Galaxy and reproduces the metallicity distribution of MPHS.

4.1 Building the Milky Way

The code GAlaxy Merger Tree & Evolution (GAMETE) described in SSF07 (updated version in 107) follows the star formation (SF)/chemical history of the MW along its merger tree, finally matching all its observed properties.

The code reconstructs the hierarchical merger history of the MW using a Monte Carlo algorithm based on the extended Press & Schechter theory [228] and adopting a binary scheme with accretion mass [113, 229]. Looking back in time at any time-step a halo can either lose part of its mass (corresponding to a cumulative fragmentation into haloes below the resolution limit $M_{\rm res}$) or lose mass and fragment into two progenitors. The mass below $M_{\rm res}$ accounts for the *Galactic Medium* (GM) which represents the mass reservoir into which haloes are embedded. During the evolution, progenitor haloes accrete gas from the GM and virialize out of it. We assume that feedback suppresses SF in mini-haloes and that only Lyα cooling haloes ($T_{\rm vir} >$

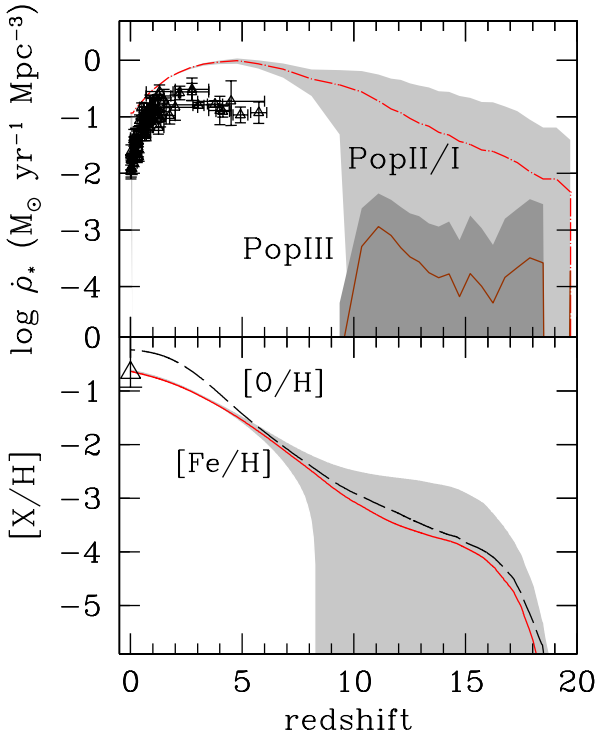

Figure 4.1 *Upper panel*: Comoving SFR density evolution for Pop III (solid line) and Pop II/I stars (dashed line). The curves are obtained after averaging over 100 realizations of the merger tree; shaded areas denote $\pm 1\sigma$ dispersion regions around the mean. Points represent the low-redshift measurements of the cosmic SFR by [236]. *Lower panel*: Corresponding GM iron (solid line) and oxygen (dashed line) abundance evolution. The point is the measured [O/H] abundance in high-velocity clouds by [237].

10^4 K) contribute stars and metals to the Galaxy. This motivates the choice of a resolution mass $M_{\rm res} = M_4(z)/10 = M(T_{\rm vir} = 10^4$ K $, z)/10$ where $M_4(z)$ is the mass corresponding to a virial temperature $T_{\rm vir} = 10^4$K at redshift z. At the highest redshift of the simulation, $z \approx 20$, the gas present in virialized haloes, as in the GM, is assumed to be of primordial composition. The SF rate (SFR) is taken to be proportional to the mass of gas. Following the critical metallicity scenario [230, 231, 232, 233, 234] we assume that low-mass (Pop II/I) SF occurs when the metallicity $Z_{\rm cr} > 10^{-5\pm1} Z_\odot$ according to a Larson initial mass function with a characteristic mass $m_\star = 0.35 M_\odot$. At lower Z massive Pop III stars form with a characteristic mass $m_{\rm PopIII} = 200 M_\odot$, i.e. within the pair-instability supernova ($\rm SN_{\gamma\gamma}$) mass range of $140-260 M_\odot$ [235]. The chemical evolution of both gas in proto-Galactic haloes (ISM) and in the GM, is computed by according to a mechanical feedback prescription (see [107] for details). Produced metals are instantaneously and homogeneously mixed with the gas.

The model free parameters are fixed to match the global properties of the MW and the Metallicity Distribution Function (MDF) of MPHS derived form the Hamburg-ESO Survey (Beers & Christlieb, private communication). In Fig. 4.1 (upper panel) the derived Galactic (comoving) SFR density is shown for Pop III and Pop II/I stars. Pop II/I stars dominate the SFR at any redshift. Following a burst of Pop III stars, in fact, the metallicity of the host halo raises to $Z > Z_{cr}$: chemical feedback suppresses Pop III formation in self-enriched progenitors. Later on Pop III stars can only form in those haloes which virialize from the GM and so, when $Z_{\rm GM} \gtrsim Z_{cr}$, their formation is totally quenched. The above results are in agreement with recent hydrodynamic simulations implementing chemical feedback effects (120). The earlier Pop III disappearance of our model ($z \sim 10$) with respect to this study ($z \sim 4$) is a consequence of the biased volume we consider i.e. the MW environment. As the higher mean density accelerates SF/metal enrichment, PopIII stars disappear at earlier times; the SFR maximum value and shape, however, match closely the simulated ones.

In Fig. 4.1 (lower panel) we show the corresponding evolution of the GM iron and oxygen abundance. As SSF07 have shown that the majority of present-day iron-poor stars ([Fe/H]< -2.5) formed in haloes accreting GM gas which was Fe-enhanced by previous SN explosions, the initial [Fe/H] abundance within a halo is set by the corresponding GM Fe-abundance at the virialization redshift.

4.2 Lithium production

To describe the production of ^{6}Li for a continuous source of CRs we generalize the classical work of [238], who developed a formalism to follow the propagation of an homogeneous CR population in an expanding universe, assuming that CRs have been instantaneously produced at some redshift.

Since the *primary* CRs are assumed to be produced by SNe, the physical source function $Q(E, z)$ is described by a power law in momentum:

$$Q(E, z) = C(z)\frac{\phi(E)}{\beta(E)}\ (\mathrm{GeV/n})^{-1}\,\mathrm{cm}^{-3}\,\mathrm{s}^{-1} \tag{4.1}$$

with $\beta = v/c$ and

$$\phi(E) = \frac{E + E_0}{[E(E + 2E_0)]^{(\gamma+1)/2}} \ (\mathrm{GeV/n})^{-1}\,\mathrm{cm}^{-2}\,\mathrm{s}^{-1} \tag{4.2}$$

where $\gamma = 2$ is the injection spectral index and $E_0 = 939$ MeV and E are, respectively, the rest-mass energy and the kinetic energy per nucleon. The functional form of the injection spectrum $\phi(E)$ is inferred from the theory of collisionless shock acceleration [239] and the γ value is the one typically associated to the case of strong shock. We note however that the results are only very weakly dependent on the spectral slope. Finally, $C(z)$ is a redshift-dependent normalization; its value is fixed at each redshift by normalizing $Q(E, z)$ to the total kinetic energy transferred to CRs by SN explosions:

$$\mathcal{E}_{\mathrm{SN}}(z) = \int_{E_{\mathrm{min}}}^{E_{\mathrm{max}}} EQ(E, z)\mathrm{d}E \tag{4.3}$$

with

$$\mathcal{E}_{\mathrm{SN}}(z) = \epsilon(1 + z)^3[E_{\mathrm{II}}\mathrm{SNR}_{\mathrm{II}}(z) + E_{\gamma\gamma}\mathrm{SNR}_{\gamma\gamma}(z)] \tag{4.4}$$

where $E_{\mathrm{II}} = 1.2 \times 10^{51}$ erg and $E_{\gamma\gamma} = 2.7 \times 10^{52}$ erg are, respectively, the average explosion energies for a Type II SN ($\mathrm{SN_{II}}$) and a $\mathrm{SN}_{\gamma\gamma}$; $\epsilon = 0.15$ is the fraction of the total energy not emitted in neutrinos transferred to CRs by a single SN, assumed to be the same for the two stellar populations; $\mathrm{SNR_{II}}$ ($\mathrm{SNR}_{\gamma\gamma}$) is the $\mathrm{SN_{II}}$ ($\mathrm{SN}_{\gamma\gamma}$) explosion comoving rate, simply proportional to the Pop II/I (Pop III) SFR. The efficiency parameter is inferred by shock acceleration theory and confirmed by recent observations of SN remnants in our Galaxy [240].

We now need to specify the energy limits E_{min}, E_{max} of the CR spectrum produced by SN shock waves (eq. 4.3). We fix $E_{\mathrm{max}} = 10^6$ GeV, following the theoretical estimate by [241]. Due to the rapid decrease of $\phi(E)$ the choice of E_{max} does not affect the result of the integration and hence the derived $C(z)$ value. On the contrary $C(z)$ strongly depends on the choice of E_{min}: the higher E_{min}, the higher is $C(z)$. Since observations cannot set tight constraints on E_{min}, due to solar magnetosphere modulation of low-E CRs, we consider it as a free parameter of the model.

Once the spectral shape of $Q(E, z)$ is fixed, we should in principle take in account the subsequent propagation of CRs both in the ISM and GM. Following [226], we make the hypothesis that primary CRs escape from parent galaxies on a timescale

short enough to be considered as immediately injected in the GM without energy losses. At high redshift in fact: (i) structures are smaller and less dense [242] implying higher diffusion efficiencies [243]; (ii) the magnetic field is weaker and so it can hardly confine CRs into structures. Note also that, besides diffusive propagation of CRs, superbubbles and/or galactic winds could directly eject CRs into the GM.

Under this hypothesis the density evolution of primary CRs only depends on energy losses suffered in the GM. The nuclei lose energy mainly via two processes, ionization and Hubble expansion, and they are destroyed by inelastic scattering off GM targets (mainly protons).

We can follow the evolution of α-particles (primary CRs) through the transport equation [238]

$$\frac{\partial N_{\alpha,\mathrm{H}}}{\partial t} + \frac{\partial}{\partial E}(bN_{\alpha,\mathrm{H}}) + \frac{N_{\alpha,\mathrm{H}}}{T_D} = K_{\alpha p} Q_{,\mathrm{H}}(E,z) \tag{4.5}$$

where $N_{i,H}$ is the ratio between the (physical) number density of species i and GM protons, $n_H(z) = n_{\mathrm{H},0}(1+z)^3$; $Q_{,\mathrm{H}}(E,z) \equiv Q(E,z)/n_{\mathrm{H}}(z)$ is the normalized physical source function, $b \equiv (\partial E/\partial t)$ is the total energy loss rate adopted from [226], T_D is the destruction term as in the analytic fit by [244]; finally, $K_{\alpha p} = 0.08$ is the cosmological abundance by number of α-particles with respect to protons.

We consider ^{6}Li as entirely secondary, i.e. purely produced by fusion of GM He-nuclei by primary α-particles. The physical source function for ^{6}Li is given by:

$$Q_{6\mathrm{Li}}(E,z) = \int \sigma_{\alpha\alpha\to 6\mathrm{Li}}(E,E') n_{\mathrm{He}}(z) \Phi_\alpha(E',z) \mathrm{d}E' \tag{4.6}$$

where E' and E are respectively the kinetic energies per nucleon of the incident particle and of the produced ^{6}Li nuclei, and $\Phi_\alpha(E',z) = \beta(E')N_\alpha(E',z)$ the incident α-particle flux. Making the approximation $\sigma_{\alpha\alpha\to 6\mathrm{Li}}(E,E') = \sigma_l(E)\delta(E - E'/4)$ [245] and defining $Q_{6\mathrm{Li,H}} \equiv Q_{6\mathrm{Li}}/n_{\mathrm{H}}$, the eq. (4.6) becomes

$$Q_{6\mathrm{Li,H}}(E,z) = \sigma_l(E) K_{\alpha p} n_{\mathrm{H}}(z) \Phi_{\alpha,\mathrm{H}}(4E,z) \tag{4.7}$$

where the cross section $\sigma_l(E)$ is given by the analytic fit of [246]:

$$\sigma_l(E) \sim 66 \exp\left(-\frac{E}{4\ \mathrm{MeV}}\right)\ \mathrm{mb} \tag{4.8}$$

We can now write a very simple equation describing the evolution of ^{6}Li:

$$\frac{\partial N_{\rm 6Li,H}}{\partial t} = Q_{\rm 6Li,H}(E,z) \tag{4.9}$$

in this case, in fact, destruction and energy losses are negligible since their time scales are very long with respect to the production time scale [247].

The solution of the coupled eqs. (4.5)-(4.9) gives ^{6}Li/H at any given redshift z.

4.3 Results

The system of equations introduced in the previous Sec. are solved numerically using a Crank-Nicholson implicit numerical scheme [248]. Because of its stability and robustness implicit schemes are used to solve transport equations in most CRs diffusion problems [249].

We test the accuracy of our code by studying a simplified case in which an analytic solution can be derived and compared with numerical results. To this aim we assume that: (i) both energy losses and destruction of primary CRs in the GM can be neglected; (ii) the physical energy density injected by SNe is constant, $\mathcal{E}_{\rm SN} \sim 7.4 \times 10^{-27}$ GeV cm^{-3} s^{-1}, in the redshift range $z > 3$. It is worth noting that the above hypothesis conspire to give an upper limit to the exact solution, thus providing an estimate of the maximum achievable ^{6}Li abundance. Under these approximations, the source spectrum defined in eq. (4.1) becomes:

$$Q(E,z) = 6.4 \cdot 10^{-29} \frac{\phi(\rm E)}{\beta(\rm E)} \, (\rm GeV/n)^{-1} \, cm^{-3} \, s^{-1} \tag{4.10}$$

and eqs. (4.5)-(4.9) can be solved. We find

$$N_{\alpha,\rm H}(z) = 39.6 \, (1+z)^{-9/2} \tag{4.11}$$

and

$$N_{\rm 6Li,H}(z) = 8.2 \times 10^{-11} (1+z)^{-3} \tag{4.12}$$

From Fig. 4.2 we conclude that the analytical solution for the GM ^{6}Li abundance (eq. 4.12) is perfectly matched by the numerical[1] one. Also shown are the numerical

[1]This solution represents an upper limit for the [226] model, as inferred from their Fig. 2.

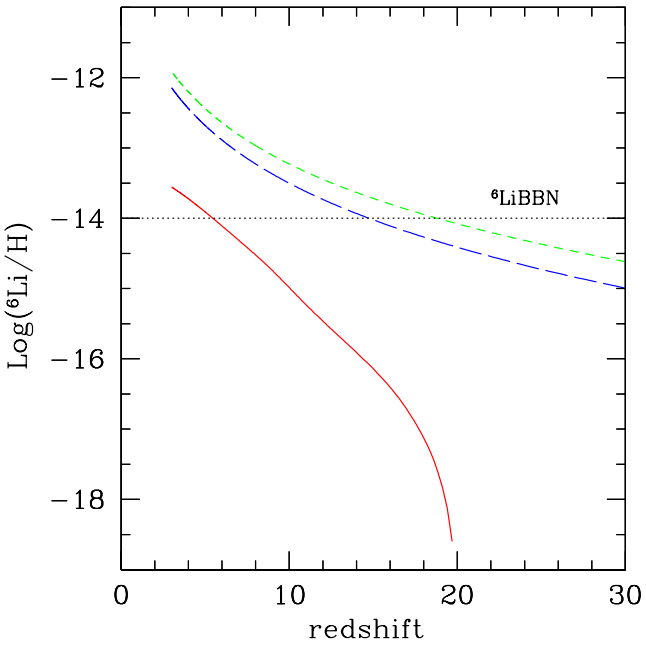

Figure 4.2 Redshift evolution of GM ^{6}Li/H abundance for the analytical (green short-dashed line) and numerical solution (overlapped) of a simplified model with no energy losses and destruction, and $\mathcal{E}_{\rm SN} = 7.4 \times 10^{-27}$ GeV cm^{-3} s^{-1} for $z > 3$, the same model including energy loss/destruction (blue long dashed line), the fiducial model with realistic SNR, $\epsilon = 0.15$ and $E_{\rm min} = 10^{-5}$ MeV (red solid line).

solutions obtained by relaxing first the hypothesis (i) and then (i) + (ii). Not unexpectedly, the inclusion of energy losses and destruction term into eq. (4.5) affects only slightly the result, as the typical time-scales of such processes are longer than the ^{6}Li production one.

A realistic injection energy, on the contrary, has a strong impact on the predicted shape and amplitude of the ^{6}Li evolution. In fact, the SFR, and consequently $\mathcal{E}_{\rm SN}$, is an increasing function of time in the analyzed redshift range (Fig. 4.1 upper panel). The maximum $\mathcal{E}_{\rm SN}$ we can obtain by using the SNR derived from the curve in Fig. 4.1, a realistic energy transfer efficiency $\epsilon = 0.15$, and $E_{\rm min} = 10^{-5}$ GeV [226], is $\mathcal{E}_{\rm SN}^{max} \sim 8.6 \times 10^{-28} < 7.4 \times 10^{-27}$ GeV cm^{-3} s^{-1}. Note that the ^{6}Li/H abundance at $z = 3$ results more than 1 order of magnitude smaller than the value of the simplified case. In the following, we will refer to this physical model as our fiducial model.

We now use the [Fe/H] predicted by GAMETE (Fig. 4.1, lower panel) to convert redshift into [Fe/H] values and derive the GM ^{6}Li vs [Fe/H]. According to our semi-analytical model for the build-up of the MW, in fact, the GM elemental abun-

dances reflect those of MPHS, which are predicted to form out of new virializing haloes accreting gas from the GM. This implies that the observed MPHS formed continuously within the redshift range $3 < z \leqslant 10$. From Fig. 4.3 we see that our fiducial model yields log ^{6}Li/H$= -13.5$, i.e. about three orders of magnitude below the data.

This discrepancy cannot be cured by simply boosting the free parameters to their maximum allowed values. This is also illustrated in the same Figure, where for the upper curve we assume $\epsilon = 1$, $E_{\rm min} = 10$ MeV/n [2] and for the SFR the maximum value allowed by GAMETE within 1-σ dispersion. Although the discrepancy between observations and model results is less prominent in this case, we are still unable to fit the data, in particular at [Fe/H] $= -3$ (i.e. at higher redshifts) only Log ^{6}Li/H$= -12.6$ has had time to be produced, failing short by 30 times.

In addition the flat data distribution cannot be recovered. It is worth noting that, as also pointed out by [210] ^{6}Li may be depleted in stars, mainly during the pre-main sequence phase. If this is the case, the ^{6}Li abundance observed in stars would not be representative of the gas from which they have formed. Taking into account this effect the inferred ^{6}Li abundances become metallicity dependent, i.e. the flatness is lost. Because of depletion however, the derived ^{6}Li values would be higher for all [Fe/H], making the discrepancy between our results and observations even larger.

We finally note, as already claimed by [226], that the production of ^{7}Li through this mechanism is comparable with that of ^{6}Li , being the production cross sections of the two isotopes very similar. No overproduction of ^{7}Li is then expected with respect of the BBN-based value.

4.4 Discussion

We have pointed out that both the level and flatness of the ^{6}Li distribution cannot be explained by CR spallation if these particles have been accelerated by SN shocks inside MW building blocks. Although previous claims [226] of a possible solution[3]

[2] This value is exceptionally high and corresponds to the energy at which the ^{6}Li production is most efficient. Thus the ^{6}Li production will be drastically reduced by increasing $E_{\rm min}$ above this value.

[3] Note that their eq. 18 contains an extra dz/dt term

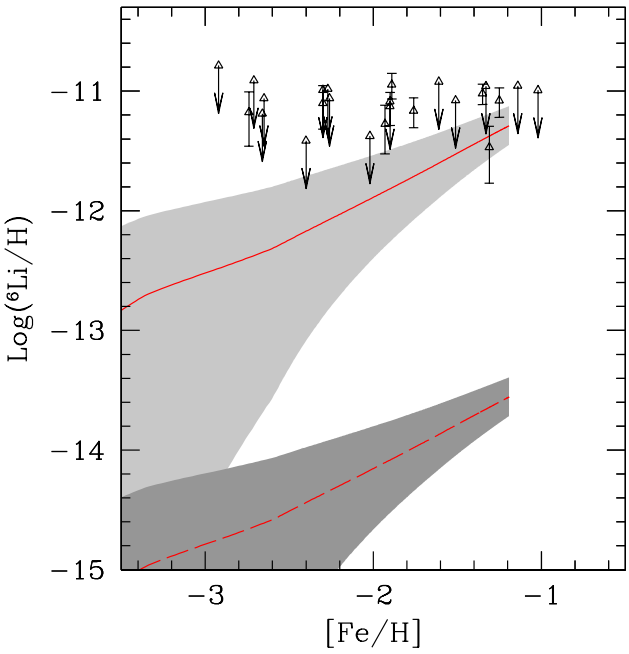

Figure 4.3 Redshift evolution of ^{6}Li/H vs [Fe/H] for the fiducial model ($\epsilon = 0.15$, $E_{\rm min} = 10^{-5}$ GeV/n, dashed line) and for the maximal model ($\epsilon = 1$, $E_{\rm min} = 10$ MeV/n, solid line). Shaded areas denote $\pm 1\sigma$ dispersion regions around the mean.

invoking the production of ^{6}Li in an early burst of PopIII stars have been put forward, such scenario is at odd with both the global properties of the MW and its halo MPHS.

Our model, which follows in detail the hierarchical build-up of the MW and reproduces correctly the MDF of the MPHS, predicts a monotonic increase of ^{6}Li abundance with time, and hence with [Fe/H]. Moreover, our fiducial model falls short of three orders of magnitude in explaining the data; such discrepancy cannot be cured by allowing the free parameters ($E_{\rm min}, \epsilon$) to take their maximum (physically unlikely) values. Apparently, a flat ^{6}Li distribution appears inconsistent with any (realistic) model for which CR acceleration energy is tapped from SNe: if so, ^{6}Li is continuously produced and destruction mechanisms are too inefficient to prevent its abundance to steadily increase along with [Fe/H].

Clearly, the actual picture could be more complex: for example, if the diffusion coefficient in the ISM of the progenitor galaxies is small enough, ^{6}Li could be produced *in situ* rather than in the more rarefied GM. This process might increase the species abundance, but cannot achieve the required decoupling of ^{6}Li evolution from the enrichment history.

Alternatively, shocks associated with structure formation might provide an alternative ^{6}Li production channel [224]; although potentially interesting as this mechanisms decouples metal enrichment (governed by SNe) and CR acceleration (due to structure formation shocks), the difficulties that this scenario must face are that (i) at the redshifts ($z = 2 - 3$) at which shocks are most efficient it must be still [Fe/H]< -3, and (ii) MPHS that formed at earlier epochs should have vanishing ^{6}Li abundance [250].

If these issues could represent insurmountable problems, then one has to resort to more exotic models involving either suitable modifications of BBN or some yet unknown production mechanism unrelated to cosmic SF history.

5

Concluding remarks

Extensive summaries on each aspect of my Thesis work have already been given at the end of each Chapter. For clarity, though, it might turn out useful to briefly reiterate the main findings of this thesis here, highlighting also future perspectives of my work, particularly in connection with upcoming observational results.

- Although turbulence is an important physical process in essentially all astrophysical environments, on the scale relevant to cosmological phenomena it has received a relatively meager attention. My present work aimed at making one of the first steps to quantify the amount of turbulent energy deposited in the IGM and there dissipated by galactic winds and to characterize its properties. My results clearly showed that turbulence contributes appreciably to the energy budget of the intergalactic gas affected by galaxy feedback, becoming more and more important at higher redshifts. If turbulence is indeed present in the IGM, as my study suggests, it might have relevant implications for a number of IGM studies that will be subject of future investigation. First, the long-standing problem of a discrepancy between the observed absorption line Doppler parameters and those deduced from numerical simulations of the Lyα forest might be alleviated by a proper inclusion of turbulence broadening. [102] convincingly demonstrated that only a model in which sub-resolution turbulence with an heuristic prescription based on the strength of the OVI absorption line is able to match observations. This confirms the correlation between turbulence and metal enrichment that we are planning to explore further. Secondly, the turbulent energy injection might affect the matter power-

spectrum determination from experiments using the Lyα forest as a probe, particularly on the smallest scales [251]. Third, if turbulence is largely present in the IGM it might result in a detectable signature in the scintillation of distant quasars [76, 252]. The IGM hosts the necessary conditions for scattering, is largely ionized and permeated by shocks from large scale formation or galactic feedback. Moreover, the long path lengths through the IGM can compensate for the lower density with respect to the ISM. This possibility was explored so far only as an *Ansatz*, to which my study now provides a more solid support. Next, turbulence might be carefully modeled in order to interpret the results for experiments aiming at directly measuring the change of the expansion rate of the Universe with time and the variability of fundamental constants [253, 254], as for example the proposed CODEX-ESPRESSO experiment. Last but not least, the relatively mild level of turbulence we find at $z \approx 3$ is consistent so far with the upper limits coming from observations. Moreover, it indicates that the IGM at those epochs had already dissipated a large fraction of the kinetic energy deposited at early times ($z > 5$) by the galaxies which initiated the metal enrichment and, possibly, the reionization process. All this well agrees with the idea that the metals we detect at moderate redshifts were mostly produced during a "pre-enrichment" phase of the IGM, by a population of small galaxies ancestors of the ones we study routinely in detail, the Lyman Break Galaxies.

- The origin of CRs represents an intriguing puzzle, which requires the combination of many different observations over a wide energy range to be solved. To this aim, my work so far has been focusing on the construction of a consistent model of CR propagation, taking into account diffusion and all the interactions of charged particles with the galactic environment. As already mentioned, I showed that it is possible to interpret all the CR data available in a consistent scenario. Forthcoming data from several running or scheduled experiments, as PAMELA (both for antiprotons and light nuclei), CREAM-II [155], TRACER [185, 186], and AMS-02 [190] which will measure both CR nuclei and $\bar{p}$ fluxes from hundreds MeV/n up to TeV/n, will soon allow tighter constraints. Especially AMS-02 is expected to provide very accurate data and, what is most relevant here, it will allow simultaneous and consistently calibrated measurements of several nuclear species and antiprotons (as well as electrons and

positrons which will also provide valuable complementary inputs). Moreover, CRs effects hold the promise to become the most appropriate and exciting candidate for indirect searches of Dark Matter signals in the Galaxy. The indirect detection of DM particles is based on the search for CRs anomalous components originating from DM annihilations in the Galactic halo, on top of the standard astrophysical production. These additional exotic components are potentially detectable on Earth and forthcoming missions will be specifically designed to target DM signals in CRs and diffuse γ-rays. The results presented in this Thesis noticeably constrain the main propagation parameters (and their allowed range) by using nuclear data only; this information can be used to model the CR background in analyses aimed at constraining or finding some exotic signal in antiproton and lepton data. Another interesting result I am planning to achieve soon is to reconstruct the spatial distribution of galactic magnetic fields by comparing the simulated synchrotron maps produced by DRAGON with the WMAP7 data (or the upcoming PLANCK ones). My code allows to simulate the electron distribution in the Galaxy in a consistent manner in which the diffusion coefficient itself depends on the galactic magnetic field parameters, thus largely improving previous analyses.

Bibliography

[1] S. N. Shore. *Astrophysical Hydrodynamics: An Introduction*. Wiley, 2007.

[2] L. D. Landau and E. M. Lifshitz. *Fluid mechanics*. Oxford: Pergamon Press, 1959.

[3] P. A. Davidson. *Turbulence : an introduction for scientists and engineers*. Oxford University Press, 2004.

[4] M. S. Longair. *High energy astrophysics. Vol.2: Stars, the galaxy and the interstellar medium*. Cambridge University Press, 1994.

[5] S. Chandrasekhar. Turbulence - a Physical Theory of Astrophysical Interest. *ApJ*, 110:329–+, November 1949.

[6] A. Brandenburg and A. Nordlund. Astrophysical turbulence. *ArXiv e-prints*, December 2009.

[7] A. Kolmogorov. The Local Structure of Turbulence in Incompressible Viscous Fluid for Very Large Reynolds' Numbers. *Akademiia Nauk SSSR Doklady*, 30:301–305, 1941.

[8] W. Heisenberg. On the Theory of Statistical and Isotropic Turbulence. *Royal Society of London Proceedings Series A*, 195:402–406, December 1948.

[9] J. O. Hinze. *Turbulence*. McGraw-Hill Mechanical Engineering, 1975.

[10] Leslie S. G. Kovasznay. The spectrum of locally isotropic turbulence. *Phys. Rev.*, 73(9):1115–1116, May 1948.

[11] C. A. Norman and A. Ferrara. The Turbulent Interstellar Medium: Generalizing to a Scale-dependent Phase Continuum. *ApJ*, 467:280–+, August 1996.

[12] R. H. Kraichnan. Inertial-Range Spectrum of Hydromagnetic Turbulence. *Physics of Fluids*, 8:1385–1387, July 1965.

[13] J. Cho and A. Lazarian. Compressible magnetohydrodynamic turbulence: mode coupling, scaling relations, anisotropy, viscosity-damped regime and astrophysical implications. *MNRAS*, 345:325–339, October 2003.

[14] J. Cho, A. Lazarian, and E. T. Vishniac. MHD Turbulence: Scaling Laws and Astrophysical Implications. In E. Falgarone & T. Passot, editor, *Turbulence and Magnetic Fields in Astrophysics*, volume 614 of *Lecture Notes in Physics, Berlin Springer Verlag*, pages 56–98, 2003.

[15] J. L. Phillips, S. J. Bame, W. C. Feldman, J. T. Gosling, C. M. Hammond, D. J. McComas, B. E. Goldstein, and M. Neugebauer. ULYSSES solar wind plasma observations during the declining phase of solar cycle 22. *Advances in Space Research*, 16:85–, August 1995.

[16] M. L. Goldstein, D. A. Roberts, and W. H. Matthaeus. Magnetohydrodynamic Turbulence In The Solar Wind. *ARA&A*, 33:283–326, 1995.

[17] C.-Y. Tu and E. Marsch. MHD structures, waves and turbulence in the solar wind: Observations and theories. *Space Science Reviews*, 73:1–210, July 1995.

[18] G. G. Howes, W. Dorland, S. C. Cowley, G. W. Hammett, E. Quataert, A. A. Schekochihin, and T. Tatsuno. Kinetic Simulations of Magnetized Turbulence in Astrophysical Plasmas. *Physical Review Letters*, 100(6):065004–+, February 2008.

[19] F. Sahraoui, M. L. Goldstein, P. Robert, and Y. V. Khotyaintsev. Evidence of a Cascade and Dissipation of Solar-Wind Turbulence at the Electron Gyroscale. *Physical Review Letters*, 102(23):231102–+, June 2009.

[20] J. W. Freeman. Estimates of solar wind heating inside 0.3 AU. *Geophysical Research Letters*, 15:88–91, January 1988.

[21] M. L. Goldstein, J. Hwang, F. Sahraoui, E. Lee, and G. K. Parks. First In-Situ Observation of Rolled-up Kelvin-Helmholtz Vortices under Southward IMF with Evidence of Reconnection. *AGU Fall Meeting Abstracts*, pages B1530+, December 2009.

[22] H. C. Spruit, A. Nordlund, and A. M. Title. Solar convection. *ARA&A*, 28:263–301, 1990.

[23] M. Asplund. New Light on Stellar Abundance Analyses: Departures from LTE and Homogeneity. *ARA&A*, 43:481–530, September 2005.

[24] E. Caffau, H.-G. Ludwig, M. Steffen, T. R. Ayres, P. Bonifacio, R. Cayrel, B. Freytag, and B. Plez. The photospheric solar oxygen project. I. Abundance analysis of atomic lines and influence of atmospheric models. *A&A*, 488:1031–1046, September 2008.

[25] M. Asplund, N. Grevesse, A. J. Sauval, and P. Scott. The Chemical Composition of the Sun. *ARA&A*, 47:481–522, September 2009.

[26] V. Ossenkopf and M.-M. Mac Low. Turbulent velocity structure in molecular clouds. *A&A*, 390:307–326, July 2002.

[27] R. B. Larson. Stellar kinematics and interstellar turbulence. *MNRAS*, 186:479–490, February 1979.

[28] R. B. Larson. Turbulence and star formation in molecular clouds. *MNRAS*, 194:809–826, March 1981.

[29] C. M. Brunt and M. H. Heyer. Interstellar Turbulence. II. Energy Spectra of Molecular Regions in the Outer Galaxy. *ApJ*, 566:289–301, February 2002.

[30] C. M. Brunt and M. H. Heyer. Interstellar Turbulence. I. Retrieval of Velocity Field Statistics. *ApJ*, 566:276–288, February 2002.

[31] C. M. Brunt, M. H. Heyer, and M.-M. Mac Low. Turbulent driving scales in molecular clouds. *A&A*, 504:883–890, September 2009.

[32] B. J. Rickett. Radio propagation through the turbulent interstellar plasma. *ARA&A*, 28:561–605, 1990.

[33] S. Boldyrev and C. Gwinn. Scintillations and Lévy Flights through the Interstellar Medium. *ApJ*, 584:791–796, February 2003.

[34] M. A. de Avillez and D. Breitschwerdt. Global dynamical evolution of the ISM in star forming galaxies. I. High resolution 3D simulations: Effect of the magnetic field. *A&A*, 436:585–600, June 2005.

[35] T. H. Troland and R. M. Crutcher. Magnetic Fields in Dark Cloud Cores: Arecibo OH Zeeman Observations. *ApJ*, 680:457–465, June 2008.

[36] R. M. Crutcher, N. Hakobian, and T. H. Troland. Testing Magnetic Star Formation Theory. *ApJ*, 692:844–855, February 2009.

[37] R. M. Crutcher. OH and CN Zeeman Observations of Magnetic Fields in Molecular Clouds. In *Revista Mexicana de Astronomia y Astrofisica Conference Series*, volume 36 of *Revista Mexicana de Astronomia y Astrofisica Conference Series*, pages 107–112, August 2009.

[38] F. Yusef-Zadeh, M. Morris, and D. Chance. Large, highly organized radio structures near the galactic centre. *Nature*, 310:557–561, August 1984.

[39] F. Yusef-Zadeh, J. W. Hewitt, and W. Cotton. A 20 Centimeter Survey of the Galactic Center Region. I. Detection of Numerous Linear Filaments. *ApJS*, 155:421–550, December 2004.

[40] R. Beck, A. Brandenburg, D. Moss, A. Shukurov, and D. Sokoloff. Galactic Magnetism: Recent Developments and Perspectives. *ARA&A*, 34:155–206, 1996.

[41] B. G. Elmegreen and J. Scalo. Interstellar Turbulence I: Observations and Processes. *ARA&A*, 42:211–273, September 2004.

[42] E. Falgarone, J.-L. Puget, and M. Perault. The small-scale density and velocity structure of quiescent molecular clouds. *A&A*, 257:715–730, April 1992.

[43] P. Padoan and Å. Nordlund. The Stellar Initial Mass Function from Turbulent Fragmentation. *ApJ*, 576:870–879, September 2002.

[44] M.-M. Mac Low and R. S. Klessen. Control of star formation by supersonic turbulence. *Reviews of Modern Physics*, 76:125–194, January 2004.

[45] J. Ballesteros-Paredes, R. S. Klessen, M.-M. Mac Low, and E. Vazquez-Semadeni. Molecular Cloud Turbulence and Star Formation. *Protostars and Planets V*, pages 63–80, 2007.

[46] C. F. McKee and E. C. Ostriker. Theory of Star Formation. *ARA&A*, 45:565–687, September 2007.

[47] J. M. Miller, J. Raymond, A. Fabian, D. Steeghs, J. Homan, C. Reynolds, M. van der Klis, and R. Wijnands. The magnetic nature of disk accretion onto black holes. *Nature*, 441:953–955, June 2006.

[48] S. A. Balbus and J. F. Hawley. Instability, turbulence, and enhanced transport in accretion disks. *Reviews of Modern Physics*, 70:1–53, January 1998.

[49] K. Cai, R. H. Durisen, A. C. Boley, M. K. Pickett, and A. C. Mejía. The Thermal Regulation of Gravitational Instabilities in Protoplanetary Disks. IV. Simulations with Envelope Irradiation. *ApJ*, 673:1138–1153, February 2008.

[50] S. A. Michael, T. Steiman-Cameron, R. Durisen, and A. Boley. Effective Alphas and Mixing for Disks with Gravitational Instabilities: Convergence Testing in Global 3D Simulations. In *Bulletin of the American Astronomical Society*, volume 40 of *Bulletin of the American Astronomical Society*, pages 201–+, May 2008.

[51] J. Frank, A. King, and D. Raine. *Accretion power in astrophysics.* Camb. Astrophys. Ser., Vol. 21, 1992.

[52] C. Loken, K. Roettiger, J. O. Burns, and M. Norman. Radio jet propagation and wide-angle tailed radio sources in merging galaxy cluster environments. *ApJ*, 445:80–97, May 1995.

[53] D. R. Wik, C. L. Sarazin, P. M. Ricker, and S. W. Randall. The Impact of Galaxy Cluster Mergers on Cosmological Parameter Estimation from Surveys of the Sunyaev-Zel'dovich Effect. *ApJ*, 680:17–31, June 2008.

[54] M. Birkinshaw. The Sunyaev-Zel'dovich effect. *Phys. Rep.*, 310:97–195, March 1999.

[55] K. Roettiger, J. O. Burns, and J. M. Stone. A Cluster Merger and the Origin of the Extended Radio Emission in Abell 3667. *ApJ*, 518:603–612, June 1999.

[56] K. Roettiger, J. M. Stone, and J. O. Burns. Magnetic Field Evolution in Merging Clusters of Galaxies. *ApJ*, 518:594–602, June 1999.

[57] K. Subramanian, A. Shukurov, and N. E. L. Haugen. Evolving turbulence and magnetic fields in galaxy clusters. *MNRAS*, 366:1437–1454, March 2006.

[58] W. Jaffe. On the morphology of the magnetic field in galaxy clusters. *ApJ*, 241:925–927, November 1980.

[59] A. Ruzmaikin, D. Sokolov, and A. Shukurov. The dynamo origin of magnetic fields in galaxy clusters. *MNRAS*, 241:1–14, November 1989.

[60] I. Goldman and Y. Rephaeli. Turbulently generated magnetic fields in clusters of galaxies. *ApJ*, 380:344–350, October 1991.

[61] V. S. Berezinskii, S. V. Bulanov, V. A. Dogiel, and V. S. Ptuskin. *Astrophysics of cosmic rays*. Amsterdam: North-Holland, 1990.

[62] C. F. Kennel and F. Engelmann. Velocity Space Diffusion from Weak Plasma Turbulence in a Magnetic Field. *Physics of Fluids*, 9:2377–2388, November 1966.

[63] J. R. Jokipii. Propagation of cosmic rays in the solar wind. *Reviews of Geophysics and Space Physics*, 9:27–87, 1971.

[64] R. Schlickeiser. *Cosmic Ray Astrophysics*. Springer, 2002.

[65] P. Goldreich and S. Sridhar. Toward a theory of interstellar turbulence. 2: Strong alfvenic turbulence. *ApJ*, 438:763–775, January 1995.

[66] H. Yan and A. Lazarian. Cosmic-Ray Scattering and Streaming in Compressible Magnetohydrodynamic Turbulence. *ApJ*, 614:757–769, October 2004.

[67] M. Rauch, W. L. W. Sargent, and T. A. Barlow. Small-Scale Structure at High Redshift. II. Physical Properties of the C IV Absorbing Clouds. *ApJ*, 554:823–840, June 2001.

[68] L. L. Cowie, A. Songaila, T.-S. Kim, and E. M. Hu. The metallicity and internal structure of the Lyman-alpha forest clouds. *AJ*, 109:1522–1530, April 1995.

[69] S. A. Kaplan and S. B. Pikelner. *The interstellar medium.* Harvard University Press, 1970.

[70] W. R. Oegerle, T. M. Tripp, K. R. Sembach, E. B. Jenkins, D. V. Bowen, L. L. Cowie, R. F. Green, J. W. Kruk, B. D. Savage, J. M. Shull, and D. G. York. Far Ultraviolet Spectroscopic Explorer Observations of the Galactic and Intergalactic Medium toward H1821+643. *ApJL*, 538:L23–L26, July 2000.

[71] T. M. Tripp and B. D. Savage. O VI and Multicomponent H I Absorption Associated with a Galaxy Group in the Direction of PG 0953+415: Physical Conditions and Baryonic Content. *ApJ*, 542:42–56, October 2000.

[72] K. R. Sembach, J. C. Howk, B. D. Savage, J. M. Shull, and W. R. Oegerle. Far-Ultraviolet Spectroscopy of the Intergalactic and Interstellar Absorption toward 3C 273. *ApJ*, 561:573–599, November 2001.

[73] B. D. Savage, K. R. Sembach, T. M. Tripp, and P. Richter. Far Ultraviolet Spectroscopic Explorer and Space Telescope Imaging Spectrograph Observations of Intervening O VI Absorption Line Systems in the Spectrum of PG 0953+415. *ApJ*, 564:631–649, January 2002.

[74] J. M. Cordes, T. J. W. Lazio, and M. A. McLaughlin. The dynamic radio sky. *New Astronomy Reviews*, 48:1459–1472, December 2004.

[75] A. N. Hall and D. W. Sciama. The angular broadening of compact radio sources observed through ionized gas in a rich cluster of galaxies. *ApJL*, 228:L15–L18, February 1979.

[76] A. Ferrara and R. Perna. Scintillation as a probe of the intergalactic medium. *MNRAS*, 325:1643–1648, August 2001.

[77] D. R. Lorimer, M. Bailes, M. A. McLaughlin, D. J. Narkevic, and F. Crawford. A Bright Millisecond Radio Burst of Extragalactic Origin. *Science*, 318:777–, November 2007.

[78] J. P. Macquart. Limits on the Detection of Transients Imposed by Scattering. In *Bursts, Pulses and Flickering: Wide-Field Monitoring of the Dynamic Radio Sky*, 2007.

[79] A. Songaila and L. L. Cowie. Metal enrichment and Ionization Balance in the Lyman Alpha Forest at Z = 3. *AJ*, 112:335–+, August 1996.

[80] R. Davé, U. Hellsten, L. Hernquist, N. Katz, and D. H. Weinberg. Constraining the Metallicity of the Low-Density Lyalpha Forest Using O VI Absorption. *ApJ*, 509:661–677, December 1998.

[81] J. Schaye, M. Rauch, W. L. W. Sargent, and T.-S. Kim. The Detection of Oxygen in the Low-Density Intergalactic Medium. *ApJ*, 541:L1–L4, September 2000.

[82] M. Pettini, P. Madau, M. Bolte, J. X. Prochaska, S. L. Ellison, and X. Fan. The C IV Mass Density of the Universe at Redshift 5. *ApJ*, 594:695–703, September 2003.

[83] J. Schaye, A. Aguirre, T.-S. Kim, T. Theuns, M. Rauch, and W. L. W. Sargent. Metallicity of the Intergalactic Medium Using Pixel Statistics. II. The Distribution of Metals as Traced by C IV. *ApJ*, 596:768–796, October 2003.

[84] A. Aguirre, J. Schaye, T.-S. Kim, T. Theuns, M. Rauch, and W. L. W. Sargent. Metallicity of the Intergalactic Medium Using Pixel Statistics. III. Silicon. *ApJ*, 602:38–50, February 2004.

[85] R. A. Simcoe, W. L. W. Sargent, and M. Rauch. The Distribution of Metallicity in the Intergalactic Medium at z˜2.5: O VI and C IV Absorption in the Spectra of Seven QSOs. *ApJ*, 606:92–115, May 2004.

[86] S. L. Ellison, A. Songaila, J. Schaye, and M. Pettini. The Enrichment History of the Intergalactic Medium-Measuring the C IV/H I Ratio in the Lyα Forest. *AJ*, 120:1175–1191, September 2000.

[87] A. Songaila. The Minimum Universal Metal Density between Redshifts of 1.5 and 5.5. *ApJ*, 561:L153–L156, November 2001.

[88] E. V. Ryan-Weber, M. Pettini, P. Madau, and B. J. Zych. A downturn in intergalactic CIV as redshift 6 is approached. *MNRAS*, 395:1476–1490, May 2009.

[89] M.-M. Mac Low and A. Ferrara. Starburst-driven Mass Loss from Dwarf Galaxies: Efficiency and Metal Ejection. *ApJ*, 513:142–155, March 1999.

[90] A. Ferrara, M. Pettini, and Y. Shchekinov. Mixing metals in the early Universe. *MNRAS*, 319:539–548, December 2000.

[91] A. Aguirre, L. Hernquist, J. Schaye, N. Katz, D. H. Weinberg, and J. Gardner. Metal Enrichment of the Intergalactic Medium in Cosmological Simulations. *ApJ*, 561:521–549, November 2001.

[92] B. D. Oppenheimer and R. Davé. Cosmological simulations of intergalactic medium enrichment from galactic outflows. *MNRAS*, 373:1265–1292, December 2006.

[93] R. Cen and N. E. Chisari. Star Formation Feedback and Metal Enrichment History Of The Intergalactic Medium. *ArXiv e-prints*, May 2010.

[94] T. M. Heckman. Galactic Superwinds at Low and High Redshift. In J. E. Hibbard, M. Rupen, & J. H. van Gorkom, editor, *Gas and Galaxy Evolution*, volume 240 of *Astronomical Society of the Pacific Conference Series*, pages 345–+, 2001.

[95] M. Pettini, A. E. Shapley, C. C. Steidel, J.-G. Cuby, M. Dickinson, A. F. M. Moorwood, K. L. Adelberger, and M. Giavalisco. The Rest-Frame Optical Spectra of Lyman Break Galaxies: Star Formation, Extinction, Abundances, and Kinematics. *ApJ*, 554:981–1000, June 2001.

[96] K. L. Adelberger, C. C. Steidel, A. E. Shapley, and M. Pettini. Galaxies and Intergalactic Matter at Redshift z˜3: Overview. *ApJ*, 584:45–75, February 2003.

[97] A. E. Shapley, C. C. Steidel, M. Pettini, and K. L. Adelberger. Rest-Frame Ultraviolet Spectra of z˜3 Lyman Break Galaxies. *ApJ*, 588:65–89, May 2003.

[98] C. F. McKee and J. P. Ostriker. A theory of the interstellar medium - Three components regulated by supernova explosions in an inhomogeneous substrate. *ApJ*, 218:148–169, November 1977.

[99] M.-M. Mac Low and R. S. Klessen. Control of star formation by supersonic turbulence. *Reviews of Modern Physics*, 76:125–194, January 2004.

[100] A. Meiksin, G. Bryan, and M. Machacek. Hydrodynamical simulations of the Lyα forest: data comparisons. *MNRAS*, 327:296–322, October 2001.

[101] A. A. Meiksin. The physics of the intergalactic medium. *Reviews of Modern Physics*, 81:1405–1469, October 2009.

[102] B. D. Oppenheimer and R. Davé. The nature and origin of low-redshift OVI absorbers. *MNRAS*, 395:1875–1904, June 2009.

[103] E. Scannapieco and M. Brüggen. Simulating supersonic turbulence in galaxy outflows. *MNRAS*, pages 583–+, April 2010.

[104] D. Ryu, H. Kang, J. Cho, and S. Das. Turbulence and Magnetic Fields in the Large-Scale Structure of the Universe. *Science*, 320:909–, May 2008.

[105] W. Zhu, L.-l. Feng, and L.-Z. Fang. Vorticity of Intergalactic Medium Velocity Field on Large Scales. *ApJ*, 712:1–13, March 2010.

[106] S. Salvadori, R. Schneider, and A. Ferrara. Cosmic stellar relics in the Galactic halo. *MNRAS*, 381:647–662, October 2007.

[107] S. Salvadori, A. Ferrara, and R. Schneider. Life and times of dwarf spheroidal galaxies. *MNRAS*, 386:348–358, May 2008.

[108] C. Lacey and S. Cole. Merger rates in hierarchical models of galaxy formation. *MNRAS*, 262:627–649, June 1993.

[109] G. Kauffmann and S. D. M. White. The merging history of dark matter haloes in a hierarchical universe. *MNRAS*, 261:921–928, April 1993.

[110] R. S. Somerville and T. S. Kolatt. How to plant a merger tree. *MNRAS*, 305:1–14, May 1999.

[111] V. Springel, S. D. M. White, A. Jenkins, C. S. Frenk, N. Yoshida, L. Gao, J. Navarro, R. Thacker, D. Croton, J. Helly, J. A. Peacock, S. Cole, P. Thomas, H. Couchman, A. Evrard, J. Colberg, and F. Pearce. Simulations of the formation, evolution and clustering of galaxies and quasars. *Nature*, 435:629–636, June 2005.

[112] R. K. Sheth and G. Lemson. The forest of merger history trees associated with the formation of dark matter haloes. *MNRAS*, 305:946–956, May 1999.

[113] S. Cole, C. G. Lacey, C. M. Baugh, and C. S. Frenk. Hierarchical galaxy formation. *MNRAS*, 319:168–204, November 2000.

[114] H. Parkinson, S. Cole, and J. Helly. Generating dark matter halo merger trees. *MNRAS*, 383:557–564, January 2008.

[115] J. Dunkley, E. Komatsu, M. R. Nolta, D. N. Spergel, D. Larson, G. Hinshaw, L. Page, C. L. Bennett, B. Gold, N. Jarosik, J. L. Weiland, M. Halpern, R. S. Hill, A. Kogut, M. Limon, S. S. Meyer, G. S. Tucker, E. Wollack, and E. L. Wright. Five-Year Wilkinson Microwave Anisotropy Probe Observations: Likelihoods and Parameters from the WMAP Data. *ApJS*, 180:306–329, February 2009.

[116] R. Barkana and A. Loeb. In the beginning: the first sources of light and the reionization of the universe. *Phys. Rep.*, 349:125–238, July 2001.

[117] R. B. Larson. Effects of supernovae on the early evolution of galaxies. *MNRAS*, 169:229–246, November 1974.

[118] A. Dekel and J. Silk. The origin of dwarf galaxies, cold dark matter, and biased galaxy formation. *ApJ*, 303:39–55, April 1986.

[119] A. Ferrara and E. Tolstoy. The role of stellar feedback and dark matter in the evolution of dwarf galaxies. *MNRAS*, 313:291–309, April 2000.

[120] L. Tornatore, A. Ferrara, and R. Schneider. Population III stars: hidden or disappeared? *MNRAS*, 382:945–950, December 2007.

[121] B. M. Tinsley. Evolution of the Stars and Gas in Galaxies. *Fundamentals of Cosmic Physics*, 5:287–388, 1980.

[122] R. B. Larson. Early star formation and the evolution of the stellar initial mass function in galaxies. *MNRAS*, 301:569–581, December 1998.

[123] L. B. van den Hoek and M. A. T. Groenewegen. New theoretical yields of intermediate mass stars. *A&A Supp.*, 123:305–328, June 1997.

[124] S. E. Woosley and T. A. Weaver. The Evolution and Explosion of Massive Stars. II. Explosive Hydrodynamics and Nucleosynthesis. *ApJS*, 101:181–+, November 1995.

[125] A. S. Kompaneets. A Point Explosion in an Inhomogeneous Atmosphere. *Soviet Physics Doklady*, 5:46–+, July 1960.

[126] Jeremiah P. Ostriker and Christopher F. McKee. Astrophysical blastwaves. *Rev. Mod. Phys.*, 60:1–68, 1988.

[127] P. Madau, A. Ferrara, and M. J. Rees. Early Metal Enrichment of the Intergalactic Medium by Pregalactic Outflows. *ApJ*, 555:92–105, July 2001.

[128] M.-M. Mac Low and R. McCray. Superbubbles in disk galaxies. *ApJ*, 324:776–785, January 1988.

[129] Julio F. Navarro, Carlos S. Frenk, and Simon D. M. White. A Universal Density Profile from Hierarchical Clustering. *Astrophys. J.*, 490:493–508, 1997.

[130] T. R. Choudhury and A. Ferrara. Updating reionization scenarios after recent data. *MNRAS*, 371:L55–L59, September 2006.

[131] R. S. Sutherland and M. A. Dopita. Cooling functions for low-density astrophysical plasmas. *ApJS*, 88:253–327, September 1993.

[132] S. Ikeuchi and J. P. Ostriker. Evolution of the intergalactic medium - What happened during the epoch Z = 3-10? *ApJ*, 301:522–543, February 1986.

[133] A. Lazarian and J. Cho. Basic Properties of Compressible MHD Turbulence: Implications for Molecular Clouds. *Ap&SS*, 292:29–43, July 2004.

[134] G. Kowal and A. Lazarian. Scaling Relations of Compressible MHD Turbulence. *ApJL*, 666:L69–L72, September 2007.

[135] W. Schmidt, C. Federrath, M. Hupp, S. Kern, and J. C. Niemeyer. Numerical simulations of compressively driven interstellar turbulence. I. Isothermal gas. *A&A*, 494:127–145, January 2009.

[136] A. M. Bykov and I. N. Toptygin. Effect of shocks on interstellar turbulence and cosmic-ray dynamics. *Ap&SS*, 138:341–354, November 1987.

[137] A. Brandenburg, M. J. Korpi, and A. J. Mee. Thermal Instability in Shearing and Periodic Turbulence. *ApJ*, 654:945–954, January 2007.

[138] A. M. Hopkins and J. F. Beacom. On the Normalization of the Cosmic Star Formation History. *ApJ*, 651:142–154, November 2006.

[139] X. X. Xue, H. W. Rix, G. Zhao, P. Re Fiorentin, T. Naab, M. Steinmetz, F. C. van den Bosch, T. C. Beers, Y. S. Lee, E. F. Bell, C. Rockosi, B. Yanny, H. Newberg, R. Wilhelm, X. Kang, M. C. Smith, and D. P. Schneider. The Milky Way's Circular Velocity Curve to 60 kpc and an Estimate of the Dark Matter Halo Mass from the Kinematics of ˜2400 SDSS Blue Horizontal-Branch Stars. *ApJ*, 684:1143–1158, September 2008.

[140] W. Dehnen and J. Binney. Mass models of the Milky Way. *MNRAS*, 294:429–+, March 1998.

[141] A. G. A. Brown, H. M. Velázquez, and L. A. Aguilar. Detection of satellite remnants in the Galactic Halo with Gaia- I. The effect of the Galactic background, observational errors and sampling. *MNRAS*, 359:1287–1305, June 2005.

[142] S. W. Stahler and F. Palla. *The Formation of Stars*. Wiley-VCH, January 2005.

[143] N. Murray and M. Rahman. Star Formation in Massive Clusters Via the Wilkinson Microwave Anisotropy Probe and the Spitzer Glimpse Survey. *ApJ*, 709:424–435, January 2010.

[144] S. Bertone, F. Stoehr, and S. D. M. White. Semi-analytic simulations of galactic winds: volume filling factor, ejection of metals and parameter study. *MNRAS*, 359:1201–1216, June 2005.

[145] S. Samui, K. Subramanian, and R. Srianand. Constrained semi-analytical models of galactic outflows. *MNRAS*, 385:783–808, April 2008.

[146] T. Theuns, A. Leonard, G. Efstathiou, F. R. Pearce, and P. A. Thomas. P^3M-SPH simulations of the Lyalpha forest. *MNRAS*, 301:478–502, December 1998.

[147] F. Haardt and P. Madau. Radiative Transfer in a Clumpy Universe. II. The Ultraviolet Extragalactic Background. *ApJ*, 461:20–+, April 1996.

[148] J. Schaye, T. Theuns, M. Rauch, G. Efstathiou, and W. L. W. Sargent. The thermal history of the intergalactic medium. *MNRAS*, 318:817–826, November 2000.

[149] M. Ricotti, N. Y. Gnedin, and J. M. Shull. The Evolution of the Effective Equation of State of the Intergalactic Medium. *ApJ*, 534:41–56, May 2000.

[150] V. D'Odorico, M. Bruscoli, F. Saitta, F. Fontanot, M. Viel, S. Cristiani, and P. Monaco. The quasar proximity effect at redshift $z \sim 2.6$ with the From Lines to Overdensities approach. *MNRAS*, 389:1727–1738, October 2008.

[151] F. Saitta, V. D'Odorico, M. Bruscoli, S. Cristiani, P. Monaco, and M. Viel. Tracing the gas at redshift 1.7-3.5 with the Lyα forest: the FLO approach. *MNRAS*, 385:519–530, March 2008.

[152] D. Kirkman and D. Tytler. The transverse proximity effect in the z ˜ 2 Lyman α forest suggests quasi-stellar object episodic lifetimes of ˜1 Myr. *MNRAS*, 391:1457–1471, December 2008.

[153] A. W. Strong, I. V. Moskalenko, and V. S. Ptuskin. Cosmic-Ray Propagation and Interactions in the Galaxy. *Annual Review of Nuclear and Particle Science*, 57:285–327, November 2007.

[154] A. Castellina and F. Donato. Diffusion coefficient and acceleration spectrum from direct measurements of charged cosmic ray nuclei. *Astroparticle Physics*, 24:146–159, September 2005.

[155] H. S. Ahn, P. S. Allison, M. G. Bagliesi, J. J. Beatty, G. Bigongiari, P. J. Boyle, T. J. Brandt, J. T. Childers, N. B. Conklin, S. Coutu, M. A. Duvernois, O. Ganel, J. H. Han, H. J. Hyun, J. A. Jeon, K. C. Kim, J. K. Lee, M. H. Lee, L. Lutz, P. Maestro, A. Malinin, P. S. Marrocchesi, S. A. Minnick, S. I. Mognet, S. Nam, S. L. Nutter, I. H. Park, N. H. Park, E. S. Seo, R. Sina, S. P. Swordy, S. P. Wakely, J. Wu, J. Yang, Y. S. Yoon, R. Zei, and S. Y. Zinn. Measurements of cosmic-ray secondary nuclei at high energies with the first flight of the CREAM balloon-borne experiment. *Astroparticle Physics*, 30:133–141, October 2008.

[156] O. Adriani, G. C. Barbarino, G. A. Bazilevskaya, R. Bellotti, M. Boezio, E. A. Bogomolov, L. Bonechi, M. Bongi, V. Bonvicini, S. Bottai, A. Bruno, F. Cafagna, D. Campana, P. Carlson, M. Casolino, G. Castellini, M. P. de Pascale, G. de Rosa, D. Fedele, A. M. Galper, L. Grishantseva, P. Hofverberg, A. Leonov, S. V. Koldashov, S. Y. Krutkov, A. N. Kvashnin, V. Malvezzi, L. Marcelli, W. Menn, V. V. Mikhailov, M. Minori, E. Mocchiutti, M. Nagni, S. Orsi, G. Osteria, P. Papini, M. Pearce, P. Picozza, M. Ricci, S. B. Ricciarini, M. Simon, R. Sparvoli, P. Spillantini, Y. I. Stozhkov, E. Taddei, A. Vacchi, E. Vannuccini, G. Vasilyev, S. A. Voronov, Y. T. Yurkin, G. Zampa, N. Zampa, and V. G. Zverev. New Measurement of the Antiproton-to-Proton Flux Ratio up to 100 GeV in the Cosmic Radiation. *Physical Review Letters*, 102(5):051101–+, February 2009.

[157] M. Pato, D. Hooper, and M. Simet. Pinpointing cosmic ray propagation with the

AMS-02 experiment. *Journal of Cosmology and Astro-Particle Physics*, 6:22–+, June 2010.

[158] P. Blasi. Direct Measurements, Acceleration and Propagation of Cosmic Rays. *ArXiv e-prints*, January 2008.

[159] P. Blasi. Origin of the Positron Excess in Cosmic Rays. *Physical Review Letters*, 103(5):051104–+, July 2009.

[160] L. Bergström, J. Edsjö, and P. Ullio. Cosmic Antiprotons as a Probe for Supersymmetric Dark Matter? *ApJ*, 526:215–235, November 1999.

[161] L. Bergström, G. Bertone, T. Bringmann, J. Edsjö, and M. Taoso. Gamma-ray and radio constraints of high positron rate dark matter models annihilating into new light particles. *Phys. Rev. D*, 79(8):081303–+, April 2009.

[162] G. Bertone, M. Cirelli, A. Strumia, and M. Taoso. Gamma-ray and radio tests of the e^+ excess from DM annihilations. *Journal of Cosmology and Astro-Particle Physics*, 3:9–+, March 2009.

[163] M. Cirelli, M. Kadastik, M. Raidal, and A. Strumia. Model-independent implications of the e^+, $\bar{p}$ cosmic ray spectra on properties of Dark Matter. *Nuclear Physics B*, 813:1–21, May 2009.

[164] I. V. Moskalenko, A. W. Strong, J. F. Ormes, and M. S. Potgieter. Secondary Antiprotons and Propagation of Cosmic Rays in the Galaxy and Heliosphere. *ApJ*, 565:280–296, January 2002.

[165] F. Donato, D. Maurin, P. Salati, A. Barrau, G. Boudoul, and R. Taillet. Antiprotons from Spallations of Cosmic Rays on Interstellar Matter. *ApJ*, 563:172–184, December 2001.

[166] C. Evoli, D. Gaggero, D. Grasso, and L. Maccione. Cosmic ray nuclei, antiprotons and gamma rays in the galaxy: a new diffusion model. *Journal of Cosmology and Astro-Particle Physics*, 10:18–+, October 2008.

[167] V. L. Ginzburg and S. I. Syrovatskii. *The Origin of Cosmic Rays*. Macmillan, 1964.

[168] D. Maurin, F. Donato, R. Taillet, and P. Salati. Cosmic Rays below Z=30 in a Diffusion Model: New Constraints on Propagation Parameters. *ApJ*, 555:585–596, July 2001.

[169] A. W. Strong and I. V. Moskalenko. Propagation of Cosmic-Ray Nucleons in the Galaxy. *ApJ*, 509:212–228, December 1998.

[170] A. W. Strong, I. V. Moskalenko, O. Reimer, S. Digel, and R. Diehl. The distribution of cosmic-ray sources in the Galaxy, γ-rays and the gradient in the CO-to-H_2 relation. *A&A*, 422:L47–L50, July 2004.

[171] C. Evoli, D. Grasso, and L. Maccione. Diffuse neutrino and gamma-ray emissions of the galaxy above the TeV. *Journal of Cosmology and Astro-Particle Physics*, 6:3–+, June 2007.

[172] V. S. Ptuskin, S. I. Rogovaya, V. N. Zirakashvili, L. G. Chuvilgin, G. B. Khristiansen, E. G. Klepach, and G. V. Kulikov. Diffusion and drift of very high energy cosmic rays in galactic magnetic fields. *A&A*, 268:726–735, February 1993.

[173] J. Candia and E. Roulet. Diffusion and drift of cosmic rays in highly turbulent magnetic fields. *JCAP*, 10:7–+, October 2004.

[174] F. Casse, M. Lemoine, and G. Pelletier. Transport of cosmic rays in chaotic magnetic fields. *Phys. Rev. D*, 65(2):023002–+, January 2002.

[175] D. DeMarco, P. Blasi, and T. Stanev. Numerical propagation of high energy cosmic rays in the Galaxy: I. Technical issues. *JCAP*, 6:27–+, June 2007.

[176] X. H. Sun and J. L. Han. Structure Function Studies for Turbulent Interstellar Medium. In B. Uyaniker, W. Reich, & R. Wielebinski, editor, *The Magnetized Interstellar Medium*, pages 25–30, February 2004.

[177] A. W. Clegg, J. M. Cordes, J. M. Simonetti, and S. R. Kulkarni. Rotation measures of low-latitude extragalactic sources and the magnetoionic structure of the Galaxy. *ApJ*, 386:143–157, February 1992.

[178] M. Haverkorn, B. M. Gaensler, J. C. Brown, N. S. Bizunok, N. M. McClure-Griffiths, J. M. Dickey, and A. J. Green. Enhanced Small-Scale Faraday Rotation in the Galactic Spiral Arms. *ApJL*, 637:L33–L35, January 2006.

[179] S. D. Hunter, D. L. Bertsch, J. R. Catelli, T. M. Dame, S. W. Digel, B. L. Dingus, J. A. Esposito, C. E. Fichtel, R. C. Hartman, G. Kanbach, D. A. Kniffen, Y. C. Lin, H. A. Mayer-Hasselwander, P. F. Michelson, C. von Montigny, R. Mukherjee, P. L. Nolan, E. Schneid, P. Sreekumar, P. Thaddeus, and D. J. Thompson. EGRET Observations of the Diffuse Gamma-Ray Emission from the Galactic Plane. *ApJ*, 481:205–+, May 1997.

[180] J. L. Han and G. J. Qiao. The magnetic field in the disk of our Galaxy. *A&A*, 288:759–772, August 1994.

[181] T. Shibata, M. Hareyama, M. Nakazawa, and C. Saito. A Possible Approach to Three-dimensional Cosmic-Ray Propagation in the Galaxy. II. Stable Nuclei with Energy Change. *ApJ*, 642:882–901, May 2006.

[182] D. Maurin, A. Putze, and L. Derome. Systematic uncertainties on the cosmic-ray transport parameters. Is it possible to reconcile B/C data with $\delta = 1/3$ or $\delta = 1/2$? *A&A*, 516:A67+, June 2010.

[183] K. M. Ferrière. The interstellar environment of our galaxy. *Reviews of Modern Physics*, 73:1031–1066, October 2001.

[184] D. Maurin, R. Taillet, and F. Donato. New results on source and diffusion spectral features of Galactic cosmic rays: I B/C ratio. *A&A*, 394:1039–1056, November 2002.

[185] P. J. Boyle. The Elemental Composition of High-Energy Cosmic Rays:. Measurements with Tracer. *Modern Physics Letters A*, 23:2031–2045, 2008.

[186] M. Ave, P. J. Boyle, C. Höppner, J. Marshall, and D. Müller. Propagation and Source Energy Spectra of Cosmic Ray Nuclei at High Energies. *ApJ*, 697:106–114, May 2009.

[187] J. S. George, K. A. Lave, M. E. Wiedenbeck, W. R. Binns, A. C. Cummings, A. J. Davis, G. A. de Nolfo, P. L. Hink, M. H. Israel, R. A. Leske, R. A. Mewaldt, L. M. Scott, E. C. Stone, T. T. von Rosenvinge, and N. E. Yanasak. Elemental Composition and Energy Spectra of Galactic Cosmic Rays During Solar Cycle 23. *ApJ*, 698:1666–1681, June 2009.

[188] W. R. Binns, T. L. Garrard, P. S. Gibner, M. H. Israel, M. P. Kertzman, J. Klarmann, B. J. Newport, E. C. Stone, and C. J. Waddington. Abundances of ultraheavy elements in the cosmic radiation - Results from HEAO 3. *ApJ*, 346:997–1009, November 1989.

[189] S. P. Swordy, D. Mueller, P. Meyer, J. L'Heureux, and J. M. Grunsfeld. Relative abundances of secondary and primary cosmic rays at high energies. *ApJ*, 349:625–633, February 1990.

[190] AMS Collaboration, M. Aguilar, J. Alcaraz, J. Allaby, B. Alpat, G. Ambrosi, H. Anderhub, L. Ao, A. Arefiev, P. Azzarello, E. Babucci, L. Baldini, M. Basile, D. Barancourt, F. Barao, G. Barbier, G. Barreira, R. Battiston, R. Becker, U. Becker, L. Bellagamba, P. Béné, J. Berdugo, P. Berges, B. Bertucci, A. Biland, S. Bizzaglia, S. Blasko, G. Boella, M. Boschini, M. Bourquin, L. Brocco, G. Bruni, M. Buénerd, J. D. Burger, W. J. Burger, X. D. Cai, C. Camps, P. Cannarsa, M. Capell, D. Casadei, J. Casaus, G. Castellini, C. Cecchi, Y. H. Chang, H. F. Chen, H. S. Chen, Z. G. Chen, N. A. Chernoplekov, T. H. Chiueh, K. Cho, M. J. Choi, Y. Y. Choi, Y. L. Chuang, F. Cindolo, V. Commichau, A. Contin, E. Cortina-Gil, M. Cristinziani, J. P.

da Cunha, T. S. Dai, C. Delgado, J. D. Deus, N. Dinu, L. Djambazov, I. D'Antone, Z. R. Dong, P. Emonet, J. Engelberg, F. J. Eppling, T. Eronen, G. Esposito, P. Extermann, J. Favier, E. Fiandrini, P. H. Fisher, G. Fluegge, N. Fouque, Y. Galaktionov, M. Gervasi, P. Giusti, D. Grandi, O. Grimms, W. Q. Gu, K. Hangarter, A. Hasan, V. Hermel, H. Hofer, M. A. Huang, W. Hungerford, M. Ionica, R. Ionica, M. Jongmanns, K. Karlamaa, W. Karpinski, G. Kenney, J. Kenny, D. H. Kim, G. N. Kim, K. S. Kim, M. Y. Kim, A. Klimentov, R. Kossakowski, V. Koutsenko, M. Kraeber, G. Laborie, T. Laitinen, G. Lamanna, E. Lanciotti, G. Laurenti, A. Lebedev, C. Lechanoine-Leluc, M. W. Lee, S. C. Lee, G. Levi, P. Levtchenko, C. L. Liu, H. T. Liu, I. Lopes, G. Lu, Y. S. Lu, K. Lübelsmeyer, D. Luckey, W. Lustermann, C. Maña, A. Margotti, F. Mayet, R. R. McNeil, B. Meillon, M. Menichelli, A. Mihul, A. Mourao, A. Mujunen, F. Palmonari, A. Papi, H. B. Park, W. H. Park, M. Pauluzzi, F. Pauss, E. Perrin, A. Pesci, A. Pevsner, M. Pimenta, V. Plyaskin, V. Pojidaev, M. Pohl, V. Postolache, N. Produit, P. G. Rancoita, D. Rapin, F. Raupach, D. Ren, Z. Ren, M. Ribordy, J. P. Richeux, E. Riihonen, J. Ritakari, S. Ro, U. Roeser, C. Rossin, R. Sagdeev, D. Santos, G. Sartorelli, C. Sbarra, S. Schael, A. Schultz von Dratzig, G. Schwering, G. Scolieri, E. S. Seo, J. W. Shin, V. Shoutko, E. Shoumilov, R. Siedling, D. Son, T. Song, M. Steuer, G. S. Sun, H. Suter, X. W. Tang, S. C. C. Ting, S. M. Ting, M. Tornikoski, J. Torsti, J. Trümper, J. Ulbricht, S. Urpo, E. Valtonen, J. Vandenhirtz, F. Velcea, E. Velikhov, B. Verlaat, I. Vetlitsky, F. Vezzu, J. P. Vialle, G. Viertel, D. Vité, H. von Gunten, S. W. Wicki, W. Wallraff, B. C. Wang, J. Z. Wang, Y. H. Wang, K. Wiik, C. Williams, S. X. Wu, P. C. Xia, J. L. Yan, L. G. Yan, C. G. Yang, J. Yang, M. Yang, S. W. Ye, P. Yeh, Z. Z. Xu, H. Y. Zhang, Z. P. Zhang, D. X. Zhao, G. Y. Zhu, W. Z. Zhu, H. L. Zhuang, A. Zichichi, B. Zimmermann, and P. Zuccon. The Alpha Magnetic Spectrometer (AMS) on the International Space Station: Part I - results from the test flight on the space shuttle. *Phys. Rep.*, 366:331–405, August 2002.

[191] T. Sanuki, M. Motoki, H. Matsumoto, E. S. Seo, J. Z. Wang, K. Abe, K. Anraku, Y. Asaoka, M. Fujikawa, M. Imori, T. Maeno, Y. Makida, N. Matsui, H. Matsunaga, J. Mitchell, T. Mitsui, A. Moiseev, J. Nishimura, M. Nozaki, S. Orito, J. Ormes, T. Saeki, M. Sasaki, Y. Shikaze, T. Sonoda, R. Streitmatter, J. Suzuki, K. Tanaka, I. Ueda, N. Yajima, T. Yamagami, A. Yamamoto, T. Yoshida, and K. Yoshimura. Precise Measurement of Cosmic-Ray Proton and Helium Spectra with the BESS Spectrometer. *ApJ*, 545:1135–1142, December 2000.

[192] J. R. Letaw, R. Silberberg, and C. H. Tsao. Propagation of heavy cosmic-ray nuclei. *ApJS*, 56:369–391, November 1984.

[193] W. R. Webber, J. C. Kish, and D. A. Schrier. Total charge and mass changing cross

sections of relativistic nuclei in hydrogen, helium, and carbon targets. *Phys. Rev. B*, 41:520–532, February 1990.

[194] L. C. Tan and L. K. Ng. Calculation of the equilibrium antiproton spectrum. *Journal of Physics G Nuclear Physics*, 9:227–242, February 1983.

[195] W. R. Webber, A. Soutoul, J. C. Kish, and J. M. Rockstroh. Updated Formula for Calculating Partial Cross Sections for Nuclear Reactions of Nuclei with Z $<$ 28 and E $>$ 150 MeV Nucleon^{-1} in Hydrogen Targets. *ApJS*, 144:153–167, January 2003.

[196] M. Asplund, N. Grevesse, and A. Jacques Sauval. The solar chemical composition. *Nuclear Physics A*, 777:1–4, October 2006.

[197] L. J. Gleeson and W. I. Axford. Solar Modulation of Galactic Cosmic Rays. *ApJ*, 154:1011–+, December 1968.

[198] J. W. Bieber, R. A. Burger, R. Engel, T. K. Gaisser, S. Roesler, and T. Stanev. Antiprotons at Solar Maximum. *Physical Review Letters*, 83:674–677, July 1999.

[199] V. S. Ptuskin, I. V. Moskalenko, F. C. Jones, A. W. Strong, and V. N. Zirakashvili. Dissipation of Magnetohydrodynamic Waves on Energetic Particles: Impact on Interstellar Turbulence and Cosmic-Ray Transport. *ApJ*, 642:902–916, May 2006.

[200] M. Boezio, V. Bonvicini, P. Schiavon, A. Vacchi, N. Zampa, D. Bergström, P. Carlson, T. Francke, S. Grinstein, M. Suffert, M. Hof, J. Kremer, W. Menn, M. Simon, S. A. Stephens, M. Ambriola, R. Bellotti, F. Cafagna, F. Ciacio, M. Circella, C. De Marzo, N. Finetti, P. Papini, S. Piccardi, P. Spillantini, E. Vannuccini, S. Bartalucci, M. Ricci, M. Casolino, M. P. De Pascale, A. Morselli, P. Picozza, R. Sparvoli, J. W. Mitchell, J. F. Ormes, R. E. Streitmatter, U. Bravar, and S. J. Stochaj. The Cosmic-Ray Antiproton Flux between 3 and 49 GeV. *ApJ*, 561:787–799, November 2001.

[201] D. Maurin, R. Taillet, F. Donato, P. Salati, A. Barrau, and G. Boudoul. Galactic Cosmic Ray Nuclei as a Tool for Astroparticle Physics. *ArXiv Astrophysics e-prints*, December 2002.

[202] L. Bronfman, R. S. Cohen, H. Alvarez, J. May, and P. Thaddeus. A CO survey of the southern Milky Way - The mean radial distribution of molecular clouds within the solar circle. *ApJ*, 324:248–266, January 1988.

[203] K. Ferrière, W. Gillard, and P. Jean. Spatial distribution of interstellar gas in the innermost 3 kpc of our galaxy. *A&A*, 467:611–627, May 2007.

[204] C. Evoli, D. Gaggero, D. Grasso, and L. Maccione. Diffuse gamma emission of the Galaxy from cosmic rays. *Nuclear Instruments and Methods in Physics Research A*, 588:22–25, April 2008.

[205] D. N. *et al.* Spergel. Three-Year Wilkinson Microwave Anisotropy Probe (WMAP) Observations: Implications for Cosmology. *ApJS*, 170:377–408, June 2007.

[206] W.-M. Yao and et al. Review of Particle Physics. *Journal of Physics G Nuclear Physics*, 33:1–1232, July 2006.

[207] F. Spite and M. Spite. Abundance of lithium in unevolved halo stars and old disk stars - Interpretation and consequences. *A&A*, 115:357–366, November 1982.

[208] M. Spite, F. Spite, and J. P. Maillard. Abundance of lithium in another sample of halo dwarfs, and in the spectroscopic binary BD-0 deg 4234. *A&A*, 141:56–60, December 1984.

[209] S. G. Ryan, J. E. Norris, and T. C. Beers. The Spite Lithium Plateau: Ultrathin but Postprimordial. *ApJ*, 523:654–677, October 1999.

[210] M. Asplund, D. L. Lambert, P. E. Nissen, F. Primas, and V. V. Smith. Lithium Isotopic Abundances in Metal-poor Halo Stars. *ApJ*, 644:229–259, June 2006.

[211] P. *et al.* Bonifacio. First stars VII - Lithium in extremely metal poor dwarfs. *A&A*, 462:851–864, February 2007.

[212] R. H. Cyburt. Primordial nucleosynthesis for the new cosmology: Determining uncertainties and examining concordance. *Phys. Rev. D*, 70(2):023505–+, July 2004.

[213] A. Cuoco, F. Iocco, G. Mangano, G. Miele, O. Pisanti, and P. D. Serpico. Present Status of Primordial Nucleosynthesis after Wmap:. *International Journal of Modern Physics A*, 19:4431–4453, 2004.

[214] A. Coc, E. Vangioni-Flam, P. Descouvemont, A. Adahchour, and C. Angulo. Updated Big Bang Nucleosynthesis Compared with Wilkinson Microwave Anisotropy Probe Observations and the Abundance of Light Elements. *ApJ*, 600:544–552, January 2004.

[215] M. H. Pinsonneault, G. Steigman, T. P. Walker, and V. K. Narayanan. Stellar Mixing and the Primordial Lithium Abundance. *ApJ*, 574:398–411, July 2002.

[216] A. J. Korn, F. Grundahl, O. Richard, P. S. Barklem, L. Mashonkina, R. Collet, N. Piskunov, and B. Gustafsson. A probable stellar solution to the cosmological lithium discrepancy. *Nat*, 442:657–659, August 2006.

[217] M. Kawasaki, K. Kohri, and T. Moroi. Big-bang nucleosynthesis and hadronic decay of long-lived massive particles. *Phys. Rev. D*, 71(8):083502–+, April 2005.

[218] K. Jedamzik, K.-Y. Choi, L. Roszkowski, and R. Ruiz de Austri. Solving the cosmic lithium problems with gravitino dark matter in the constrained minimal supersymmetric standard model. *JCAP*, 7:7–+, July 2006.

[219] Maxim Pospelov. Particle physics catalysis of thermal big bang nucleosynthesis. *Phys. Rev. Lett.*, 98:231301, 2007.

[220] Daniel Cumberbatch et al. Solving the cosmic lithium problems with primordial late-decaying particles. *Phys. Rev.*, D76:123005, 2007.

[221] M. Kusakabe, T. Kajino, R. N. Boyd, T. Yoshida, and G. J. Mathews. Simultaneous solution to the ^{6}Li and ^{7}Li big bang nucleosynthesis problems from a long-lived negatively charged leptonic particle. *Phys. Rev. D*, 76(12):121302–+, December 2007.

[222] V. Tatischeff and J.-P. Thibaud. Is ^{6}Li in metal-poor halo stars produced in situ by solar-like flares? *A&A*, 469:265–274, July 2007.

[223] F. Miniati, D. Ryu, H. Kang, T. W. Jones, R. Cen, and J. P. Ostriker. Properties of Cosmic Shock Waves in Large-Scale Structure Formation. *ApJ*, 542:608–621, October 2000.

[224] T. K. Suzuki and S. Inoue. Cosmic-Ray Production of ^{6}Li by Structure Formation Shocks in the Early Milky Way: A Fossil Record of Dissipative Processes during Galaxy Formation. *ApJ*, 573:168–173, July 2002.

[225] U. Keshet, E. Waxman, A. Loeb, V. Springel, and L. Hernquist. Gamma Rays from Intergalactic Shocks. *ApJ*, 585:128–150, March 2003.

[226] E. Rollinde, E. Vangioni, and K. A. Olive. Population III Generated Cosmic Rays and the Production of ^{6}Li. *ApJ*, 651:658–666, November 2006.

[227] F. Daigne, K. A. Olive, J. Silk, F. Stoehr, and E. Vangioni. Hierarchical Growth and Cosmic Star Formation: Enrichment, Outflows, and Supernova Rates. *ApJ*, 647:773–786, August 2006.

[228] W. H. Press and P. Schechter. Formation of Galaxies and Clusters of Galaxies by Self-Similar Gravitational Condensation. *ApJ*, 187:425–438, February 1974.

[229] M. Volonteri, F. Haardt, and P. Madau. The Assembly and Merging History of Supermassive Black Holes in Hierarchical Models of Galaxy Formation. *ApJ*, 582:559–573, January 2003.

[230] V. Bromm, A. Ferrara, P. S. Coppi, and R. B. Larson. The fragmentation of pre-enriched primordial objects. *MNRAS*, 328:969–976, December 2001.

[231] R. Schneider, A. Ferrara, P. Natrajan, and K. Omukai. First Stars, Very Massive Black Holes, and Metals. *ApJ*, 571:30–39, May 2002.

[232] R. Schneider, A. Ferrara, R. Salvaterra, K. Omukai, and V. Bromm. Low-mass relics of early star formation. *Nat*, 422:869–871, April 2003.

[233] K. Omukai, T. Tsuribe, R. Schneider, and A. Ferrara. Thermal and Fragmentation Properties of Star-forming Clouds in Low-Metallicity Environments. *ApJ*, 626:627–643, June 2005.

[234] R. Schneider, K. Omukai, A. K. Inoue, and A. Ferrara. Fragmentation of star-forming clouds enriched with the first dust. *MNRAS*, 369:1437–1444, July 2006.

[235] A. Heger and S. E. Woosley. The Nucleosynthetic Signature of Population III. *ApJ*, 567:532–543, March 2002.

[236] A. M. Hopkins. On the Evolution of Star-forming Galaxies. *ApJ*, 615:209–221, November 2004.

[237] R. Ganguly, K. R. Sembach, T. M. Tripp, and B. D. Savage. Highly Ionized Gas in the Galactic Halo and the High-Velocity Clouds toward PG 1116+215. *ApJS*, 157:251–278, April 2005.

[238] T. Montmerle. On the possible existence of cosmological cosmic rays. I - The framework for light-element and gamma-ray production. *ApJ*, 216:177–191, August 1977.

[239] R. Blandford and D. Eichler. Particle Acceleration at Astrophysical Shocks - a Theory of Cosmic-Ray Origin. *Phys. Rep.*, 154:1–+, October 1987.

[240] V. Tatischeff. Cosmic-ray acceleration in supernova shocks. *ArXiv e-prints*, 804, April 2008.

[241] P. O. Lagage and C. J. Cesarsky. The maximum energy of cosmic rays accelerated by supernova shocks. *A&A*, 125:249–257, September 1983.

[242] D. H. Zhao, H. J. Mo, Y. P. Jing, and G. Börner. The growth and structure of dark matter haloes. *MNRAS*, 339:12–24, February 2003.

[243] M. Jubelgas, V. Springel, T. Enßlin, and C. Pfrommer. Cosmic ray feedback in hydrodynamical simulations of galaxy formation. *A&A*, 481:33–63, April 2008.

[244] U. Heinbach and M. Simon. Propagation of galactic cosmic rays under diffusive reacceleration. *ApJ*, 441:209–221, March 1995.

[245] M. Meneguzzi, J. Audouze, and H. Reeves. The production of the elements Li, Be, B by galactic cosmic rays in space and its relation with stellar observations. *A&A*, 15:337–359, 1971.

[246] D. J. *et al.* Mercer. Production of A=6,7 nuclides in the $\alpha+\alpha$ reaction and cosmic ray nucleosynthesis. *Phys. Rev. C*, 63(6):065805–+, June 2001.

[247] E. Rollinde, E. Vangioni, and K. Olive. Cosmological Cosmic Rays and the Observed ^{6}Li Plateau in Metal-poor Halo Stars. *ApJ*, 627:666–673, July 2005.

[248] W. H. Press. *Numerical recipes in C++ : the art of scientific computing.* Numerical recipes in C++ : the art of scientific computing by William H. Press. xxviii, 1,002 p. : ill. ; 26 cm. Includes bibliographical references and index. ISBN : 0521750334, 2002.

[249] A. W. Strong and I. V. Moskalenko. Propagation of Cosmic-Ray Nucleons in the Galaxy. *ApJ*, 509:212–228, December 1998.

[250] N. Prantzos. The energetics, evolution, and stellar depletion of ^{6}Li in the early Galaxy. *A&A*, 448:665–675, March 2006.

[251] P. McDonald, U. Seljak, S. Burles, D. J. Schlegel, D. H. Weinberg, R. Cen, D. Shih, J. Schaye, D. P. Schneider, N. A. Bahcall, J. W. Briggs, J. Brinkmann, R. J. Brunner, and M. Fukugita. The Lyα Forest Power Spectrum from the Sloan Digital Sky Survey. *ApJS*, 163:80–109, March 2006.

[252] T. J. W. Lazio, J. M. Cordes, A. G. de Bruyn, and J.-P. Macquart. The microarcsecond sky and cosmic turbulence. *New Astronomy Review*, 48:1439–1457, December 2004.

[253] P.-S. Corasaniti, D. Huterer, and A. Melchiorri. Exploring the dark energy redshift desert with the Sandage-Loeb test. *Phys. Rev. D*, 75(6):062001–+, March 2007.

[254] J. Liske, A. Grazian, E. Vanzella, M. Dessauges, M. Viel, L. Pasquini, M. Haehnelt, S. Cristiani, F. Pepe, G. Avila, P. Bonifacio, F. Bouchy, H. Dekker, B. Delabre, S. D'Odorico, V. D'Odorico, S. Levshakov, C. Lovis, M. Mayor, P. Molaro, L. Moscardini, M. T. Murphy, D. Queloz, P. Shaver, S. Udry, T. Wiklind, and S. Zucker. Cosmic dynamics in the era of Extremely Large Telescopes. *MNRAS*, 386:1192–1218, May 2008.